



Universidad de Concepción

Dirección de Postgrado

Facultad de Ciencias Físicas y Matemáticas

Programa de Doctorado en Ciencias Físicas

**Rol del Ambiente en el Cese de la
Formación Estelar en Galaxias.
(Understanding The Role of the
Environment in the Quenching of
Galaxies)**

Tesis presentada para optar al grado académico de Doctor
en Ciencias Físicas

Daniela Estefanía Olave Rojas
Marzo 2019
Concepción - Chile

Profesor Guía: Ricardo Javier Demarco López
Departamento de Astronomía
Facultad de Ciencias Físicas y Matemáticas
Universidad de Concepción



*Dedicada a Teresita, Alejandro, David y Felipe
por su infinito amor y apoyo durante todos estos años*

Agradecimientos

Este trabajo representa el punto final de mi carrera estudiantil, la cual comenzó hace ya 25 años durante mi primer día de clases en el kinder D de “Las Concentradas”. Los últimos 12 años de este largo recorrido se han escapado a todo pronóstico de lo que alguna vez pensé sería mi carrera estudiantil, pero sin duda han sido 12 años de infinito aprendizaje tanto profesional como personal. Es por esto, que quiero agradecer a todas las personas que de una forma u otra me han ayudado a que este recorrido haya sido más llevadero.

En primer lugar, quiero agradecer a Felipe, quien ha sido mi compañero de vida durante ya 13 años, quien decidió tomar mi mano y nunca más soltarla, quien me ha impulsado a alcanzar todas las metas que me he propuesto, quien ha cuidado de mi con su inmenso amor. Felipe, nunca me cansaré de agradecerte por tu infinito amor, te amo, y como te dije alguna vez, recuerda que la aventura nos aguarda.

Agradezco a Teresita, Alejandro y David, mis padres y hermano, quienes han estado presente durante toda mi vida apoyándome incondicionalmente, por darme el apoyo y la confianza para ir a cazar todos mis sueños y volver a casa cada vez que ha sido necesario. Mamá, gracias por tu amor incondicional, por tu paciencia en los momentos más críticos de este camino y por todo lo que me has enseñado. Papá, gracias por haberme dado todo en la vida y más, gracias por entenderme incluso sin palabras, gracias por estar ahí silenciosamente. David, eres el mejor hermano que podría haber tenido, muchas gracias por estar incondicionalmente para mi, a pesar de que vivas al otro lado del charco, eres mi modelo a seguir, cuando grande quiero ser como tú jaja. Teresita, Alejandro y David, los amo profundamente, gracias por la guía que me han dado durante toda mi vida y por amarme tal como soy sin condiciones.

Quiero agradecer a Ricardo Demarco, mi supervisor, por haber confiado en mi y apoyarme incluso antes de conocernos personalmente. Gracias Ricardo por guiarme en estos últimos 4 años de mi carrera estudiantil, por conseguir todo lo que he necesitado y por apoyar mis decisiones. Sin duda tu apoyo ha sido fundamental para haber concluido este proceso de la mejor manera posible, el cual no ha estado exento de contratiempos.

También quiero agradecer a Pierluigi Cerulo, mi otro supervisor, quien me ha dado apoyo científico y psicológico cada vez que me ha hecho falta durante el desarrollo de esta Tesis. Pierluigi, muchas gracias por todas tus enseñanzas, consejos, correcciones y guía.

Sin tu apoyo este trabajo no hubiese sido tan fácil, muchas gracias por todo.

Agradezco a los amigos que la vida me ha dado, los cuales son parte de mi familia. Comienzo por agradecer a Carlos y Camila B., mis compadres, quienes han estado siempre presente cuando los he necesitado, muchas gracias por confiar en mí al haberme escogido como la madrina de Vicente a pesar de mi traslado constante por distintas ciudades del país para lograr este objetivo. Camila S., nos conocemos hace 26 años, hemos compartido una vida juntas y espero seguir sumando años, gracias por estar ahí. Francisco, a ti te conozco hace menos años (sólo 12 jejeje), pero eres mi gran amigo, siempre te agradeceré por el apoyo que me diste cuando hice el Magíster y almorzábamos “juntos” para que no me sintiera sola. Claudia, muchas gracias por tu amistad cuando más falta me ha hecho, lo nuestro fue una amistad a primera vista jajaja. Javier, no compartimos la sangre, pero eres el hermano que escogí, gracias por estar siempre ahí y por ser parte de mi vida, a pesar de la distancia. Marco, sufrimos junto este camino llamado Doctorado desde dos áreas de la física diferentes, muchas gracias por haber hecho terapia psicológica conmigo cada vez que algo nos aterraba.

Gracias a mis suegros Aída y Cristian, primero por haberme “dado” a Felipe y por haber aceptado que se fuera a otra ciudad conmigo. Gracias por apoyarme y enorgullirse de mi en cada paso que doy, gracias por hacerme sentir una hija más con todo el amor que me han entregado durante todos estos años.

Agradezco de manera especial a Sergio Torres, quien fue mi Director de Tesis durante el Magíster, por haberme dado su apoyo y confianza desde el primer momento. Sergio, sabes que no me agradan las demostraciones de afecto públicas, pero esto lo vale. Muchas gracias por tu guía durante mis primeros años de carrera científica, eres un pilar fundamental en este proceso y sin ti nada de esto hubiera sido posible. Muchas gracias y un abrazo apretado para tí jajaja, te quiero mucho.

Doy gracias a todas las personas que se cruzaron en mi camino durante estos 8 años de aprendizaje desde que partí a La Serena hasta que me trasladé a Concepción. Muchas gracias a todas las personas que me extendieron una mano amiga cuando más lo necesité.

Finalmente, agradezco el apoyo financiero de CONICYT a través de su Beca/Nacional-Doctorado año 2015 Folio N° 21150415, el cual fue fundamental para el desarrollo de esta Tesis.

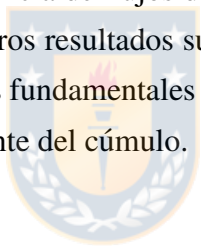
Resumen

El objetivo principal de esta Tesis es entender los efectos de los impulsores externos de la evolución de las galaxias a través del análisis de sus propiedades en distintos ambientes. Para abordar este problema, realizamos dos estudios complementarios enfocados en el escenario del *preprocesamiento* de galaxias, el cual sugiere que las galaxias apagan su formación estelar en grupos antes de caer al ambiente del cúmulo (Zabludoff & Mulchaey 1998, Fujita 2004). El primer estudio aborda el fenómeno del preprocesamiento de galaxias desde una perspectiva global, mientras que el segundo estudio lo hace desde una perspectiva local.

En la primera parte de nuestra investigación hemos estudiado el efecto del ambiente local en los colores de las galaxias utilizando una muestra de dos cúmulos de galaxias en $z \sim 0.40$, MACS J0416.1-2403 and MACS J1206.2-0847, obtenidos del programa de observación CLASH-VLT (Rosati et al., 2014) y una muestra de galaxias de campo en el mismo desplazamiento al rojo de los cúmulos obtenida del catálogo COSMOS/UltraVISTA (Muzzin et al., 2013). Para estudiar la relación entre los colores ópticos de las galaxias y el ambiente, el primer paso de nuestro análisis fue la identificación de subestructuras en los cúmulos usando una combinación de métodos estadísticos y algoritmos de agrupación. Esta técnica permite la identificación de subestructuras considerando la posición angular de las galaxias y su velocidad peculiar con respecto al centro del cúmulo. Luego, mediante el uso de la bimodalidad en colores mostrada por la relación color-magnitud separamos las galaxias en azules (con formación estelar) y rojas (sin formación estelar) para estudiar las fracciones de color de galaxias en los cúmulos y subestructuras en función de la distancia al centro del cúmulo o en función de la distancia al centro de la sobredensidad (cúmulo o subestructura). Este análisis muestra que la fracción de galaxias azules en los cúmulos y en las subestructuras es siempre menor al valor promedio de las galaxias azules en el campo. Además, encontramos que los cúmulos y las subestructuras tienen una eficiencia ambiental comparable en la formación de galaxias rojas. Estos resultados sugieren que el preprocesamiento juega un papel importante en la formación y evolución de galaxias rojas en cúmulos.

Debido a que los estudios altamente detallados de las propiedades de las galaxias en grupos con alto desplazamiento al rojo aún no son posibles con la tecnología actual, la única forma de estudiar los detalles del preprocesamiento en grupos es a través de la obser-

vación de estructuras en el Universo local. Por esta razón, en la segunda parte de nuestra investigación se presenta un detallado análisis fotométrico y espectroscópico de las tres galaxias que componen el grupo Arp 314 (Arp 314-1, Arp 314-2 y Arp 314-3). Mediante la inspección visual de las imágenes ópticas encontramos que las galaxias del grupo tienen una morfología perturbada con signos claros de una interacción gravitacional. Adicionalmente, las imágenes sugieren la existencia de regiones de formación estelar, las cuales son confirmadas por la información espectroscópica disponible. Estas regiones se ubican principalmente en las colas de marea de Arp 314-1 y sus espectros tienen líneas de emisión consistentes con edades jóvenes (≤ 10 millones de años), sugiriendo que fueron formadas como una consecuencia de las interacciones entre las galaxias de Arp 314. Mediante el uso de los espectros de las regiones de formación estelar estimamos el gradiente de metalicidad de Arp 314-1, el cual es más plano que el encontrado en sistemas sin interacción. Adicionalmente, encontramos que las galaxias en Arp 314 tienen una cinemática compleja que sugiere la existencia de flujos de gas los cuales explicarían el gradiente de metalicidad observado. Nuestros resultados sugieren que la interacción entre galaxias es uno de los mecanismos físicos fundamentales en conducir la evolución de galaxias en los grupos antes de caer al ambiente del cúmulo.



Abstract

The main goal of this Thesis is to understand the effects of the external drivers of galaxy evolution through the analysis of the galaxy properties in different environments. To address this problem, we developed two complementary studies focusing on the galaxy *pre-processing* scenario, which suggest that galaxies quench their star formation in groups before falling into the cluster environment (Zabludoff & Mulchaey 1998, Fujita 2004). The first study addressed the phenomenon of galaxy pre-processing from a global perspective, while the second study does it from a local perspective.

In the first part of our investigation we have studied the effect of the local environment on galaxy colours using a sample of two clusters at $z \sim 0.40$, MACS J0416.1-2403 and MACS J1206.2-0847, drawn from the observing programme CLASH-VLT (Rosati et al., 2014) and a sample of field galaxies at the same redshift of the clusters obtained from the COSMOS/UltraVISTA catalogue (Muzzin et al., 2013). To study the relationship between the optical colours of galaxies with the environment, the first step of our analysis was the identification of substructures in clusters using a combination of statistical methods and clustering algorithms. This technique allows the identification of substructures considering the angular position of galaxies and their peculiar velocity with respect to the cluster centre. We then use the colour bimodality seen in the the colour-magnitude relation to separate galaxies in blue (star-forming) and red (quiescent) in order to constrain the colour fraction of galaxies in clusters and substructures as a function of distance from the cluster centre or as a function of distance distance from the centre of the overdensity structure (cluster or substructure). This analysis shows that the fraction of blue galaxies in both the main clusters and in the substructures is always lower than the average fraction of blue galaxies in the field. Moreover, we found that the clusters and substructures have a comparable environmental efficiency in producing red galaxies. These results suggest that the pre-processing plays a role in the formation and evolution of red galaxies in clusters.

Given that detailed studies of galaxy properties in groups at high redshift are still challenging with current technology, the only way of studying the details of pre-processing in groups is through the observation of structures in the local Universe. For this reason, in the second part of this Thesis we present a detailed photometric and spectroscopic analysis of the three galaxies that make up the group Arp 314 (Arp 314-1, Arp 314-2 and Arp 314-3). The optical images show that the galaxies of the group have a disturbed mor-

phology with clear signs of a gravitational interaction. In addition, images suggest the existence of star-forming regions, which are confirmed by the spectroscopic information available. These regions are located principally in the tidal tails of Arp 314-1 and their spectra have emission lines consistent with young ages (≤ 10 Myrs), suggesting that were formed as a consequence of the interactions between galaxies. By using the spectra of the star-forming regions we estimated the metallicity gradient of Arp 314-1, which is flatter than that found in non-interacting systems. In addition, we found that the galaxies in Arp 314 have a complex kinematics that suggests the presence of gas flows, which would explain the observed metallicity gradient. Our results suggest that the interaction between galaxies is one of the fundamental physical mechanisms driving the galaxy evolution in groups before their entrance into the cluster environment.



Contents

Agradecimientos	iii
Resumen	v
Abstract	vii
List of Figures	xii
List of Tables	xiv
1 Introduction	1
1.1 Environmental Effects on the Properties of Galaxies	2
1.2 Groups and Clusters of Galaxies as Cosmic Laboratories	6
1.3 The Pre-processing of Galaxies	10
1.4 Motivation and Outline of the Thesis	13
2 Sample and Data Description	15
2.1 Clusters Sample	15
2.1.1 MACS J0416.1-2403 and MACS J1206.2-0847	15
2.1.2 The MACS0416 and MACS1206 data-sets	18
2.2 The Arp 314 Group	23
2.2.1 Arp 314 Observations and Data	24
2.3 The Field Sample	27
3 Galaxy pre-processing in substructures around $z \sim 0.4$ galaxy clusters	28
3.1 Introduction	29
3.2 Data	32
3.2.1 Photometric Catalogues	32
3.2.2 Spectroscopic Catalogues	33
3.3 Measurement and Data Analysis	34
3.3.1 Spectroscopic Completeness	34
3.3.2 Photometric Redshifts	35
3.4 Results	36

3.4.1	Cluster membership, velocity dispersion and stellar mass	36
3.4.2	Detection of Substructures	37
3.4.3	Colour-Magnitude Diagram	40
3.4.4	Photometric Members	41
3.4.5	Stellar Masses	44
3.4.6	Colour Fractions	45
3.4.7	Substructure Quenching Efficiency	53
3.5	Discussion	55
3.5.1	Substructure detections	55
3.5.2	Colour fractions in substructures and galaxy clusters	58
3.5.3	Evidence for pre-processing from the colour fractions in substructures	60
3.6	Summary and Conclusions	63
4	Revealing the effects of galaxy interaction in the main galaxies of the southern group Arp 314	65
4.1	Introduction	66
4.2	Data	67
4.2.1	Imaging and spectroscopy	67
4.2.2	Fabry-Perot data	70
4.2.3	Complementary data	70
4.3	Analysis	71
4.3.1	Extinctions and flux measurements	71
4.3.2	Star formation rates and stellar masses	74
4.3.3	Gas-phase oxygen abundances	75
4.4	Results	76
4.4.1	Inspecting the optical morphology of galaxies in Arp 314	76
4.4.2	Internal extinctions, radial velocities and line fluxes	77
4.4.3	H α luminosities: From typical HII regions to giant HII region candidates	77
4.4.4	Ionization mechanism and AGN activity	78
4.4.5	Star formation rates	79
4.4.6	Gas-phase oxygen abundances	82

<i>Contents</i>	xi
4.4.7 Kinematics: Searching for gas motions	84
4.5 Discussion	88
4.5.1 Discovering the unexplored interacting system Arp 314	88
4.5.2 Gas flows and the flattening of the gas-phase oxygen distribution .	90
4.6 Summary and conclusions	92
5 Conclusions and Future Plans	93
5.1 General Conclusions	93
5.2 Future Plans	94
Bibliography	96
Appendices	118
A Data Tables	119



List of Figures

1.1	The morphology-density relation	3
1.2	Interacting group NGC 6845	4
1.3	The observed metallicity profile with radius for M101	5
1.4	The observed metallicity profile with radius for NGC92	6
1.5	Morphology-density and morphology-clustercentric radius relations . . .	7
1.6	Typical scheme of merger tree in the Λ CDM hierarchical scenario of structure formation	8
1.7	Fraction of star-forming galaxies as a function of projected distance from the cluster centre	9
2.1	Galaxy cluster MACS J0416.1-2403	16
2.2	Galaxy cluster MACS J1206.2-0847.	17
2.3	The Arp314 group	23
3.1	Spectroscopic Completeness	35
3.2	Spatial and radial velocity distribution of cluster members	40
3.3	Colour-magnitude diagrams	42
3.4	Colour histogram that shows the bimodal distribution in $(B - R_c)$ colour .	43
3.5	Colour fraction as a function of projected distance	47
3.6	Colour fraction as a function of projected distance in bins of stellar mass .	48
3.7	Colour fraction as a function of apparent magnitude and stellar mass . . .	49
3.8	Background-corrected colour fractions as a function of projected distance	51
3.9	Background-corrected colour fractions as a function of projected distance in bins of stellar mass	52
3.10	Background-corrected colour fractions as a function of apparent magni- tude and stellar mass	53
3.11	Environmental quenching efficiency	54
3.12	Environmental quenching efficiency separated by mass	55
3.13	Environmental quenching efficiency as a function of distance from the overdensity centre	56
3.14	Environmental quenching efficiency as a function of distance from the overdensity centre separated by mass	57

4.1	<i>r'</i> -band image of Arp 314	68
4.2	Spectra of two star-forming regions in Arp 314	72
4.3	Observed spectrum of Arp 314-1	73
4.4	Emission line diagnostic diagram for the regions observed in Arp 314 . .	80
4.5	Gemini/GMOS <i>r'</i> -band image of Arp 314-1 and Arp 314-2	81
4.6	Oxygen abundance gradient for Arp 314-1	84
4.7	Images and velocity fields for Arp 314	85



List of Tables

2.1	The CLASH Cluster Sample	19
2.2	Gemini/GMOS spectroscopic instrumental and observational setup	26
3.1	Main properties of the clusters MACS0416 and MACS1206	37
3.2	Results from the DS-Test on MACS0416 and MACS1206	38
3.3	Substructures identified in MACS0416 and MACS1206 and their principal features	41
3.4	Mean environmental quenching efficiency in clusters and substructures.	55
4.1	Positions, radial velocities and internal extinctions for sources in Arp 314	69
4.2	<i>WISE</i> information for galaxies in Arp 314	71
4.3	Line fluxes for the star-forming regions located in the tidal tail and main body of Arp 314	78
4.4	Star formation rates, stellar masses and specific star formation rates	82
A.1	Spectroscopic colour fraction as a function of distance from the cluster centre.	120
A.2	Spectroscopic colour fraction as a function of distance from the overdensity centre	120
A.3	Spectroscopic colour fraction as a function of distance from the cluster centre for massive and less massive galaxies	121
A.4	Spectroscopic colour fraction as a function of distance from the overdensity centre for massive and less massive galaxies	122
A.5	Spectroscopic colour fraction as a function of R_c	122
A.6	Spectroscopic colour fraction as a function of $\log(M_\star/M_\odot)$	123
A.7	Spectrophotometric colour fraction as a function of distance from the cluster centre.	123
A.8	Spectrophotometric colour fraction as a function of distance from the overdensity centre	123
A.9	Spectrophotometric colour fraction as a function of distance from the cluster centre for massive and less massive galaxies	124

A.10 Spectrophotometric colour fraction as a function of distance from the overdensity centre for massive and less massive galaxies	125
A.11 Spectrophotometric colour fraction as a function of R_c	125
A.12 Spectrophotometric colour fraction as a function of $\log(M_\star/M_\odot)$	126
A.13 Mean environmental quenching efficiency as a function of distance from the cluster centre for the spectroscopic sample.	126
A.14 Mean environmental quenching efficiency as a function of distance from the overdensity centre for the spectroscopic sample.	126
A.15 Mean environmental quenching efficiency as a function of distance from the cluster centre for the spectrophotometric sample.	127
A.16 Mean environmental quenching efficiency as a function of distance from the overdensity centre for the spectrophotometric sample.	127



1

Introduction

Since the discovery of the existence of galaxies in the Universe, humanity has been interested in understanding how the formation and evolution of these systems is developed. By “formation” one means the physical processes that led to the constitution of galaxies, while with “evolution” one means the physical changes that occur in them over time. It is currently well established that the evolution of galaxies is driven by a combination of internal and external mechanisms which can be respectively linked to their stellar mass and the environment in which they reside. A key problem in modern astrophysics is to understand the role of the environment in the evolution of galaxies.

The present Thesis focuses on the study of galaxy properties in different environments with the aim of investigating the effects of the external drivers of galaxy evolution. In particular, this Thesis consists of the observational study of galaxies in two clusters at $z \sim 0.40$, namely MACS J0416.1-2403 (MACS0416) and MACS J1206.2-0847 (MACS1206) and in the Arp 314 group, at $z = 0.01$.

The data for the two $z = 0.4$ clusters were drawn from the Large Programme *Dark Matter Mass Distributions of Hubble Treasury Clusters and the Foundations of Λ CDM Structure Formation Models* (CLASH-VLT, Rosati et al. 2014), which is a spectroscopic follow-up of 13 clusters in the Cluster Lensing and Supernova survey with Hubble (CLASH; Postman et al. 2012). CLASH-VLT is a programme aimed at reconstructing cluster mass profiles using the spectroscopic galaxy members as tracers. Observations were conducted at the European Southern Observatory Very Large Telescope (ESO/VLT) with the Visible Multi-Object Spectrograph (VIMOS; Le Fèvre et al. 2003), which allowed the collection of the redshifts for up to 1000 galaxy members out to 3 virial radii from the cluster centre.

Arp 314 was instead observed as part of the programme GS-2013B-Q-27, PI: S.

Torres-Flores, conducted at the Gemini South telescope with the Gemini Multi-Object Spectrograph (GMOS-S, Hook et al. 2004) and aimed at the detailed study of galaxy interactions.

1.1 Environmental Effects on the Properties of Galaxies

The environment plays an important role in driving the evolution of galaxies, as demonstrated in many theoretical and observational studies (e.g Lewis et al. 2002, Poggianti et al. 2006, McGee et al. 2009, Demarco et al. 2010, Jaffé et al. 2016, Cerulo et al. 2017). It is observed indeed that several properties of galaxies such as morphology, colour, and star-formation rate (SFR) are affected by the environment in which galaxies are located.

For example, Dressler (1980), through the study of 55 clusters, found that the frequencies of elliptical and S0 (early-type) galaxies increases with local galaxy density (see Figure 1.1), while spiral and irregular (late-type) galaxies are more frequent in low-density environments (see also e.g. van der Wel et al. 2007, Holden et al. 2007). This Morphology-Density relation can be observed in clusters of galaxies up to $z = 1.5$ (Dressler et al. 1997, Postman et al. 2005, Mei et al. 2012). Interestingly, Dressler et al. (1997) (but see also Vulcani et al. 2011) found that S0 galaxies are less frequent at high redshifts, while spiral galaxies become more abundant. This result has been interpreted as evidence for morphological transformation from spiral to S0.

It is now known that the morphology of galaxies is related to other physical properties which also evolve with time. For instance, early-type galaxies tend to have higher masses, red colours and little or no star formation, while late-type galaxies tend to be blue, with high star formation and more abundant at low stellar masses (see e.g. Schawinski et al. 2014, Vulcani et al. 2011).

These relationships between morphology and stellar populations of galaxies have led astronomers to investigate the links between them and the environment in which galaxies reside. Thus, it is observed that there is a SFR vs density relationship which holds in clusters up to $z = 1.5$. This relation shows that there is a higher fraction of galaxies that are less star-forming in high-density environments than in low-density environments (Poggianti et al. 1999, Poggianti et al. 2006). There is evidence that the correlation between SFR and local density weakens or reverses at $z > 1.5$, when clusters had recently assembled or were still in their assembly process (Tran et al. 2010, Alberts et al. 2014).

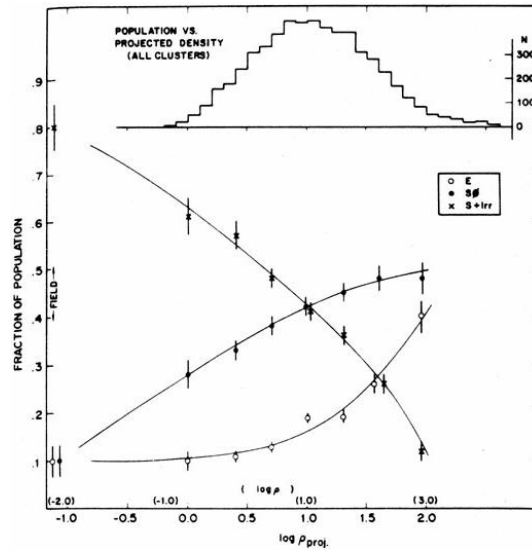


Figure 1.1 The morphology-Density Relation shows that the fraction of early-type galaxies (E) increases with the logarithm of the projected density, in galaxies Mpc^{-2} , while fraction of late-type galaxies (S + Irr) decreases comparatively in a high-density environment. The histogram shows the number distribution of the galaxies over the bins of projected density. Source: Dressler (1980)

Dressler et al. (1999) showed that at $z \sim 0.4$ the quenching of star formation is more efficient in clusters than in the field, a conclusion that is in agreement with Muzzin et al. (2012), who investigated clusters at $z \sim 1$. Similarly, Gobat et al. (2008), studying the star formation history (SFH) of galaxies in clusters and in the field at $z = 1.2$, found that early-type galaxies with similar stellar masses quenched star formation 0.5 Gyr earlier in clusters than in the field.

George et al. (2011) found that at $0.2 < z < 1.0$ the fraction of red galaxies in intermediate density environments such as groups is $\sim 20\%$ higher than in the field at fixed stellar mass. Moreover, they found that some galaxy groups exhibit an increase in the star formation activity of their galaxy members. Star formation is shown to be triggered by the compression of the interstellar gas resulting from the interactions of the galaxies with their surrounding companions in the groups (Ellison et al. 2010, Torres-Flores et al. 2014b). In particular, Torres-Flores et al. (2014b) and Olave-Rojas et al. (2015) study the properties of interacting galaxies, detecting young star-forming regions with ages younger than 10 Myr that have blue colours in the optical and are characterized by emission line spectra (Figure 1.2). The young ages of these star-forming regions suggest that they were created within the galaxy as a consequence of the interactions with their companions (Chien et al.

2007, de Mello et al. 2008).

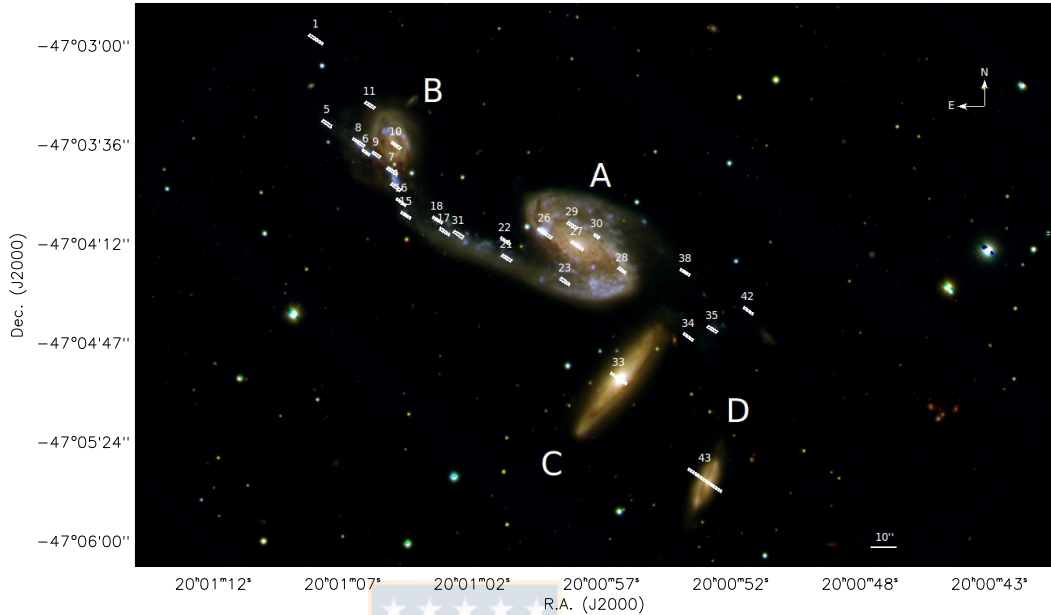


Figure 1.2 Interacting group NGC 6845 in a colour Gemini/GMOS obtained by combining u' , g' and r' images. White rectangles in the image indicate the nucleus of the main galaxies and the star-forming regions in the system. In particular, we note that rectangles in the tidal tail between NGC 6845A and NGC 6845B indicate the star-forming regions formed “in situ” due to the interaction between NGC 6845A and B. Source: Olave-Rojas et al. (2015)

The metallicity of galaxies is also affected by the environment in which they reside. Some authors (e.g. Kewley et al. 2010, Rupke et al. 2010b, Torres-Flores et al. 2014b, Bresolin et al. 2012, Olave-Rojas et al. 2015) studied the spatial distribution of the abundance of oxygen, a proxy for the gas-phase metallicity, in galaxies that are undergoing a gravitational interaction with their companions in groups. These works show that the spatial distribution of the gas-phase metallicity in interacting galaxies is different from that of isolated galaxies without signs of interaction (see e.g. Werk et al. 2011). The latter are indeed characterized by a negative metallicity radial gradient (see Figure 1.3), while the metallicity gradients of interacting galaxies are negative only in their innermost regions ($r \leq r_{25}^1$). In the outskirts ($r > r_{25}$) these galaxies exhibit a flat gradient (Figure 1.4).

The origin of the flat gradient has been explained in theoretical works as resulting

¹The optical radius is defined as the radius of the isophote at which the surface brightness has the value of 25 mag/arcsec^2 in the B-band (Schneider, 2006)

from the flow of metal-poor gas towards the centres of the galaxies (Rupke et al. 2010a, 2010b, Perez et al. 2011). On the other hand, the formation of new stars triggered by the interaction contribute with new chemical elements and could increase the metallicity of the interstellar medium (ISM) in the outskirts, principally through supernova feedback (Perez et al., 2011).

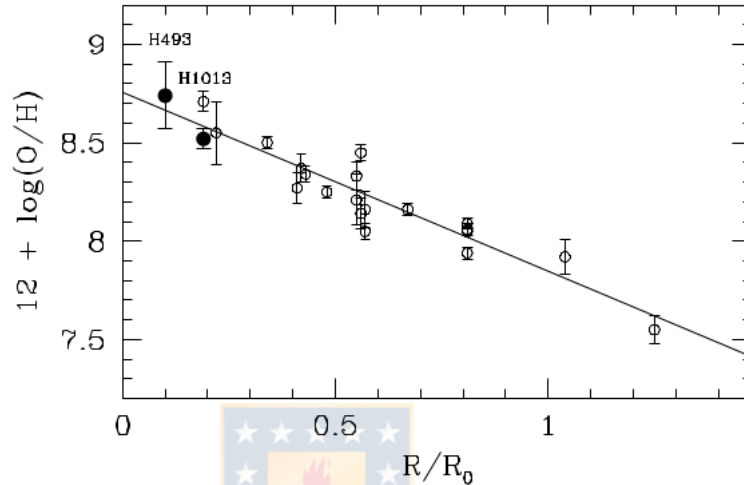


Figure 1.3 The observed metallicity profile with radius for M101 as traced by the gas phase oxygen abundance as a function of distance from the galaxy centre. M101 is characterized by a negative metallicity radial gradient. R_0 corresponds to the optical radius of the galaxies. Source: Bresolin (2007)

Many physical mechanisms have been proposed to explain the changes that are observed in the properties of galaxies that reside in different environments. All these mechanisms have been studied in theoretical works and can both promote or quench star-formation. They can originate within the galaxies (AGN and supernova feedback, star-formation feedback) or outside (heating of the halo gas, interactions with other galaxies and with the intracluster or intragroup medium). Although internal and external mechanisms independently affect the star formation activity of galaxies, in the densest environments, such as the cores of galaxy clusters or compact groups, internal processes may be activated by galaxy interactions.

The main external mechanisms which affect the properties of galaxies in groups and clusters are ram-pressure stripping by the intracluster medium (Gunn & Gott, 1972). The ram-pressure stripping removes the gas of the galaxies when they fall into the cluster and travel through the intracluster medium (ICM). Gravitational interactions among galaxies

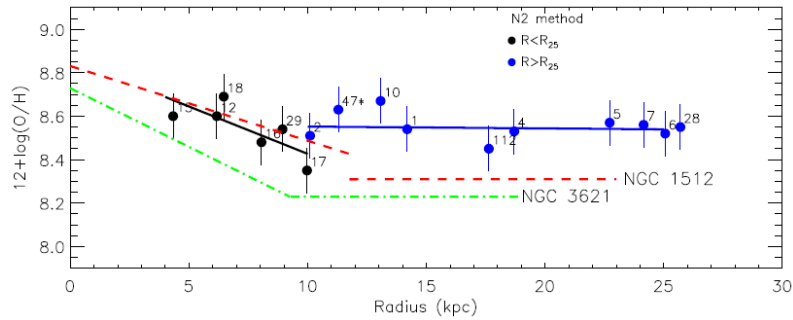


Figure 1.4 The observed metallicity profile with radius for NGC92 as traced by the gas phase oxygen abundance as a function of distance from the galaxy centre. NGC92 has a negative metallicity gradient only in its innermost regions ($r \leq r_{25}$), while in the outskirts ($r > r_{25}$) NGC92 exhibits a flat gradient. R_{25} corresponds to the optical radius of the galaxies. Source: Torres-Flores et al. (2014b)

such as tidal interactions (Toomre & Toomre, 1972) and merger between galaxies (Mihos, 2003), which are expected to be more frequent in groups. Tidal interactions can trigger star-formation and modify the metal content of galaxies (Kewley et al. 2010, Perez et al. 2011) and mergers between galaxies can form an S0 galaxy (Bekki, 1998) or to produce giant ellipticals (Naab & Burkert, 2003), depending on the relationship between the masses of the merging galaxies. Galaxy harassment (Moore et al. 1996, 1999) is the accumulation of numerous high-speed encounters between galaxies in clusters. Galaxy harassment can exhaust the gas due to a burst of star-formation or strip the neutral atomic hydrogen (HI) from galaxies (Duc & Bournaud, 2008). Finally, tidal interactions between galaxies and the gravitational potential of the cluster (Larson et al. 1980, Miller 1986, Byrd & Valtonen 1990) can compress the gas, inducing inflows and triggering star-formation.

1.2 Groups and Clusters of Galaxies as Cosmic Laboratories

Clusters of Galaxies are the most massive bound cosmic structures. They host a broad variety of environments in which galaxies may form and evolve. In general a cluster is characterized by a density profile which is well fitted by a Navarro et al. (1997) (NFW) function: the density is highest in the core and decreases towards the outskirts. The

cores of clusters are highly virialised, while in the outskirts the dynamical equilibrium is perturbed by the infall of galaxies and groups from the field or by the interactions with neighbouring clusters.

Because of their density profiles, the morphology-density relations introduced in Section 1.1 can be translated into a morphology vs cluster-centric distance relation (Whitmore et al. 1993, Goto et al. 2003, Postman et al. 2005, also see right panel of Figure 1.5). A similar reasoning can be applied to the SFR vs density relationship, and so it is observed that at least up to $z = 1.5$, the SFR of galaxies increases with the distance from the cluster centre (Lewis et al., 2002).

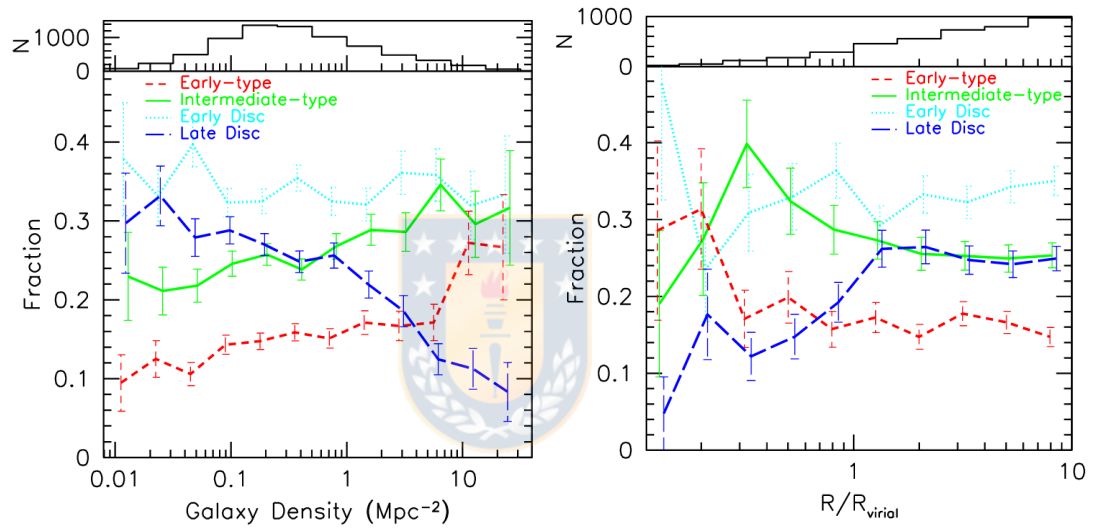


Figure 1.5 Morphology-density and morphology-clustercentric radius relations. The red short-dashed, green solid, cyan dotted and blue long-dashed lines represent early-type, intermediate-type, early-disc and late-disc galaxies, respectively. The histogram in the upper panel shows the numbers of galaxies in each bin of density or clustercentric radius. Left panel: Morphology-density relation shows that the fraction of early-type galaxies slightly increases with increasing density and quickly increases at the two highest-density bins, while the fraction of late-disc declines toward high density. Right panel: Morphology-clustercentric radius relation shows that the fraction of early-type and intermediate galaxies increase toward a cluster centre, while the fraction of late-disc galaxies decrease toward a cluster centre. Source: Goto et al. (2003)

The broad variety of environments of galaxy clusters allows one to use them as cosmic laboratories for the study of the environmental drivers of galaxy evolution. As discussed in Section 1.1, there are many environmental mechanisms that have been proposed as environmental drivers of galaxy evolution; however, it is not clear what are the dominant

mechanisms and in which environmental regime a certain mechanism prevails over the other. In clusters one can study galaxy properties in different environment, and so one can try to distinguish between various pathways in the evolution of galaxies.

The Λ cold dark matter (Λ CDM) structure formation paradigm explains the formation of clusters of galaxies as a gradual assembly in which several group-like structures are accreted on to a more massive structure (Press & Schechter 1974, Fakhouri et al. 2010, Chiang et al. 2013). This merging process is well represented by a tree (Figure 1.6) in which the trunk represent the final product and the branches are the dark matter haloes that are accreted on to the main halo. The traces of this accretion are detectable in clusters as substructures that arise in the velocity and position distribution of galaxies (e.g. Dressler et al. 2013) or in the distribution of the intracluster medium (e.g. Bianconi et al. 2018).

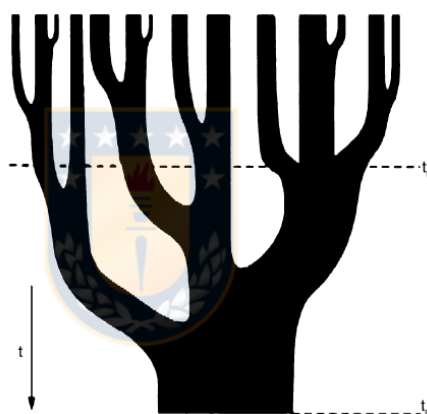


Figure 1.6 Typical scheme of merger tree in the Λ CDM hierarchical scenario of structure formation. The time axis runs from top to bottom. t_0 corresponds to the present epoch where a massive halo has been formed by continuous mergers of halos of lower mass and t_f is the time of halo formation and it corresponds to the time at which a sub-halo had reached half the mass that has the final massive halo at t_0 period. Source: Schneider (2006)

Several theoretical works show that clusters of galaxies at the present epoch accreted up to 40% of their galaxies through the accretion of groups, suggesting that the study of the properties of galaxies in substructures and their comparison with the properties of galaxies in the main cluster is fundamental to understand the relationships between the evolution of galaxies and the formation histories of their hosting large-scale structures.

For instance, Fujita (2004) used an analytical model based on the hierarchical structure formation paradigm to study the evolution of disk-dominated galaxies in substruc-

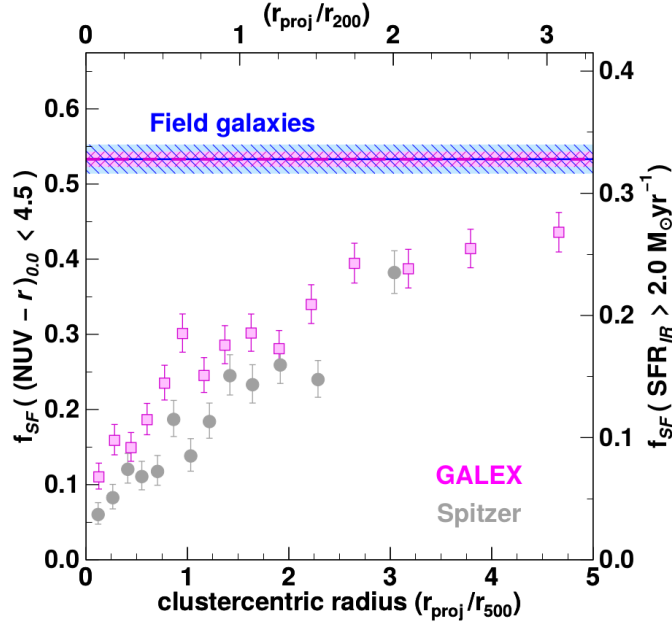


Figure 1.7 Fraction of star-forming galaxies as a function of projected distance from the cluster centre normalized by r_{200} and r_{500} in the top and bottom axis, respectively. The fraction of star-forming galaxies was estimated in a sample of 30 clusters at $0.15 < z < 0.30$ using data from the Galaxy Evolution Explorer (GALEX, Martin et al. 2005) in the Near Ultraviolet and *Spitzer* (Werner et al., 2004) at $24\mu\text{m}$. Magenta squares show the fraction of massive ($M_{\star} > 2 \times 10^{10} M_{\odot}$) star-forming galaxies in clusters with $(NUV - r)_{0.0} < 4.5$. Grey dots represent the fraction of star-forming galaxies with $SFR_{IR} > 2 M_{\odot} \text{yr}^{-1}$. The magenta dashed line and magenta shaded region correspond to the fraction of star-forming galaxies in the field and its 1σ confidence levels, respectively, estimated using GALEX data. The blue dashed line and blue shaded region represent the fraction of star-forming galaxies in the field and its 1σ confidence levels, respectively, estimated using data from *Spitzer*. The fraction of star-forming galaxies in the field was estimated using the same criteria of the cluster galaxies. Fraction of star-forming galaxies in cluster is lower than in the field even at $r > 3 \times r_{200}$, suggesting that the pre-processing of galaxies is one feasible mechanism to explain the observed fraction in the outer region of the clusters. Source: Haines et al. (2015)

tures around a galaxy cluster. This author finds that substructure members were "pre-processed", i.e. they quenched star formation before their parent groups were accreted on to the cluster. This prediction has been corroborated in various observational works in which the star formation of galaxies in the outskirts of clusters was studied. Hou et al. (2014); Just et al. (2015); Haines et al. (2015), among others, find that the star formation activity of cluster galaxies out to $3 \times r_{200}$ from the cluster centre is lower than that of

galaxies in the field (Figure 1.7). These results cannot be explained by models in which star formation ceases only after the galaxy falls in to the virialised regions of the clusters and is consistent with the pre-processing scenario of Fujita (2004) (see also Vijayaraghavan & Ricker 2013).

1.3 The Pre-processing of Galaxies

With pre-processing it is indicated the termination of star formation in galaxies that were members of a group that was later accreted on to a cluster. A pre-processed cluster member is therefore a galaxy that is not forming stars and that was accreted in the cluster when it was already quiescent.

The hypothesis of pre-processing was first proposed in Zabludoff & Mulchaey (1998) to explain the fact that the fractions of star-forming and post-starburst early-type galaxies in groups are similar to the fractions of galaxies with the same spectral signatures in clusters that are rich in substructures. The authors claimed that members of cluster substructures terminated star formation as a result of environmental processes that are typical of groups (e.g. galaxy-galaxy interactions) and, therefore, that star-formation in those objects was quenched before their arrival in the cluster. Similarly, Cortese et al. (2006) showed that the members of a compact group that is falling in to the Abell 1367 cluster present disturbed morphologies and enhanced $H\alpha$ emission. They conclude that the environment of the group is affecting the properties of galaxies and that pre-processing may have played a significant role during the early stages of cluster assembly.

There are several theoretical works that support the pre-processing scenario and place it in to the general theoretical framework of galaxy formation and evolution. De Lucia et al. (2012) used semi-analytic models based on hierarchical structure formation to study the environmental history of group and cluster galaxies. They find that at $z = 0$ 55% of the quiescent galaxy population (defined as those with specific star formation rate $sSFR = SFR/M_{\star} \leq 10^{-11} \text{ yr}^{-12}$) were accreted already quenched from galaxy groups with masses $10^{13} M_{\odot}$. The same authors find that the accreted galaxies had been group members for 5-7 Gyr.

²The $sSFR$ threshold adopted by De Lucia et al. (2012) is defined observationally (e.g. Weinmann et al. 2010) and is used to separate galaxies in the star-forming sequence from passive galaxies, because this value corresponds roughly to the location of the minimum in the bimodal distribution of $sSFR$ s.

In a similar way Bahé et al. (2013) performed hydrodynamical simulations of groups and clusters of galaxies and studied their galaxy populations. They find that the fraction of star-forming galaxies in clusters is lower than that of the field out to $5 \times r_{200}$ from the cluster centre. Furthermore, these authors find that the fraction of pre-processed galaxies increases towards the cluster centre, from 30% at $5r_{200}$ to 65% at r_{200} .

Wetzel et al. (2013) studied groups and clusters of galaxies in the Sloan Digital Sky Survey Data Release 7 (SDSS-DR7; Abazajian et al. 2009) and in high-resolution cosmological N-body simulations. These authors find that at $z = 0 \sim 50\%$ of galaxies with stellar masses $< 10^{10} M_{\odot}$ in clusters with masses $> 10^{14} M_{\odot}$ were quenched in groups before these were accreted on to the clusters.

Theoretical works are important to understand the physics of galaxies within groups and clusters and allow one to understand the processes of interaction with the environment that lead group galaxies to be accreted on to a cluster when they are already quiescent. Furthermore, theoretical models and simulations may also help in designing observational strategies.

Vijayaraghavan & Ricker (2013) modelled the merger between a cluster and a group of galaxies. They show that galaxies that fall into the cluster directly from the field are generally star-forming, while those that fall in as members of the group may be already quenched as a result of environmental processes that happen within the group like ram-pressure stripping and galaxy-galaxy mergers. Thus, pre-processing is important in the evolution of cluster galaxies and must be taken in to account. Interestingly, these authors also show that the accreted group is not destroyed immediately after accretion and that its members can retain distinct kinematics from the other cluster galaxies.

As a consequence of that, it should be possible to identify accreted groups through the analysis of the peculiar motions and spatial distribution of cluster galaxies. Accreted groups should therefore be seen as substructures within the main body of the cluster. These are indeed the principles that have inspired several authors for the observational identification of accreted groups.

For example, Bianconi et al. (2018) used the distribution of the intracluster gas to identify accreted groups, which were detected as substructures in the profile of the X-ray light of the ICM. One limitation of this method is that only the most massive and dense accreted groups can be found.

One other largely used approach employs the peculiar motions of cluster members.

The Dressler-Schectman (DS) test (Dressler & Schectman, 1988) is a statistical test that allows one to estimate the amount of substructures within a cluster by analysing the line-of-sight peculiar velocities of cluster members (See Chapter 3 for details). When this is coupled with the study of the spatial distribution of galaxies, one can efficiently find substructures that correspond to low- and high-mass accreted groups (e.g. Hou et al. 2014, Jaffé et al. 2016). The limitation of this method is that one needs to have a large spectroscopic coverage of the clusters out to $2 - 3 \times r_{200}$ in order for it to be effective.

Dressler et al. (2013) detected substructures in clusters at $0.31 < z < 0.54$ in the ICBS with the spatial and kinematic analysis of the galaxy members and found that the fraction of quiescent and post-starburst galaxies increases with mass of the accreted groups. They suggest that star formation in these galaxies terminated as a result of merger and tidal stripping processes which happened within the groups prior to their fall in to the clusters.

Hou et al. (2014) applied a similar method to detect accreted groups in clusters of the SDSS DR7, and they found that the number of substructures increases with the mass of their host clusters. They also found that the fraction of quiescent galaxies in the substructures is higher than that in the field and in the sample of cluster galaxies that are not part of a substructure.

The observational and theoretical works summarised above show that up to 50% of the quiescent galaxy population in $z = 0$ clusters originated in groups prior to their accretion on to the clusters. This implies that half of the population of quiescent galaxies may be constituted of pre-processed systems and, therefore, that pre-processing plays an important role in the build-up of the red-sequence in the colour-magnitude diagram of galaxies.

It is thus important to couple the study of galaxies in clusters with the analysis of galaxies in groups as the processes that caused star-formation quenching in these systems may be different from those that quench star formation in clusters.

Groups are small systems of galaxies and are characterized by lower velocity dispersions compared to clusters. These conditions favour the occurrence of galaxy-galaxy tidal interactions and mergers which are less frequent in clusters and generate pathways for the evolution of structure and stellar populations that are different from those originated by ram-pressure stripping or strangulation.

Pre-processing thus represents a fundamental piece in the framework of galaxy evolution theories and in order to understand it, it is crucial to join the study of clusters of

galaxies with the detailed analysis of galaxy properties in groups.

1.4 Motivation and Outline of the Thesis

Motivated by the problems exposed and the results discussed in the previous sections of this Chapter, we embarked on a study of the physics of galaxies in groups and clusters with the aim of understanding the effect of the environment on their evolution and in particular the importance of the pre-processing in the quenching of star formation.

This Thesis is divided in two parts, the first concerning the study of two clusters at $z = 0.4$ from the CLASH-VLT survey and the second consisting the analysis of the properties of galaxies during an ongoing interaction in the $z = 0.01$ Arp 314 group. The principal goal of the Thesis is to provide a global and a local views of galaxy pre-processing, while more specific goals can be considered the following:

- identification of accreted groups within galaxy clusters;
- determination of the fractions of star-forming and quiescent galaxies in clusters and groups;
- study of the kinematics of galaxies that are gravitationally interacting with each other;
- determination of the relationships between galaxy properties and the environments that host them.

The Thesis is organised as follows. Chapter 2 describes the data used in the analyses of Chapters 3 and 4. Chapter 3 presents the study of the two $z = 0.4$ clusters MACS J0416.1-2403 and MACS J1206.2-0847 published as a paper in Monthly Notices of the Royal Astronomical Society (MNRAS) (Olave-Rojas et al., 2018). In Chapter 4 we present the study of the properties of interacting galaxies in the Arp 314 group (paper submitted to MNRAS, Torres-Flores et al.), while in Chapter 5 we summarise the main results of the Thesis and give an overview of the prospects generated by this work for the future. Finally, in the Appendix, we give the data tables obtained the analysis presented in Chapter 3.

Throughout this Thesis, magnitudes are refereed in the AB system (Oke, 1974), unless otherwise stated. r_{200} represents the physical radius, measured in Mpc, inside which the

matter density is 200 times the critical density of the Universe at the redshift of each cluster or group considered.



2

Sample and Data Description

This chapter gives a description of the sample and data used in the analysis presented in this Thesis in Chapters 3 and 4. The present Chapter is organised as follows: Section 2.1 introduces the sample of clusters used in Chapter 3, where we present the study of galaxy pre-processing, while Section 2.2 introduces the group Arp 314 and the data used in Chapter 4, dedicated to the analysis of galaxy interactions in groups. Finally, Section 2.3 gives a brief description of the COSMOS/UltraVISTA sample used in Chapter 3 for comparison between cluster and field galaxies and statistical background subtraction.

2.1 Clusters Sample

2.1.1 MACS J0416.1-2403 and MACS J1206.2-0847

Chapter 3 of this Thesis presents a detailed analysis of galaxy properties in two clusters at $z \sim 0.4$, namely MACS J0416.1-2403 and MACS J1206.2-0847 (hereafter MAC0416 and MACS1206, respectively). These clusters were discovered and observed for the first time in X-rays as part of the MAssive Cluster Survey (MACS, Ebeling et al. 2001). The masses of the two clusters have been estimated in several independent works through gravitational lensing or galaxy peculiar motions and span the ranges $1.2 - 1.3 \times 10^{15} M_{\odot}$ (MACS0416, Umetsu et al. 2014, Umetsu et al. 2016) and $1.2 - 1.6 \times 10^{15} M_{\odot}$ (MACS1206, Biviano et al. 2013, Umetsu et al. 2014, Merten et al. 2015, Barreira et al. 2015). The typical fractional uncertainty in the masses is 5%, which depends on the model fitted (typically Einasto 1965 and Navarro et al. 1995) to the mass profile derived from gravitational lensing.



Figure 2.1 Galaxy cluster MACS J0416.12403. This image shows the Hubble’s view of the central region ($r < r_{200}$) of MACS J0416.1-2403. The image has a field of view of 3.38×3.24 arcmin² and the north is 23.1° left of vertical Source: ESA/Hubble, NASA, HST Frontier Fields, M. Postman (STScI), and the CLASH Team.

MACS0416 is a galaxy cluster at $z = 0.396$ with an irregular X-ray morphology. It consists of two main subclusters and at least two secondary structures around the main subclusters (see Figure 2.1¹, Mann & Ebeling 2012, Jauzac et al. 2015, Balestra et al. 2016). Mann & Ebeling (2012) observed MACS0416 with *Chandra*, and they found that the projected separation between the brightest cluster galaxies (BCGs) in two main subclusters is 200 kpc. Following this result, these authors suggest that the two main subclusters of MACS0416 are in a post-collisional phase. O’grea et al. (2015) and Balestra et al. (2016), on the other hand, using observations from *Chandra* and the Jansky Very Large Array (JVLA) coupled with the mass profile of the cluster obtained from strong and weak gravitational lensing, do not find a significant offset between the centroid of the spatial distribution of the hot X-ray emitting intracluster gas (ICM) and the centre of the dark matter density profile. Such a result supports the notion that the system is in a

¹<https://www.spacetelescope.org/images/heic1416a/>



Figure 2.2 Galaxy cluster MACS MACS J1206.2-0847. This image shows the Hubble's view of the central region ($r < r_{200}$) of MACS J1206.2-0847. The image has a field of view of 2.78×2.52 arcmin² and the north is 0.0° left of vertical Source: ESA/Hubble, NASA, M. Postman (STScI), and the CLASH Team.

pre-collisional phase of the merger.

MACS1206 is a massive and X-ray luminous cluster at $z = 0.440$, which was discovered and observed for the first time in X-rays as part of the MACS survey (Ebeling et al. 2001, 2009). In optical (see Figure 2.2²) and X-ray images this cluster appears regular, without signs of ongoing mergers, and the X-ray emission peaks at the location of the BCG (Ebeling et al., 2009). Although MACS1206 appears relaxed, Eichner et al. (2013) found significant amounts of intracluster light (ICL) concentrated outside the cluster centre, suggesting that this cluster has small overdensities. Girardi et al. (2015) performed a structural analysis of MACS1206 using the peculiar motions of cluster members, and they found that the cluster is a large-scale relaxed system, especially within r_{200} , with few secondary overdensities.

MACS0416 and MACS1206 represent two opposite cases of clusters of galaxies, one being an ongoing merger and the other a relaxed system. With the two clusters being at similar redshifts, their different dynamical states allow us to investigate of the dependence of star formation quenching on cluster assembly. It is for this reason that we chose these

²<https://apod.nasa.gov/apod/ap111017.html>

two clusters from the Dark Matter Mass Distributions of Hubble Treasury Clusters and the Foundations of Λ CDM Structure Formation Models survey (CLASH-VLT, Rosati et al. 2014) in this Thesis. We describe the data used in the study of the two clusters in the following section.

2.1.2 The MACS0416 and MACS1206 data-sets

Photometry

CLASH is a Multi-Cycle Treasury programme carried out with the *Hubble Space Telescope* (HST) which targeted 25 massive ($M_{halo} \gtrsim 10^{14.5} M_{\odot}$) clusters at redshift $0.2 < z < 0.9$ (see Table 2.1) over a 2.7 year period (Nov 2010 - July 2013). The main goals of the survey are the mapping of the distribution of dark matter in galaxy clusters using strong and weak gravitational lensing, and the detection of distant galaxies at $z > 7$. Four-fifths (20 out of 25) of the clusters were selected in X-rays (*X-ray Selected Clusters*), while the remaining 1/5 of the sample was selected based solely on the exceptional strength of their gravitational lenses (*High Magnification Clusters*). All clusters in the CLASH sample were observed using the Wide Field Camera 3 (WFC3, Kimble et al. 2008) and the Advanced Camera for Surveys (ACS, Clampin et al. 1996) in 16 broadband filters spanning the near-ultraviolet (NUV) to near-infrared (NIR) ($\sim 0.2 - 1.6 \mu\text{m}$). The HST observations cover only up to $\sim 1 \times r_{200}$ from the cluster centre. The exposures times, limiting magnitudes and extinction coefficients in each filter are listed in the Table 5 of Postman et al. (2012).

In addition, all clusters in the CLASH survey, with the exception of RXJ2248.7-4431, were observed with the SuprimeCam (Miyazaki et al., 2002) at the prime focus of the 8.3m Subaru Telescope in at least three optical bands from B to z (see Table 2.1). The clusters Abell 1423 and MACS1311.0-0310 were observed only in two and one optical bands (see Table 2.1 and Postman et al. 2012). The wide $34' \times 27'$ field of view (FOV) of SuprimeCam allowed the observations to reach out to the outskirts ($3 \times r_{200}$) of the clusters.

The Subaru CLASH data are available in the Subaru archive (Subaru-Mitaka Okayama-Kiso Archive System, SMOKA³; Baba et al. 2002). Each cluster was observed with exposures times ranging from 1000 to 10000 seconds in each filter, and the mean seeing of

³<http://smoka.nao.ac.jp>

Table 2.1 The CLASH Cluster Sample

Cluster	R.A. ^a J2000.0	Dec. ^a	z_{cl}	r_{vir}^b Mpc h ⁻¹	SuprimeCam Filters
X-ray Selected Clusters:					
Abell 209*	01:31:52.57	-13:36:38.8	0.209	1.95	BVR_cI_cz
Abell 383*	02:48:03.36	-03:31:44.7	0.187	1.86	BVR_cI_cz
MACS0329.7-0211*	03:29:41.68	-02:11:47.7	0.450	1.54	BVR_cz
MACS0429.6-0253	04:29:36.10	-02:53:08.0	0.399	1.65	VR_cI_c
MACS0744.9+3927	07:44:52.80	+39:27:24.4	0.686	1.33	BVR_cI_cz
Abell 611	08:00:56.83	+36:03:24.1	0.288	1.79	BVR_cI_cz
MACS1115.9+0129*	11:15:52.05	+01:29:56.6	0.352	1.78	BVR_cI_cz
Abell 1423	11:57:17.26	+33:36:37.4	0.213	VI_c
MACS1206.2-0847*	12:06:12.28	-08:48:02.4	0.440	1.63	BVR_cI_cz
CLJ1226.9+3332	12:26:58.37	+33:32:47.4	0.890	1.57	BVz
MACS1311.0-0310*	13:11:01.67	-03:10:39.5	0.494	1.28	R_c
RXJ1347.5-1145*	13:47:30.59	-11:45:10.1	0.451	1.80	BVR_cI_cz
MACS1423.8+2404	14:23:47.76	+24:04:40.5	0.545	1.34	BVR_cI_cz
RXJ1532.9+3021	15:32:53.78	+30:20:58.7	0.345	1.47	BVR_cI_cz
MACS1720.3+3536	17:20:16.95	+35:36:23.6	0.391	1.61	BVR_cI_cz
Abell 2261	17:22:27.25	+32:07:58.6	0.224	2.26	BVR_c
MACS1931.8-2635*	19:31:49.66	-26:34:34.0	0.352	1.61	BVR_cI_cz
RXJ2129.7+0005*	21:29:39.94	+00:05:18.8	0.234	1.65	BVR_cI_cz
MS2137-2353*	21:40:15.18	-23:39:40.7	0.313	1.89	BVR_cI_cz
RXJ2248.7-4431*	22:48:44.29	-44:31:48.4	0.348
				1.92	
High Magnification Clusters:					
MACS0416.1-2403*	04:16:09.39	-24:04:03.9	0.396	BR_cz
MACS0647.8+7015	06:47:50.03	+70:14:49.7	0.584	BVR_cI_cz
MACS0717.5+3745	06:47:50.03	+37:45:18.5	0.548	BVR_cI_cz
MACS1149.6+2223	11:49:35.86	+22:23:55.0	0.544	BVR_cI_cz
MACS2129.4-0741*	21:29:26.06	-07:41:28.8	0.570	BVR_cI_cz

^a Central cluster coordinates taken from Table 3 published by Postman et al. (2012).

^b Virial Radius taken from Table 6 published by Merten et al. (2015).

* Clusters in the CLASH-VLT sample.

the observations in the R_c -band varied in the range 0.6 - 0.8 arcsec (Umetsu et al., 2014). Typical limiting magnitudes in the R_c -band, defined as the 3σ limit for a $2''$ diameter aperture are of the order 26.0 mag (Umetsu et al., 2014). The Subaru observations were centred on the cluster centroid.

The images obtained with the Subaru Telescope were reduced by the CLASH team following standard steps of reductions including bias subtraction and flat-field correction. Data reduction was performed with the MSCRED task in the Image Reduction and Analysis Facility (iraf⁴) following the procedure outlined in Nonino et al. (2009). Details on the reduction of the CLASH Subaru data can be found in Umetsu et al. (2012) and Medezinski et al. (2013).

In the analysis developed in Chapter 3 we used the Subaru photometric catalogues

⁴IRAF is distributed by the National Optical Astronomy Observatories (NOAO). NOAO is operated by the Association of Universities for Research in Astronomy, Inc., under a cooperative agreement with the National Science Foundation.

of MACS0416 and MACS1206 and the photometric redshifts estimated in the fields of those two clusters. The photometric catalogues were generated by the CLASH-VLT team (see Mercurio et al. 2016) using the software SExtractor (Bertin & Arnouts, 1996) in conjunction with PSFEx (Bertin, 2011). Aperture magnitudes were measured within fixed circular apertures with diameters 3'' and 5'' for MACS 0416 and MACS1206, respectively. All aperture magnitudes in the catalogues were corrected for Galactic Extinction and zero-point shifts simultaneously by comparing the galaxy observed colours to the stellar library of Pickles (1998) and using the Galactic extinction maps of Schlafly & Finkbeiner (2011).

The CLASH-VLT team estimated the photometric redshifts only in MACS1206, because MACS0416 was observed in only three Subaru bands (see Table 2.1). Photometric redshifts were estimated using the aperture magnitudes and employing a Neural Network based algorithm called Multi Layer Perceptron with Quasi Newton Algorithm (MLPQNA; Brescia et al. 2013). A full description of the derivation of photometric redshifts for MACS1206 is given in Biviano et al. (2013) and Mercurio et al. (2014).

MACS0416 was also observed with the Wide-Field Imager (WFI; Baade et al. 1999) on the European Southern Observatory (ESO) 2.2m Max Planck Gesellschaft Telescope (MPG) at the La Silla Observatory in Chile. The WFI camera has a FOV of 34' × 33', and the observations were centered on the cluster core. MACS0416 was observed in the B, V, R and I-bands. Images and catalogues with aperture magnitudes in each band and photometric redshifts were published in Gruen et al. (2014) and are available in the web page of D. Gruen⁵.

The reduction of the WFI images was performed by Gruen et al. (2014) following the procedures described in Gruen et al. (2013). All images were corrected for bias, flat field and bad pixels using the Astro-WISE⁶ pipeline (Valentijn et al., 2007). Background subtraction, astrometry and co-addition of the images were done using scamp⁷ (Bertin, 2006) and SWARP⁸ (Bertin, 2010). A full description of the reduction of WFI images is given in Gruen et al. (2013, 2014).

Aperture magnitudes in each filters were estimated in a fixed circular aperture with a diameter of 2'' using SExtractor and PSFEx. Magnitudes were corrected for Galactic extinction and zero-point shifts using the Galactic extinction maps of Schlegel et al.

⁵<http://www.usm.uni-muenchen.de/~dgruen/download.html>

⁶<http://www.astro-wise.org/>

⁷<http://www.astromatic.net/software/scamp>

⁸<http://www.astromatic.net/software/swarp>

(1998) and minimizing the residuals between the observed colours and the synthetic colours obtained using the stellar library of Pickles (1998). Photometric redshifts were estimated by Gruen et al. (2014) using a photometric template-fitting algorithm developed by Bender et al. (2001). Details on the estimation procedure for photometric redshifts are in Brimiouille et al. (2013) and Gruen et al. (2013; 2014).

Summarising, in the analysis presented in Chapter 3 we use the photometric catalogues obtained by the CLASH-VLT team (see Mercurio et al. 2014; 2016) and Gruen et al. (2014). These catalogues include multi-band aperture photometry and photometric redshifts.

Spectroscopy

The CLASH-VLT survey is a spectroscopic large programme (186.A-0.798; P.I.: P. Rosati; Rosati et al. 2014) carried out with the Visible Multi-Object Spectrograph (VIMOS; Le Fèvre et al. 2003) on the ESO 8.2m Very Large Telescope (ESO/VLT) with the aim of obtaining at least 500 spectroscopic members in each of 13 CLASH clusters observable from the Southern Hemisphere at redshifts $0.2 < z < 0.6$ to reconstruct the cluster mass profile with dynamical analyses. The median redshift of the CLASH-VLT sample is $z \sim 0.4$.

The VIMOS observations were made in four separated pointings centered on the cluster cores and using Low-Resolution Blue (LR-Blue) and Medium-Resolution (MR) masks. In order to maximise the number of targets per pointing it was chosen a slit width of $1''$ and a slit length shorter than $6''$ (the standard length of slits in VIMOS), which allowed for the arrangement of more than 500 slits in each mask (Balestra et al., 2016). The LR mask has spectral coverage $3760 - 6700 \text{ \AA}$ with resolving power $R = 180$, while the MR mask has spectral coverage $4800 - 10000 \text{ \AA}$ with a resolving power $R = 580$. MACS0416 was observed in a total of 21 masks (15 LR-Blue and 6 MR), while MACS1206 was observed in a total of 12 masks (8 LR-Blue and 4 MR). The exposure times of the observations varied between 30 and 60 minutes per mask. Spectroscopic targets were selected using Subaru photometry and applying cuts in colour-colour space. This allowed a high chance of observing cluster members with the inclusion of blue galaxies to be accomplished (see Balestra et al. 2016). A full description of the spectroscopic observations of MACS0416 and MACS1206 can be found in Balestra et al. (2016) and Biviano et al. (2013), respectively.

The VIMOS spectroscopic observations have an area of $26' \times 23'$ around the centre of each cluster, covering almost entirely the FOV of Subaru, and were reduced by the CLASH-VLT team following the standard reduction steps of Multi-Object Spectroscopic (MOS) data using the VIMOS Interactive Pipeline Graphical Interface (VIPGI, Scodreggio et al. 2005).

Spectroscopic redshifts were estimated by the CLASH-VLT team using the software Easy Redshift (EZ, Garilli et al. 2010), which performs an automatic cross-correlation between the observed spectrum and template spectra of S0, Sa, Sb, Sc, and elliptical galaxies at low redshift, and Lyman break galaxies and quasars at high redshift. The solutions given by EZ were inspected visually and modified in cases of failures of the cross-correlation. Uncertainties on the redshifts are in the range $75 - 150 \text{ km s}^{-1}$ depending on the resolving power of the mask and on the number of spectra in which the mean redshift is estimated (see Biviano et al. 2013, Annunziatella et al. 2014, Balestra et al. 2016).

During the visual inspection of the spectra a Quality Flag (QF) was assigned to each redshift. Four redshift quality classes were defined, namely “secure” (QF = 3), “likely” (QF = 2), “insecure” (QF = 1) and “emission-line” (QF = 9). Spectra with QF = 3 are characterised by several emission lines and/or strong absorption features, spectra with QF = 2 have at least two spectral features well identified, spectra with QF = 1 are spectra with low signal-to-noise ratio (SNR), and finally spectra with QF = 9 have a single emission line. Spectroscopic redshifts are correct with a confidence $> 99.99\%$, 92% , 75% and $< 40\%$, for QF = 3, QF = 2, QF = 1 and QF = 9, respectively (Balestra et al., 2016).

In addition, the central region ($r \leq r_{200}$) of MACS0416 was observed with the Multi Unit Spectroscopic Explorer (MUSE, Bacon et al. 2012) as part of the Hubble Frontier Fields (HFF, Koekemoer et al. 2014, Lotz et al. 2017). The MUSE spectroscopic observations were reduced by Caminha et al. (2017) in a standard way using the MUSE reduction pipeline version 1.2.1, and spectroscopic redshifts were measured independently using EZ and SpecPro Masters & Capak (2011). The new redshifts were added to the redshifts obtained with VIMOS. A QF was assigned to each redshift following the same scheme described above.

The Spectroscopic catalogues of MACS0416 and MACS1206 have magnitude limit $R_c = 24.0 \text{ mag}$ and are available on the web page of CLASH-VLT⁹. The spectroscopic

⁹<https://sites.google.com/site/vltclashpublic/data-release>

catalogues have 4594 and 2736 galaxies for MACS0416 and MACS1206, respectively (Biviano et al. 2013, Balestra et al. 2016, Caminha et al. 2017). A detailed description of the CLASH-VLT redshift catalogues can be found in Biviano et al. (2013), Mercurio et al. (2014), Balestra et al. (2016) and Caminha et al. (2017).

2.2 The Arp 314 Group

Arp 314 is a group of three interacting galaxies (see Figure 2.3) at $z = 0.01$. Two galaxies have a spiral-like morphology (Arp 314-1 and Arp 314-2), while Arp 314-3 is an irregular galaxy. The central coordinates (J2000.0) of the system are R.A. $22^h58^m04^s$ and Dec. $-03^d47.4^m0^s$. Arp 314 is classified as a compact group of galaxies (Garcia, 1995) because the median separation between galaxies is 23 kpc, which is within the maximum spacing between galaxies in compact groups (see e.g. McConnachie et al. 2009, Sohn et al. 2015).

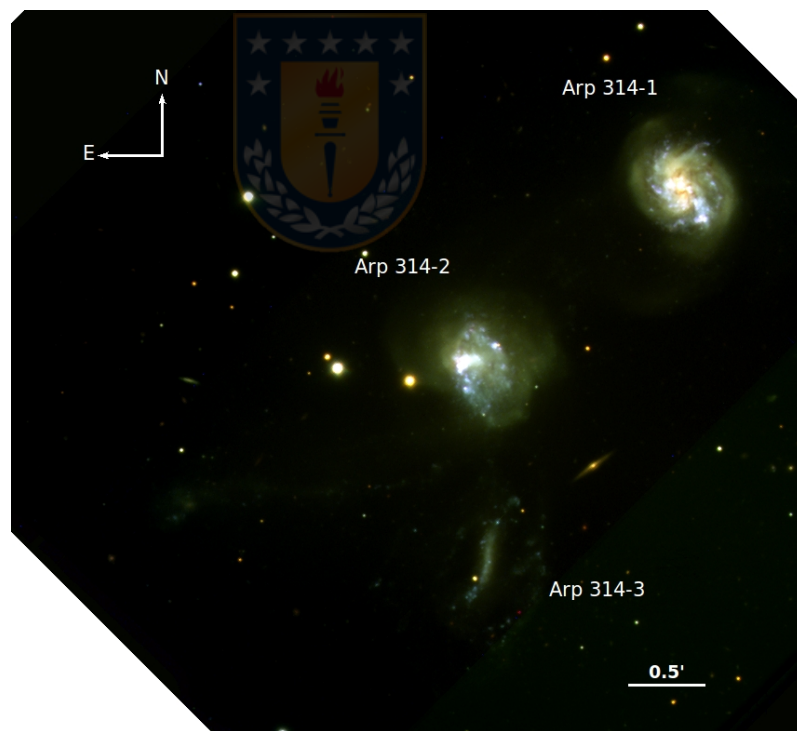


Figure 2.3 The Arp 314 group of interacting galaxies in a Gemini/GMOS colour composite image. This image was obtained combining the u' , g' and r' images.

Arp 314 was observed for the first time using the 200-inch telescope on the Palomar Observatory (Vorontsov-Velyaminov 1959, Arp 1966). Arp (1966) classified this group

as a pair of spiral galaxies (Arp 314-1 and Arp 314-2) with the number 314 on his “Atlas of Peculiar Galaxies”. Arp (1966) also mentions a faint filament between the galaxies of the group. Later, several authors studied and described the morphological and spectral properties of the Arp 314 galaxies. Thus, Dahari (1985) describes Arp 314 as a pair of spiral galaxies (Arp314-1 and Arp314-2) with faint tails and a connecting arm, while Keel et al. (1985) found that Arp 314-2 displays spectral features consistent with a “starburst” galaxy.

In addition, Nordgren et al. (1997) observed Arp 314 with the Very Large Array (VLA) Telescope to study the distribution of H α in the galaxies. These authors found that there is a large H α envelope that surrounds the galaxies in the group. Furthermore, Nordgren et al. (1997) found that there is a third small galaxy (Arp 314-3, see Figure 2.3) at the south of Arp 314-1 and Arp 314-2 that could be part of the group. Using the information of the H α velocity fields Nordgren et al. (1997) found that Arp 314-1 is experiencing a direct encounter with Arp 314-2, and also suggest that Arp 314-3 would seem to be in a direct encounter with Arp 314-2. These interactions could explain the perturbed morphology of the galaxies and the H α tidal tail. Torres-Flores et al. (2014a) using H α Fabry-Perot data cubes to study the kinematics of the galaxies of Arp 314, found that the single galaxies in Arp 314 have H α maps with a complex shape and perturbed velocity fields due to the interactions between galaxies. Arp 314 is therefore a system of galaxies undergoing an interaction and for this reason it represents a good case for the detailed study of environmental drivers of galaxy evolution.

2.2.1 Arp 314 Observations and Data

Gemini Multi-Object data

Images and spectra in Arp 314 were observed using the Gemini MultiObject Spectrograph (GMOS, Hook et al. 2004) at the Gemini South Observatory, under the observing programme GS-2013B-Q-27 (PI: S. Torres-Flores). Images were taken in August 2013 and spectroscopic observations were carried out in November 2013 in queue mode.

Arp 314 was observed in the u' , g' and r' -band filters with exposure times of 5×300 s, 4×300 s, and 3×300 s, respectively. Images in each filter were taken adopting a dithering pattern that corrected for the detector gaps and cosmic rays. All images were observed using an instrumental position angle of 135° and with a 2×2 binning mode, which allows

one to increase the readout speed of the CCDs. The camera has three detectors of 2048×4068 pixels each and a FOV of 5.5×5.5 arcmin². The 2×2 binning pixel scale is 0.146 arcsec/pixel.

We used the u' , g' and r' images to select the bluest regions in the group. These regions were selected by visual inspection of a false colour image that we built by combining u' , g' and r' images (see Figure 2.3).

Once the sources were selected, the mask for the GMOS spectroscopic observations of the regions of interest (star-forming regions within the galaxies) within the galaxies was designed. Since the sources are mostly point-like, we adopted slit widths of 1'' to maximise the amount of incoming light and minimise background contamination. The heights of the slits were set individually depending on the size of the selected source and also with the objective of maximising the number of observed regions. All slits were oriented according to the instrumental position angle used in the imaging observations.

The spectroscopic observations were made by performing four exposures of 1370 seconds each at three different central wavelengths (one in 5950 Å, two in 6000 Å and one in 6050 Å) to remove the gaps in the CCDs. This setup resulted in a spectral coverage of 3980 – 8960 Å. Spectra were taken using the R400 grating, which has a density of 400 lines/mm and a dispersion of 0.067 nm/pixel. The spectra in Arp 314 were observed with a binning of 2 pixels in the spatial axis and without binning in the spectral axis. Details of the spectroscopic observations are summarised in Table 2.2. To avoid any effect caused by instrumental flexure CuAr lamps and flat fields were observed after each science observation with the same position and central wavelengths as the science targets.

Central wavelengths and grating were chosen in order to detect principally the nebular emission lines of $H\beta$, $[OIII] \lambda 5007$ Å, $H\alpha$, $[NII] \lambda 6584$ Å. These lines are used to estimate the oxygen abundances using the $N2 \equiv \left(\frac{H\alpha}{[NII]}\right)$ and $O3N2 \equiv \left(\frac{H\alpha/[NII]}{H\beta/[OIII]}\right)$ empirical calibrators (Pettini & Pagel 2004, Marino et al. 2013), and also are used to analyse the excitation mechanisms through a diagnostic diagram (e.g. Baldwin et al. 1981, Cid Fernandes et al. 2011). The resolving power of the grating is $R = 1500$, and the resolution at $H\alpha$ is 4.5 Å.

The GMOS spectroscopic observations were reduced using the GEMINI package from IRAF v1.12. The four science frames were corrected for overscan, bias and flat-field using the routines GBIAS, GSFLAT and GSREDUCE. The cosmic rays were removed using LACOS_SPEC, developed by van Dokkum (2001). The detector gaps and remaining cosmic rays were removed combining with the GEMCOMBINE task the individual 2D spectra of each slit for each

Table 2.2 Gemini/GMOS spectroscopic instrumental and observational setup

Parameter	Exp. 1	Exp.2	Exp.3	Exp. 4
λ_c Å ^a	600	595	605	600
UT Date ^b	2013-11-27	2013-11-27	2013-11-27	2013-11-27
UT Time ^b	00:28:48.7	01:24:17.9	00:59:55.3	01:52:15.2
Airmass ^c	1.191	1.345	1.264	1.474
t_{exp} [s] ^d	1370	1370	1370	1370
Calib. Star ^e	LTT3218	LTT3218	LTT3218	LTT3218

^a Central wavelength of the dispersed light.

^b Universal date and time when the observation started.

^c Mean airmass during the observation.

^d Exposure time.

^e Spectrophotometric star for flux calibration.

central wavelength observed. The wavelength calibration in each combined 2D spectrum was done using the GSWAVELENGTH and GSTRANSFORM tasks. The rms in the wavelength calibration is 0.19 Å. Continuum and sky emission lines were removed from the spectra with the GSSKYSUB task. Finally, flux calibration was done by using the standard star LTT3218, which was reduced with a procedure similar to that used for the science data. The sensitivity function of the spectrum of LTT3218 and the flux calibration of the spectra of Arp 314 were obtained by using GSSTANDARD and GSCALIBRATE, respectively. This procedure allowed us to obtain the 1D spectra for the spectroscopic sources, which are analysed as discussed in Chapter 4.

Fabry-Perot data

Arp 314 was observed using the Fabry-Perot instrument Cinématique des GALaxiEs (CIGALE, Boulesteix et al. 1984 on the ESO 3.6m telescope at La Silla. These data were used to complement the Gemini/GMOS observations of Arp 314 described in the previous section. The Fabry-Perot observations of Arp 314 were taken in September 2000 and were already published in Torres-Flores et al. (2014a).

The FOV of CIGALE was centred on the group, scanning 32 steps with a total exposure time of 1.1 h. The scan gave sampling steps of 0.26 Å (11.81 km s⁻¹) with a spectral resolution of $R = 12682$ at H α and a free spectral range of of 378 km s⁻¹ (8.28 Å). CIGALE has a FOV of 207' \times 207' with a pixel scale of 0.405 arsec/pixel and an interference order $p = 793$ at H α .

The reduction of the Fabry-Perot data of Arp 314 is described in Torres-Flores et al.

(2014a), and we summarise it here. The software developed by Daigle et al. (2006) (see also Epinat et al. 2008) was used, which outputs the velocity field, the H α monochromatic flux, the continuum and the velocity dispersion map of each galaxy. An adaptive spatial binning was applied during data reduction in order to recover the information on regions with low SNR. The sky lines of OH were extracted by creating a data cube of the regions without galaxies, and the wavelength calibration was performed by scanning the narrow Ne $\lambda 6599$ Å line under the same conditions as the Arp 314 observations. The velocity map was corrected for instrumental broadening, deriving a mean instrumental correction over the whole field.

2.3 The Field Sample

In Chapter 3 we analyse galaxies in the two CLASH-VLT clusters MACS0416 and MACS 1206. In order to investigate the differences between galaxy properties in clusters and in the field, we built a sample of field galaxies drawn from the COSMOS/UltraVISTA catalogue published in Muzzin et al. (2013). This sample was also used to perform the statistical subtraction of interloper galaxies along the lines of sight to the clusters.

The COSMOS/UltraVISTA catalogue contains 262,615 sources and covers an area of 1.62 deg² of the Cosmic Evolution Survey (COSMOS, Scoville et al. 2007). The catalogue provides a point-spread function (PSF) matched photometry in 30 photometric bands covering the wavelength range of 0.15 - 24 μ m. Further, it contains photometric redshifts, stellar masses, and rest-frame U , V , and J photometry for all galaxies in the catalogue.

The sources in the catalogue have been selected from the UltraVISTA K_s survey (McCracken et al., 2012) with a limiting magnitude (90% completeness) $K_{s,tot} = 23.4$ mag. The UltraVISTA survey was carried out with the VISTA InfraRed CAMera (VIRCAM, Dalton et al. 2006) on the Visible and Infrared Survey Telescope for Astronomy (VISTA, Emerson et al. 2006) at the ESO/Paranal Observatory.

The COSMOS/UltraVISTA catalogue is available in the UltraVISTA web repository¹⁰. Details about the catalogue and derivation of photometric redshifts, stellar masses and rest-frame photometry are in Muzzin et al. (2013).

¹⁰<http://www.strw.leidenuniv.nl/galaxyevolution/ULTRAVISTA/Ultravista/K-selected.html>

3

Galaxy pre-processing in substructures around $z \sim 0.4$ galaxy clusters

The content of this chapter has been published in Monthly Notices of the Royal Astronomical Society (2018, vol. 479, page 2328) as “Galaxy pre-processing in substructures around $z \sim 0.4$ galaxy clusters” by Olave-Rojas D., Cerulo P., Demarco R., Jaffé Y. L., Mercurio A., Rosati P., Balestra I., Nonino M.

Abstract

We present a detailed analysis of galaxy colours in two galaxy clusters at $z \sim 0.4$, MACS J0416.1-2403 and MACS J1206.2-0847, drawn from the CLASH-VLT survey, to investigate the role of pre-processing in the quenching of star formation. We estimate the fractions of red and blue galaxies within the main cluster and the detected substructures and study the trends of the colour fractions as a function of the projected distance from the cluster and substructure centres. Our results show that the colours of cluster and substructure members have consistent spatial distributions. In particular, the colour fractions of galaxies inside substructures follow the same spatial trends observed in the main clusters. Additionally, we find that at large cluster-centric distances ($r \geq r_{200}$) the fraction of blue galaxies in both the main clusters and in the substructures is always lower than the average fraction of UVJ-selected star-forming galaxies in the field as measured in the COSMOS/UltraVista data set. We finally estimate environmental quenching efficiencies in the clusters and in the substructures and find that at large distances from the cluster centres, the quenching efficiency of substructures becomes comparable to the quenching efficiency of clusters. Our results suggest that pre-processing plays a significant role in

the formation and evolution of passive galaxies in clusters at low redshifts.

3.1 Introduction

It is well established that the evolution of galaxies is driven by a combination of internal and external physical mechanisms, which are linked to their stellar mass and to the environment in which they reside, respectively. In particular, the question: how do the properties of galaxies change as a function of environment? has motivated many works in the last decades (e.g. Dressler 1980, Couch et al. 1998; Kauffmann et al. 2004, Postman et al. 2005, Baldry et al. 2006, Bravo-Alfaro et al. 2009, Peng et al. 2010, Jaffé et al. 2016, Nantais et al. 2017, Cerulo et al. 2017).

Galaxy clusters are the most massive gravitationally bound cosmic structures and an ideal laboratory for the study of the environmental drivers of galaxy evolution (e.g. Poggianti et al. 2006, De Lucia et al. 2007, Demarco et al. 2010, Lemaux et al. 2012, Cerulo et al. 2014). The broad range of densities available in these systems, ranging from the dense core to the sparse outskirts, allows one to study the different physical mechanisms responsible for galaxy transformations (e.g. Boselli et al. 2016).

According to the Λ cold dark matter (Λ CDM) hierarchical paradigm, galaxy clusters are assembled through the continuous merging of smaller, group-like structures (Press & Schechter 1974, Fakhouri et al. 2010, Chiang et al. 2013). Theoretical models show that massive clusters in the Local Universe, with dark matter halo masses of the order of $10^{14.5} - 10^{15} M_{\odot}$ ¹, accreted $\sim 40\%$ of their galaxies from infalling groups with masses of the order of $10^{12} - 10^{13} M_{\odot}$ ¹ (McGee et al. 2009). For this reason, the study of the properties of galaxies at large cluster-centric radii ($2 \times r_{200} < r < 3 \times r_{200}$ ²; e.g. Li et al. 2009, Valentinuzzi et al. 2011, Lemaux et al. 2012, Dressler et al. 2013, Hou et al. 2014, Just et al. 2015, Haines et al. 2015), where these systems are still in the process of assembling, is of primary importance to understand the connection between the evolution of galaxies and the formation of their hosting large-scale structures (Fitchett 1988, Eke et al. 1996, Kravtsov & Borgani 2012).

In particular, some authors (see e.g. Vijayaraghavan & Ricker 2013, Hou et al. 2014; Just et al. 2015; Haines et al. 2015) find that the infall regions of galaxy clusters, at cluster-

¹We converted all the quantities reported in the literature to the cosmological parameters adopted in this study.

² r_{200} is the typical radius of a sphere with a mean density equal to 200 times the critical density

centric distances $2 - 3 \times r_{200}$, host large fractions of quiescent galaxies, with little or no ongoing star formation. This result cannot be reproduced by theoretical models in which star-formation, in infalling field galaxies, is quenched only when the galaxies pass within r_{200} of the galaxy cluster (Haines et al., 2015). In order to reproduce the observational results, it is necessary that the star formation in those galaxies be quenched in groups prior to the infall into the cluster. This scenario is known as *pre-processing* (Zabludoff & Mulchaey 1998, Fujita 2004, Wetzel et al. 2013).

Theoretical studies (e.g. Fujita 2004, McGee et al. 2009, Vijayaraghavan & Ricker 2013, Wetzel et al. 2013, Bahé et al. 2013, Bahé & McCarthy 2015) suggest that pre-processing is responsible for the elevated fraction of quiescent galaxies observed in the outer regions of galaxy clusters (e.g. Hou et al. 2014, Haines et al. 2015), in comparison with the field. In particular, Vijayaraghavan & Ricker (2013) performed cosmological N-body simulations and hydrodynamic simulations to study the merger between a galaxy group and a galaxy cluster since $z = 0.5$. The results of this analysis predict that pre-processing plays a fundamental role in quenching star formation because the gas of infalling group members is removed inside galaxy groups before these groups fall into a galaxy cluster. The gas is removed mainly through ram-pressure stripping (Gunn & Gott, 1972) and galaxy-galaxy interactions (e.g. Toomre & Toomre 1972, Barnes & Hernquist 1996). Moreover, these authors, following the cluster-group merger from $z = 0.5$ to $z = 0$, show that the infalling group does not get immediately virialised in the cluster environment: at $z = 0.2$ it can be seen that there are substructures within the main body of the cluster containing traces of the kinematics of the group. Similarly, Bahé et al. (2013, 2015) using a high-resolution cosmological hydrodynamic simulations found that $\sim 50\%$ of galaxies in subhaloes near to a massive galaxy cluster have been affected by pre-processing.

If the predictions of Vijayaraghavan & Ricker (2013) are correct then it should be possible to observe galaxy properties in cluster substructures that are not yet virialised within the main cluster halo. Hou et al. (2014) studied the impact of pre-processing through the observed quenched fraction in a sample of groups and cluster galaxies from the Sloan Digital Sky Survey Data Release 7 (SDSS-DR7; Abazajian et al. 2009) in the redshift range of $0.01 < z < 0.045$. They applied the Dressler-Shectman statistic (also known as the Dressler-Shectman test or DS-test, Dressler & Shectman 1988) to identify substructures which are kinematically distinct from the main galaxy cluster (Dressler et al., 2013).

In particular, Hou et al. (2014) found that at $2 \times r_{200} < r < 3 \times r_{200}$, the fraction of quiescent galaxies is higher in the substructure population than in the field population. These authors suggest that this enhancement is a result of the pre-processing of galaxies within substructures. In the same context, Cybulski et al. (2014) analysed the effects of pre-processing in a sample of 3505 galaxies in the Coma Supercluster. They studied the star formation (SF) activity of galaxies as a function of the type of environment (e.g. cluster, group, filament and void) to quantify the degree of impact of the environment on the SF activity in galaxies. They found that the pre-processing plays a fundamental role at low redshift, and that the evolution driven by the environment affects $\sim 50\%$ of the galaxies in groups.

Jaffé et al. (2011, 2016) found that galaxies within substructures are more likely to be deficient in atomic hydrogen (HI) and passive. In addition, Haines et al. (2015) found that the fraction of star-forming cluster galaxies rises steadily from the centre to the outskirts of galaxy clusters, but even at $3 \times r_{200}$ the values remain 20 - 30% below field values. To explain these results it is necessary that the star-formation and the fraction of HI in galaxies decline for the first time outside the central cluster regions, probably during the infall of galaxy groups.

In this Chapter we present a detailed analysis of the properties of galaxies in two clusters at $z \sim 0.4$, namely MACS J0416.1-2403 and MACS J1206.2-0847 (hereafter MAC0416 and MACS1206, respectively), drawn from Dark Matter Mass Distributions of Hubble Treasury Clusters and the Foundations of Λ CDM Structure Formation Models survey (CLASH-VLT, Rosati et al. 2014). These two systems represent two extreme cases of galaxy clusters, MACS0416 being an ongoing merger of two clusters (see e.g. Balestra et al. 2016) and the second system, MACS1206, being a relaxed cluster (Biviano et al., 2013). This Chapter has been published as a paper, which is the first in a series addressing the study of the properties of galaxies in the substructures of clusters at intermediate redshifts ($0.2 < z < 0.6$) in the CLASH-VLT survey. We present here the method that will be used in the analysis of CLASH-VLT and apply it to two extreme examples of galaxy clusters.

The Chapter is organised as follows. In Section 3.2 we describe the data sets. In Section 3.3 we present the measurements and data analysis, while in Section 3.4 we present the results which we discuss in Section 3.5. Section 3.6 summarises our main conclusions. Throughout the Chapter we adopt a Λ CDM cosmology with $\Omega_\Lambda = 0.7$, $\Omega_m = 0.3$,

and $h = H_0/100 \text{ km s}^{-1} \text{ Mpc}^{-1} = 0.7$ (Spergel et al., 2003). All magnitudes in this Chapter are in the AB-system (Oke, 1974) unless otherwise stated. In this Chapter we consider r_{200} as the physical radius, measured in Mpc, inside which the density is 200 times the critical density of the Universe at the redshift of each cluster.

3.2 Data

MACS0416 and MACS1206 were drawn from the CLASH-VLT survey. CLASH-VLT is a spectroscopic follow-up of the Cluster Lensing and Supernova survey with Hubble (CLASH, Postman et al. 2012), which targeted 25 massive clusters ($M_{\text{halo}} > 10^{14.5} M_{\odot}$) at redshifts $0.2 < z < 0.9$ with the Hubble Space Telescope and other space- and ground-based facilities to study cosmology and galaxy evolution. CLASH-VLT targeted the 13 CLASH clusters at redshifts $0.2 < z < 0.6$ that are observable from the southern hemisphere. In this Chapter we use public spectrophotometric data compiled by the CLASH collaboration³.

3.2.1 Photometric Catalogues

MACS0416 and MACS1206 were observed with the SuprimeCam (Miyazaki et al., 2002) at the prime focus of the 8.3m Subaru Telescope, in the B , R_c and z' , and B , V , R_c , I_c and z' bands, respectively (Umetsu et al. 2012, 2014). Photometric data from Subaru have an angular coverage of $34' \times 27'$ around the centre of each galaxy cluster. The above observations are available in the Subaru archive, Subaru-Mitaka Okayama-Kiso Archive System (SMOKA⁴; Baba et al. 2002). In addition, MACS0416 was observed with the Wide-Field Imager (WFI; Baade et al. 1999) on the ESO/MPG 2.2m telescope at the La Silla Observatory in Chile, in the B , V , R and I photometric bands, covering an area of $34' \times 33'$ around the centre of the cluster (Gruen et al., 2014). Subaru images were reduced by the CLASH team following the techniques described in Nonino et al. (2009). WFI images were reduced by Gruen et al. (2014) using Astro-WISE (Valentijn et al., 2007). A full description of the reduction of Subaru and WFI images is given in Umetsu et al. (2012) and Gruen et al. (2013, 2014), respectively.

³<https://archive.stsci.edu/prepds/clash/>

⁴<http://smoka.nao.ac.jp>

In this Chapter we use the photometric catalogues generated by the CLASH-VLT team. For MACS0416 we complement those catalogues with the public catalogue published by Gruen et al. (2014) and available on the author's web page⁵.

Aperture magnitudes in Subaru and WFI catalogues were obtained using the software SExtractor (Bertin & Arnouts, 1996) in conjunction with PSFEx (Bertin, 2011). Aperture magnitudes were measured within fixed circular apertures. For MACS0416 aperture diameters of 3'' and 2'' are used for Subaru and WFI, respectively, while for MACS1206 is used a diameter of 5''. Aperture magnitudes were corrected for zero-point shifts and Galactic extinction by comparing the galaxy observed colours to the stellar library of Pickles (1998) and using the Galactic extinctions of Schlafly & Finkbeiner (2011) and Schlegel et al. (1998) for Subaru and WFI, respectively. We select galaxies with magnitudes $R_c < 26.0$, which corresponds to the 3σ limit for an aperture 2'' in diameter (Umetsu et al., 2014). A description of the photometric catalogues from Subaru and WFI can be found in Mercurio et al. (2014, 2016) and Gruen et al. (2013; 2014), respectively.

3.2.2 Spectroscopic Catalogues

We use the public spectroscopic redshift catalogues⁶ (see Biviano et al. 2013; Balestra et al. 2016; Caminha et al. 2017) from CLASH-VLT (Rosati et al., 2014).

The VIMOS spectroscopic observations were made in four separate pointings centred on the core of each cluster. MACS0416 and MACS1206 were observed using a total of 21 (15 Low-Resolution Blue and 6 Medium Resolution) masks and 12 (8 Low-Resolution Blue and 4 Medium Resolution) masks, respectively. Low-Resolution Blue and Medium-Resolution masks have a spectral coverage of 3760 - 6700Å and 4800 - 10000Å with a resolving power of $R = 180$ and $R = 850$, respectively. A full description about how the spectroscopic observations of MACS0416 and MACS1206 were made can be found in Balestra et al. (2016) and Biviano et al. (2013), respectively.

The VIMOS spectroscopic observations were reduced, by the CLASH-VLT team, using the VIMOS Interactive Pipeline Graphical Interface (VIPGI, Scodreggio et al. 2005). Redshifts were determined using the software Easy Redshift (EZ, Garilli et al. 2010). EZ determines the redshift by making a cross-correlation between the observed spectrum and template spectra. In cases in which the redshift solution was dubious, the redshift was

⁵<http://www.usm.uni-muenchen.de/~dgruen/download.html>

⁶<https://sites.google.com/site/vltclashpublic/>

determined by visual inspection (Balestra et al., 2016). Uncertainties on the redshifts are in the range of $75 - 150 \text{ km s}^{-1}$ (Annunziatella et al. 2014; Balestra et al. 2016).

Spectroscopic catalogues, of MACS0416 and MACS1206, have a magnitude limit of $R_c = 24.0 \text{ mag}$. A detailed description of the CLASH-VLT redshift catalogues can be found in Biviano et al. (2013), Mercurio et al. (2014), Balestra et al. (2016), and Caminha et al. (2017).

The CLASH-VLT data release provides a spectroscopic sample of 4594 and 2736 galaxies for MACS0416 and MACS1206, respectively (Biviano et al. 2013, Balestra et al. 2016, Caminha et al. 2017), over an area of $26' \times 23'$ around the centre of each galaxy cluster.

3.3 Measurement and Data Analysis

3.3.1 Spectroscopic Completeness

Due to the strategy used on the selection of spectroscopic targets in the CLASH-VLT survey (see Biviano et al. 2013, Annunziatella et al. 2014, Balestra et al. 2016, Caminha et al. 2017 for details on the strategy of spectroscopic observations) the spectroscopic completeness of the CLASH-VLT sample decreases with the distance from the cluster centre, reducing the statistics in the outskirts of galaxy clusters. This may affect our ability to detect substructures (Balestra et al., 2016).

We estimated the sample spectroscopic completeness following the APPENDIX A in Poggianti et al. (2006). More precisely, we measured the ratio between the number of galaxies in the spectroscopic and photometric catalogues (N_{spec} and N_{phot} , respectively) in different bins of apparent magnitude or projected distance from the cluster centre to estimate the spectroscopic completeness, $C = N_{spec}/N_{phot}$, which is used to correct our measurements. We stress here that N_{spec} corresponds to the number of galaxies with spectroscopic redshift (see §3.2.2) and N_{phot} corresponds to the number of all galaxies in the photometric catalogue.

In Figure 3.1, we show the spectroscopic completeness, for MACS0416 and MACS1206, as a function of galaxy apparent magnitude in the R_c -band and projected distance from the cluster centre normalised by r_{200} (r_{200} is 1.82 Mpc and 2.33 Mpc for MACS0416 and MACS1206, respectively; see Umetsu et al. 2014, Merten et al. 2015). The central coor-

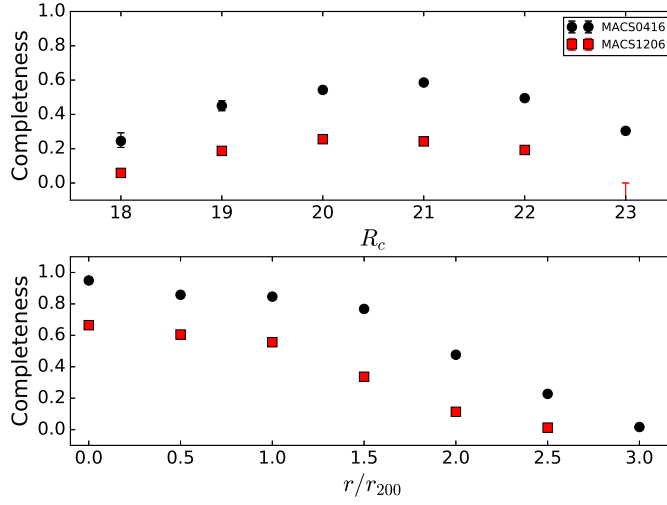


Figure 3.1 Spectroscopic Completeness. The top panel shows the completeness as a function of apparent magnitude in the R_c -band. The bottom panel shows the completeness as a function of the projected distance from the centre of the clusters normalised by r_{200} . Black points and red squares represent the spectroscopic completeness for MACS0416 and MACS1206, respectively. We note a lack of completeness in the brightest magnitude bins. This effect could be a consequence of the selection criteria for spectroscopic targets, which were selected mainly in a colour-colour space. Source: Olave-Rojas et al. (2018)

coordinates of each galaxy cluster were taken from Balestra et al. (2016) and Annunziatella et al. (2014) for MACS0416 and MACS1206, respectively.

3.3.2 Photometric Redshifts

With the spectroscopic incompleteness increasing towards the cluster outskirts, we complemented our spectroscopic selection of cluster members and substructures with the photometric redshifts available for the two clusters. For MACS0416 we used the catalogue of Gruen et al. (2014), released as part of the Hubble Frontier Fields (HFF⁷, Koekemoer et al. 2014, Lotz et al. 2017), while for MACS1206 we used an internal catalogue produced by the CLASH-VLT collaboration.

Photometric redshifts (hereafter z_{phot}) for MACS1206 were estimated using aperture magnitudes (see §3.2.1) through a Neural Network method using the Multi Layer Perceptron with Quasi Newton Algorithm (MLPQNA; Brescia et al. 2013), which is an empirical method that achieves a high accuracy and reduces the number of catastrophic objects

⁷<http://www.stsci.edu/hst/campaigns/frontier-fields/>

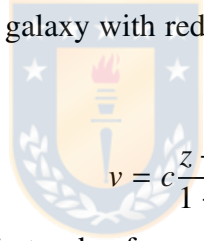
(Brescia et al., 2013). A full description of the derivation of z_{phot} for MACS1206 is given in Biviano et al. (2013) and Mercurio et al. (2014). Photometric redshifts for MACS0416 were estimated using the photometric template-fitting developed by Bender et al. (2001). See Brimiouille et al. (2013) and Gruen et al. (2013; 2014), for further details on z_{phot} estimates for MACS0416.

3.4 Results

3.4.1 Cluster membership, velocity dispersion and stellar mass

It is crucial to determine the cluster membership to find and characterise substructures. In practice, cluster members are defined as those galaxies with a peculiar velocity (see equation 3.1) lower than the escape velocity (v_{esc} , see equation 3.2, Diaferio 1999), of a galaxy cluster.

The peculiar velocity of a galaxy with redshift z in the rest frame of a galaxy cluster with redshift z_{cl} is given by:



$$v = c \frac{z - z_{cl}}{1 + z_{cl}} \quad (3.1)$$

This equation is valid, to first order, for $v \ll c$ (Harrison, 1974). The escape velocity, estimated for a cluster, using M_{200} and r_{200} , is computed as (Diaferio, 1999):

$$v_{esc} \simeq 927 \left(\frac{M_{200}}{10^{14} h^{-1} M_{\odot}} \right)^{1/2} \left(\frac{r_{200}}{h^{-1} Mpc} \right)^{-1/2} \text{ km s}^{-1} \quad (3.2)$$

The estimates of M_{200} using strong and weak gravitational lensing span the ranges $1.299 - 1.240 \times 10^{15} M_{\odot}$ (see Umetsu et al. 2014, Umetsu et al. 2016) and $1.186 - 1.590 \times 10^{15} M_{\odot}$ (see Biviano et al. 2013, Umetsu et al. 2014, Merten et al. 2015, Barreira et al. 2015) for MACS0416 and MACS1206, respectively. The estimates of M_{200} have a typical uncertainty $\leq 5\%$ depending of the model fitted (typically Einasto 1965 and Navarro et al. 1995) to the mass profile derived from gravitational lensing. Hereafter the values of M_{200} assumed are $1.27 \times 10^{15} M_{\odot}$ and $1.39 \times 10^{15} M_{\odot}$ for MACS0416 and MACS1206, respectively. These values correspond to the mean value of M_{200} for each cluster. Instead the mean value of r_{200} to derive v_{esc} was estimated using the equation (7) presented by Finn et al. (2005).

Table 3.1 Main properties of the clusters MACS0416 and MACS1206

Cluster	R.A. ^a (J2000.)	Dec. ^a	v_{esc} Km s ⁻¹	z	σ_{cl} Km s ⁻¹
MACS0416	04:16:09.14	-24:04:03.1	2375 ± 10	0.397	1044 ± 23
MACS1206	12:06:12.15	-08:48:03.4	2485 ± 68	0.440	1011 ± 25

^a The centre positions were taken from Balestra et al. (2016) and Annunziata et al. (2014) for MACS0416 and MACS1206, respectively.

Spectroscopic members were determined similarly to Cerulo et al. (2016), first we removed galaxies from the redshift catalogue with a peculiar velocity higher than the v_{esc} of the galaxy cluster. Then we estimated the velocity dispersion for the clean sample of cluster members, following the biweight estimator described in Beers et al. (1990), and finally we removed the field interlopers through a 3σ clipping algorithm (see Yahil & Vidal 1977). Following the above criterion, we found ~ 890 and ~ 640 spectroscopic members for MACS0416 and MACS1206, respectively. We used the biweight estimator to estimate the mean cluster redshift and velocity dispersion of the whole system. We estimated mean redshifts of $z \sim 0.397$ and $z \sim 0.440$, and velocity dispersions (σ_{cl}) of 1044 ± 23 km s⁻¹ and 1011 ± 25 km s⁻¹ for MACS0416 and MACS1206, respectively. These values are consistent within 1σ and 1.4σ , respectively, with results reported in the literature (Girardi et al. 2015, Balestra et al. 2016). The errors in σ_{cl} were estimated using a bootstrap technique. The central positions in Right Ascension (R.A.) and Declination (Dec.) and the kinematic properties of MACS0416 and MACS1206 are summarised in Table 3.1

3.4.2 Detection of Substructures

Once we have selected the spectroscopic members for each galaxy cluster, we verified whether the clusters contain substructures or not. For this, we used the Dressler-Shectman's statistic (Dressler & Shectman, 1988), which allows us to make a test (also known as the Dressler-Shectman test or DS-test) to verify the existence of regions kinematically distinct from the main galaxy cluster (Dressler et al., 2013).

In short, the DS-test compares the local velocity and velocity dispersion for each galaxy (\bar{v}_{local}^i and σ_{local}^i) with the cluster global values (\bar{v}_{cl} and σ_{cl} ; Jaffé et al. 2013). Local parameters are estimated in a subset of galaxies containing the galaxy i and its

Table 3.2 Results from the DS-Test on MACS0416 and MACS1206

Cluster	N_{mem}	Δ_{obs}/N_{mem}	P
MACS0416	890	1.64	<0.001
MACS1206	641	1.22	<0.001

nearest neighbours (N_{nn}). We used $N_{nn} = 10$ in equation 3.3 to apply the DS-Test in our clusters. The δ_i statistic used in the DS-Test is expressed as:

$$\delta_i^2 = \left(\frac{N_{nn} + 1}{\sigma_{cl}^2} \right) [(\bar{v}_{local}^i - \bar{v}_{cl})^2 + (\sigma_{local}^i - \sigma_{cl})^2]. \quad (3.3)$$

This value quantifies the galaxy's kinematic deviation with respect to the mean cluster values of velocity and velocity dispersion (e.g. Dressler et al. 2013, Jaffé et al. 2013, Hou et al. 2014). The larger the δ_i value, the greater the probability that the galaxy belongs to a substructure.

Dressler & Shectman (1988) also define the cumulative δ as $\Delta = \sum_i \delta_i$. A value $\Delta/N_{mem} > 1$, where N_{mem} is the number of cluster members, would be an indication that the cluster hosts substructures. However, it should be stressed that a high Δ value may be the result of random spatial fluctuations in the redshift distribution of cluster members. In order to assess this effect, we generated 1000 simulated spectroscopic samples by shuffling the velocities and positions of each galaxy in the clusters. For each of these bootstrap samples we estimated Δ and defined the P-value $P = \sum(\Delta_{shuffle} > \Delta_{obs}/N_{shuffle})$ where $\Delta_{shuffle}$ is the value of Δ obtained for each simulated sample and $N_{shuffle}$ is the number of bootstrap iterations. Values of $P < 0.01$ provide a robust constraint on the presence of substructures in the clusters. We find that MACS0416 and MACS1206 both have $\Delta/N_{mem} > 1$ and $P < 0.001$ (see Table 3.2), giving statistical support to the existence of real substructures.

After applying the DS-test we proceeded to identify and characterise the substructures. For this purpose we need to select only galaxies with a $\delta_i > \delta_{lim}$, which corresponds to galaxies with a higher probability to be inside a substructure. To determine δ_{lim} we estimated the width σ_δ of the δ_i distribution in each cluster. Following Girardi et al. (1996), δ_{lim} was defined as $\delta_{lim} = 3\sigma_\delta$ and galaxies were considered members of substructures if $\delta_i \geq \delta_{lim}$.

However, the selection $\delta_i \geq \delta_{lim}$ may include galaxies which do not necessarily belong

to a substructure due to their peculiar velocities and positions within the cluster (see e.g. discussions in Jaffé et al. 2013). Thus we added to the selection in δ_i two consecutive selections in peculiar velocity and projected position. The two selections were performed by using python scripts that combined new and pre-existing modules. The selection in velocity was performed, following e.g. Girardi et al. (2005) and Demarco et al. (2007) by using the Gaussian Mixture Model (GMM; Muratov & Gnedin 2010) algorithm. This algorithm assumes that a sample is described by the sum of two or more Gaussian functions. GMM estimates the probability that an object belongs to each identified Gaussian component through an iterative algorithm (expectation-maximisation, EM, Dempster et al. 1977, Press et al. 2007). The objects are assigned to the groups for which the likelihood of membership is higher.

For the selection of substructures in projected space, we tested two clustering algorithms available in python, namely K-Means (Lloyd, 2006) and the Density-Based Spatial Clustering of Applications with Noise (DBSCAN, Ester et al. 1996), finally preferring the second one. To identify groups using DBSCAN we must define a minimum number of neighbouring objects separated by a specific distance. When using this algorithm not all objects in the sample are assigned to a group (Ester et al., 1996) and we can remove the galaxies that are not spatially grouped with others.

In practice, we defined a substructure as a collection of at least three neighbouring galaxies with a spatial separation of ~ 140 kpc, which is a typical maximum spacing between galaxies within compact groups of galaxies (Sohn et al., 2015). Figure 3.2 shows the substructures identified for each cluster. Table 3.3 lists the central position, central redshift, number of members, velocity dispersion (σ_{sb}) and r_{200} for each identified substructure. The central position of a substructure was defined as the centroid of the spatial distribution of galaxies in the substructure. r_{200} was estimated from σ_{sb} using Equation 8 of Finn et al. (2005) under the assumption that each substructure is virialised. Uncertainties on the numbers of substructure members were estimated as the 90% Poissonian confidence intervals adopting the approximations of Ebeling (2003). We note that MACS0416_3, MACS0416_15, MACS1206_2 and MACS1206_7 have a narrow velocity range and we cannot estimate σ_{sb} and r_{200} in these substructures. We found 15 substructures in MACS0416 and 11 in MACS1206 (see Figure 3.2 and Table 3.3).

We note that the substructure MACS0416_5 corresponds to the “*Sext*” substructure previously identified by Balestra et al. (2016) in MACS0416. For this substructure we

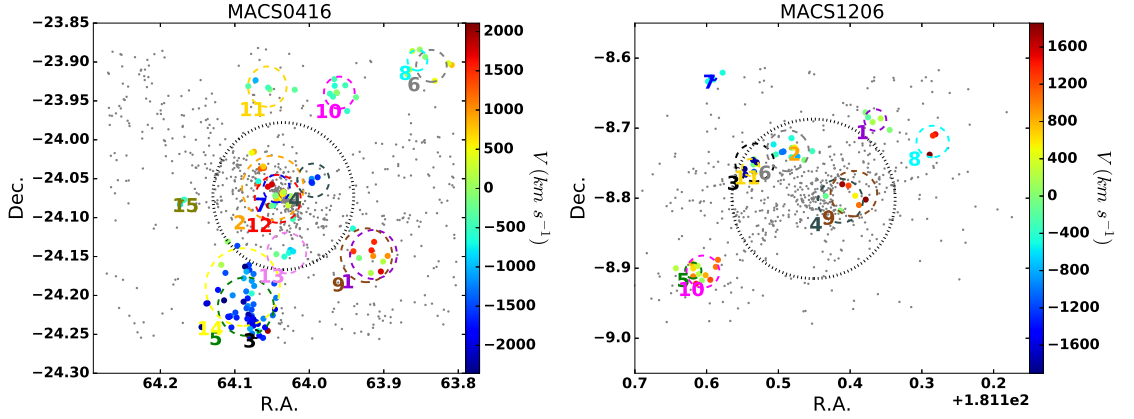


Figure 3.2 Spatial and radial velocity distribution of cluster members for MACS0416 (left) and MACS1206 (right). The black dashed circle indicates the r_{200} radius of the cluster. Grey points represent all spectroscopic members. Dashed circles of different colours indicate the r_{200} of each identified substructure. Galaxies inside substructures are plotted with points whose colours indicate the peculiar velocity of the galaxies in the rest frame of the cluster. Source: Olave-Rojas et al. (2018).

estimate a number of members of 47 ± 10 and a velocity dispersion of $354 \pm 25 \text{ km s}^{-1}$. These values are consistent within 1σ with results reported in the literature (Balestra et al., 2016).

3.4.3 Colour-Magnitude Diagram

To analyse the relationship between galaxy colour and environment we study the colour-magnitude properties of galaxies in substructures and in the clusters. For this purpose, using the photometric catalogues from Subaru (see §3.2.1), we performed a match between the spectroscopic members catalogue (see §3.4.1) and the photometric catalogue with the objective of obtaining $(B - R_c)$ colours for the spectroscopic members. The match was performed using the positions in R.A. and Dec. listed for each source in both catalogues. We set an aperture of $1''$ as the maximum separation between the matched galaxies. The corresponding $(B - R_c)$ vs R_c colour-magnitude diagram (CMD) is shown in Figure 3.3.

We used GMM to fit two Gaussians over the colour distribution to separate galaxy populations (see Figure 3.4) in different regions of the CMD. The green valley or transition zone (Cortese & Hughes, 2009) is defined as the space between the blue and red components determined by GMM (e.g Cortese 2012, Schawinski et al. 2014). In practice, to separate galaxies according to their colours we fit a Gaussian to the red and blue colour

Table 3.3 Substructures identified in MACS0416 and MACS1206 and their principal features

Cluster	Name of Substructure	R.A. ^a	Dec. ^a	z^a	No. of members ^b		σ_{sb}	r_{200}
(1)	(2)	(J2000.)		(5)	(6)		Km s ⁻¹	Mpc
(1)	(2)	(3)	(4)	(5)	(6)		(7)	(8)
MACS0416	MACS0416_1	04 : 15 : 39.3	-24 : 08 : 50.6	0.404	6±4	(34±8)	306±64	0.612
	MACS0416_2	04 : 16 : 11.8	-24 : 03 : 42.5	0.403	16±6	(78±12)	402±59	0.804
	MACS0416_3	04 : 16 : 17.2	-24 : 14 : 58.9	0.406	3±3	(3±3)	-	-
	MACS0416_4	04 : 15 : 58.7	-24 : 03 : 07.4	0.390	4±3	(10±5)	203±58	0.409
	MACS0416_5	04 : 16 : 20.4	-24 : 12 : 51.2	0.389	47±10	(89±13)	354±25	0.714
	MACS0416_6	04 : 15 : 20.7	-23 : 54 : 18.0	0.399	5±3	(7±4)	198±90	0.396
	MACS0416_7	04 : 16 : 10.5	-24 : 03 : 45.5	0.400	9±4	(25±7)	172±55	0.344
	MACS0416_8	04 : 15 : 25.2	-23 : 53 : 51.8	0.397	3±3	(6±4)	128±0	0.257
	MACS0416_9	04 : 15 : 41.6	-24 : 08 : 54.1	0.397	4±3	(40±9)	332±109	0.666
	MACS0416_10	04 : 15 : 50.3	-23 : 56 : 22.0	0.395	9±4	(21±7)	197±68	0.396
	MACS0416_11	04 : 16 : 13.5	-23 : 55 : 54.0	0.396	5±3	(21±7)	248±85	0.498
	MACS0416_12	04 : 16 : 10.2	-24 : 04 : 32.9	0.396	8±4	(45±9)	295±36	0.591
	MACS0416_13	04 : 16 : 07.3	-24 : 08 : 43.5	0.394	5±3	(17±6)	250±57	0.503
	MACS0416_14	04 : 16 : 21.4	-24 : 11 : 21.3	0.394	7±4	(77±12)	476±126	0.956
	MACS0416_15	04 : 16 : 40.9	-24 : 04 : 45.5	0.395	3±3	(3±3)	-	-
MACS1206	MACS1206_1	12 : 05 : 51.6	-08 : 41 : 18.4	0.440	5±3	(7±4)	160±17	0.313
	MACS1206_2	12 : 06 : 17.8	-08 : 44 : 01.7	0.440	3±3	(3±3)	-	-
	MACS1206_3	12 : 06 : 31.9	-08 : 44 : 56.6	0.440	3±3	(6±4)	283±0	0.553
	MACS1206_4	12 : 06 : 03.2	-08 : 48 : 13.5	0.440	3±3	(20±6)	328±0	0.642
	MACS1206_5	12 : 06 : 52.5	-08 : 54 : 12.3	0.441	5±3	(9±4)	119±41	0.232
	MACS1206_6	12 : 06 : 20.8	-08 : 43 : 56.4	0.437	9±4	(10±5)	304±40	0.597
	MACS1206_7	12 : 06 : 45.6	-08 : 37 : 41.4	0.438	4±3	(4±3)	-	-
	MACS1206_8	12 : 05 : 32.4	-08 : 43 : 08.8	0.447	3±3	(7±4)	239±0	0.465
	MACS1206_9	12 : 05 : 58.8	-08 : 47 : 36.6	0.447	4±3	(16±6)	344±53	0.669
	MACS1206_10	12 : 06 : 49.2	-08 : 54 : 17.6	0.445	8±4	(23±7)	242±38	0.472
	MACS1206_11	12 : 06 : 33.2	-08 : 45 : 22.5	0.431	5±3	(5±3)	125±111	0.245

^a Central values for each identified substructure.

^b Number of substructure members estimated from the spectroscopic sample. In parenthesis we show the number of substructure members estimated from the spectroscopic+photometric sample as described in §3.4.4.

components, separately. Then we estimated the mean (μ) and dispersion (σ) of each gaussian. We considered as blue those galaxies that have a colour $(B - R_c) \leq \mu_{blue} + 1\sigma_{blue}$, as red those galaxies that have a colour $(B - R_c) \geq \mu_{red} - 1\sigma_{red}$, and as green those galaxies in the $\mu_{blue} + 1\sigma_{blue} < (B - R_c) < \mu_{red} - 1\sigma_{red}$ colour range.

3.4.4 Photometric Members

As described in §3.3.1 in Figure 3.1 we can see that the spectroscopic completeness decreases with the projected distance from the cluster centre, reducing the statistics in the outer regions of the clusters ($r > r_{200}$) where most substructures are expected (Aguerri et al. 2007, Jaffé et al. 2016, Vijayaraghavan & Ricker 2013). This affects the characterisation of the properties of infalling galaxies and groups (Biviano et al. 2013; Balestra et al. 2016). Thus, in addition to our spectroscopic sample, we built a sample of cluster

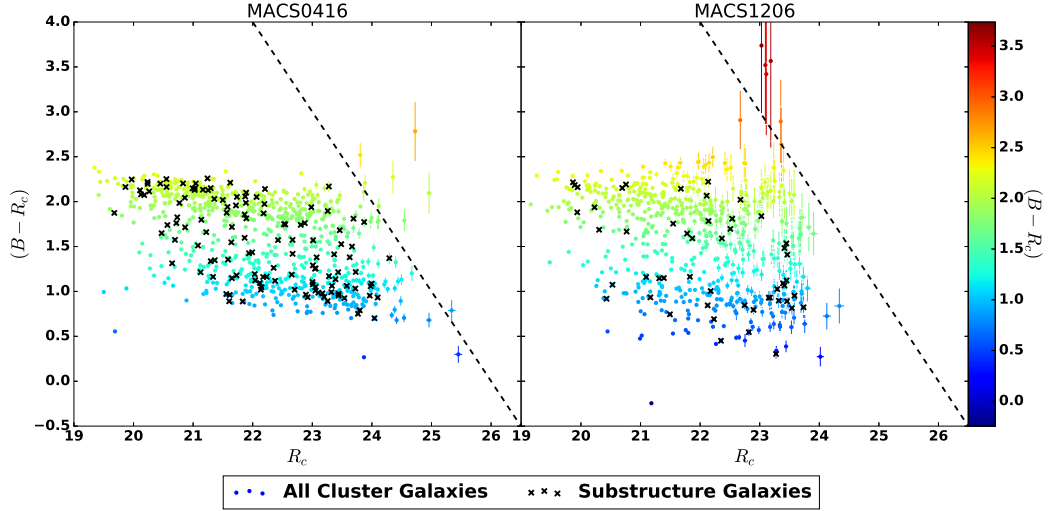


Figure 3.3 Colour-magnitude diagrams of spectroscopically confirmed cluster members. The colours are measured in the B and R_c Subaru bands. Cluster member galaxies are plotted with points whose colours indicate the $(B - R_c)$ colour and galaxies in substructures are plotted with black crosses. The diagonal dashed lines represent the 3σ completeness limit in the B and R_c Subaru images. This figure illustrates that galaxies in substructures follow the same colour-magnitude relation as the parent galaxy cluster. Left panel: MACS0416. Right panel: MACS1206. Source: Olave-Rojas et al. (2018)

members selected according to their photometric redshifts (see §3.3.2).

Cluster Membership

Photometric members were defined as those in the range $(z_{cl} - \delta_z) \lesssim z_{phot} \lesssim (z_{cl} + \delta_z)$. To determine δ_z for each cluster we used the available spectroscopic redshifts to calibrate the z_{phot} . First, we made a match between the catalogue with spectroscopic members and the catalogue of objects with z_{phot} to estimate the redshift discrepancy $\Delta_z = |z_{spec} - z_{phot}| / (1 + z_{spec})$. The match between photometric and spectroscopic catalogues were made using the position in R.A. and Dec. listed for each source in both catalogues. We set an aperture of $1''$ as the maximum separation between the matched galaxies. Then we estimated the standard deviation, σ_{Δ_z} of the redshift discrepancy distribution to exclude catastrophic identifications, defined here as those with $\Delta_z \geq 3 \times \sigma_{\Delta_z}$. Finally, we defined δ_z as the standard deviation of the $|z_{spec} - z_{phot}|$ distribution in the final clean sample.

Photometric cluster members were defined as those galaxies in the range $0.359 < z_{phot} < 0.433$ and $0.395 < z_{phot} < 0.483$, for MACS0416 and MACS1206, respectively.

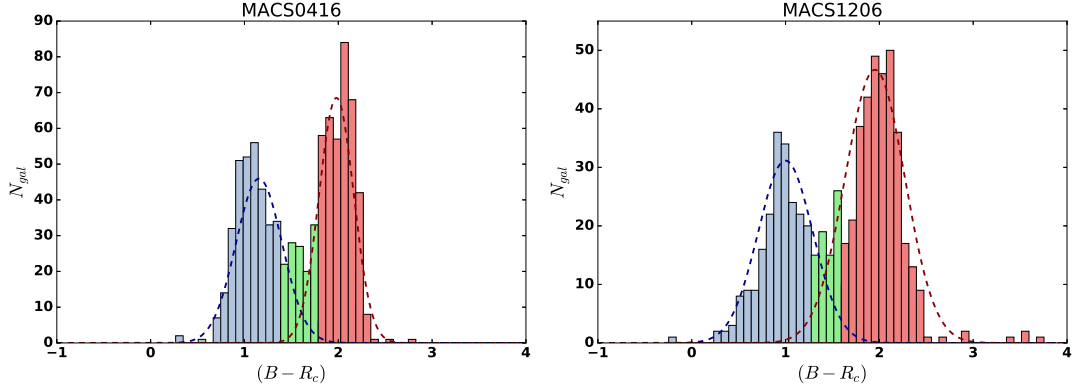


Figure 3.4 Colour histogram that shows the bimodal distribution in $(B - R_c)$ colour. Blue and red lines represent the Gaussian fitting of blue and red components determined by GMM. The colour bimodal distribution of galaxies allows us to separate galaxies in blue, red and green according to their colours. Blue galaxies have a colour $(B - R_c) \leq \mu_{blue} + 1\sigma_{blue}$, red galaxies have a colour $(B - R_c) \geq \mu_{red} - 1\sigma_{red}$, and green galaxies are in the $\mu_{blue} + 1\sigma_{blue} < (B - R_c) < \mu_{red} - 1\sigma_{red}$ colour range. Left panel: MACS0416. Right panel: MACS1206. Source: Olave-Rojas et al. (2018)

Additionally, we used the spectroscopic members to clean the sample of photometrically-selected members from false positives. False positives were defined as those galaxies that were selected as photometric members but whose spectroscopic redshift poses them outside the clusters. In practice, we removed 541 and 275 false positives from the photometrically-selected member catalogues of MACS0416 and MACS1206, respectively. We combined the samples of spectroscopic and photometric members and obtained a sample of 3523 and 2070 *spectrophotometric* members, for MACS0416 and MACS1206, respectively.

Substructure Membership

Substructure member candidates were defined as those galaxies within r_{200} of each substructure and in the range $(z_{sub} - \delta_z) \lesssim z_{phot} \lesssim (z_{sub} + \delta_z)$. The value of δ_z is defined for each substructure in the same way as described in §3.4.4. For substructures in which we cannot estimate r_{200} we have not added photometric members.

We combined the spectroscopic and photometric sample for substructure, showing the corresponding number of members for each substructure within parenthesis in Column (6) of Table 3.3. Uncertainties in member counts were estimated in the same way as described in §3.4.2. We note that in some cases (e.g. in MACS1206.4 and MACS1206.9) there are

substructures that are spatially overlapped and some photometric members are assigned to both substructures. This could be due to the fact that these substructures may be in a merger. This fact is taken into account in §3.4.6 as a source of error due to background contamination.

3.4.5 Stellar Masses

With only 3 photometric bands available for MACS0416, it is not possible to obtain reliable stellar masses through SED fitting. For this reason we estimated stellar masses in the spectroscopic and spectrophotometric samples with the calibrations of Bell et al. (2003) for the present-day stellar mass-to-light (M_{\star}/L) ratios. These authors used a sample of 12,085 galaxies from the Two Micron All Sky Survey (2MASS, Skrutskie et al. 2006) and the Sloan Digital Sky Survey (SDSS, York et al. 2000) to study the stellar mass function in the local Universe. To obtain the stellar masses Bell et al. (2003) used the correlation found by Bell & de Jong (2001) (see equation 3.4) between M_{\star}/L and galaxy colours in the rest-frame. Bell et al. (2003) re-fitted this correlation to find the empirical coefficients (a_{λ} and b_{λ}) that allows the conversion of the SDSS colours into M_{\star}/L . The scatter found by Bell et al. (2003) in the correlation between optical colours and M_{\star}/L is ~ 0.1 dex.

$$\log_{10}(M_{\star}/L) = a_{\lambda} + (b_{\lambda} \times Colour) \quad (3.4)$$

The relation of Bell et al. (2003) uses as input the rest-frame photometry. Therefore, to obtain the stellar masses of the galaxies in our sample using Equation 3.4 we must convert our observer-frame photometry to rest-frame photometry. For this, we follow the approach presented in the APPENDIX B of Mei et al. (2009) to convert the $(B - R)$ observer-frame colour to rest-frame SDSS colour and the B observer-frame magnitude to rest-frame SDSS magnitude. Mei et al. (2009) found that there is a correlation between observer-frame photometry and rest frame photometry given by

$$C_{rf} = A + B \times C_{obs} \quad (3.5)$$

$$M_{rf} - m_{obs} = \alpha + \beta \times C_{obs} \quad (3.6)$$

Zero-points (A and α) and slopes (B and β) in equations 3.5 and 3.6 were estimated using a set of synthetic stellar population models from Bruzual & Charlot (2003; BC03) with ten different metallicities from 0.4 to $2.5Z_{\odot}$, two laws of star formation rate (instantaneous burst and exponentially decaying with e-folding time $\tau = 1$ Gyr) and Salpeter (1955) IMF. The BC03 spectral library spans the range in formation redshift $2.0 < z_f < 5.0$. The models were generated with EzGal⁸ (Mancone & Gonzalez, 2012) and for each one we extracted the observed and rest-frame colours and magnitudes at the redshift of each cluster and fitted the linear relation. Zero-points and slopes were derived following the approach presented by Dang et al. (2006). In summary we fit straight lines to all the possible couples of points in the colour-colour and magnitude-colour planes and obtain the distributions of slopes and intercepts. Zero-points and slopes are defined as the median of each distribution, while their uncertainties are taken as the 1σ width of the distributions.

In practice, stellar masses (M_{\star}) of the galaxies in our sample were obtained converting the $(B - R)$ observer-frame colour to $(u' - g')$ rest-frame colour and the B observer-frame magnitude to rest-frame absolute M_g magnitude. The values of a_g and b_g were taken from Table A7 presented by Bell et al. (2003). Stellar mass uncertainties were estimated using a technique based on a Monte Carlo approach. The observer-frame colour, observer-frame magnitudes, zero-points (A and α), slopes (B and β), rest-frame colours and rest-frame magnitudes were perturbed by a random value, ϵ , in the range $-\Delta < \epsilon < +\Delta$, where Δ corresponds to the error in each variable. We generate 20 simulated objects for each real object. Finally, we estimated the uncertainties on stellar mass evaluating the 1σ asymmetric width of the simulated stellar mass distribution. The stellar masses obtained are in the range $8 \leq \log(M_{\star}/M_{\odot}) \leq 11.5$ for both MACS0416 and MACS1206. The uncertainties in the stellar masses are in the range $0.1 - 0.2$ dex.

3.4.6 Colour Fractions

Galaxy colours are related to internal properties. For example, red galaxies are more likely passive or quiescent, without star-formation. Blue galaxies, on the contrary, are more likely star forming. For this reason, we are interested in examining the relationship between galaxy colours and the local environment. We estimated the fraction of blue, green and red galaxies as a function of projected distance from the cluster centre or sub-

⁸<http://www.baryons.org/ezgal/>

structure centre, as a function of R_c magnitude, and as a function of stellar mass (M_\star). Blue, green and red populations of galaxies were defined using the colour bimodality described in §3.4.3. The colour fraction in the clusters were estimated in the sample of cluster galaxies that are not part of a substructure.

Spectroscopic Sample

The colour fractions of galaxies in the spectroscopic sample were estimated taking into account the effect of spectroscopic incompleteness (see §3.3.1). In practice, we corrected galaxy counts by weighting each galaxy with $W_i = 1/C$, where C is the spectroscopic completeness estimated in bins of distance and magnitude as described in §3.3.1. To increase the statistics in the spectroscopic sample, we merged the spectroscopic member catalogues for both clusters. We also merged the catalogue for all identified substructures. We estimated the fractions of blue (f_b), green (f_g) and red (f_r) galaxies in the whole cluster sample and in the substructures. Error-bars on the fractions were computed using a method based on statistical inference in absence of background contamination (D'Agostini 2004, Cameron 2011). In practice, the uncertainties on the spectroscopic colour fractions were defined as the width of the binomial 68% confidence intervals as discussed in Cameron (2011).

The optically selected red sequence may be contaminated by dust-obscured star-forming galaxies (see e.g.: Wolf et al. 2005, Haines et al. 2008). For this reason our colour fractions are corrected for contamination by dusty star-forming galaxies as illustrated in Section 3.4.6.

Our results are shown in Figures 3.5, 3.6 and 3.7, in which we present f_b, f_g and f_r for the clusters and substructures. The left panel of Figures 3.5 and 3.6 shows f_b, f_g and f_r as a function of projected distance from the cluster centre normalised by $r_{200,cl}$. The right panel presents f_b, f_g and f_r as a function of projected distance from the cluster centre and substructure centre, for cluster and substructure galaxies, respectively. These projected distances were normalised by r_{200} using the values for the galaxy clusters or substructures accordingly. Instead, the left panel of Figure 3.7 shows f_b, f_g and f_r as a function of R_c magnitude for cluster and substructure galaxies, and the right panel presents f_b, f_g and f_r as a function of $\log(M_\star/M_\odot)$.

In Figures 3.5, 3.6 and 3.7 we have added the observed fractions of field galaxies for comparison purposes. The dotted line represents the fraction of blue, green and red

field galaxies. These fractions were estimated using the colour bimodality, as for the spectroscopic sample. The counts in the red and blue fractions were corrected by the contamination in the red sequence due to dusty star-forming galaxies. The dash-dotted line represents the fraction of star-forming (f_{SF}) and passive (f_P) galaxies in the field, accordingly. The f_{SF} and f_P were estimated using the UVJ -diagram (Wuyts et al. 2007, Patel et al. 2011, Nantais et al. 2016). The selection of the field sample is described in §3.4.6. These results will be discussed in §3.5.

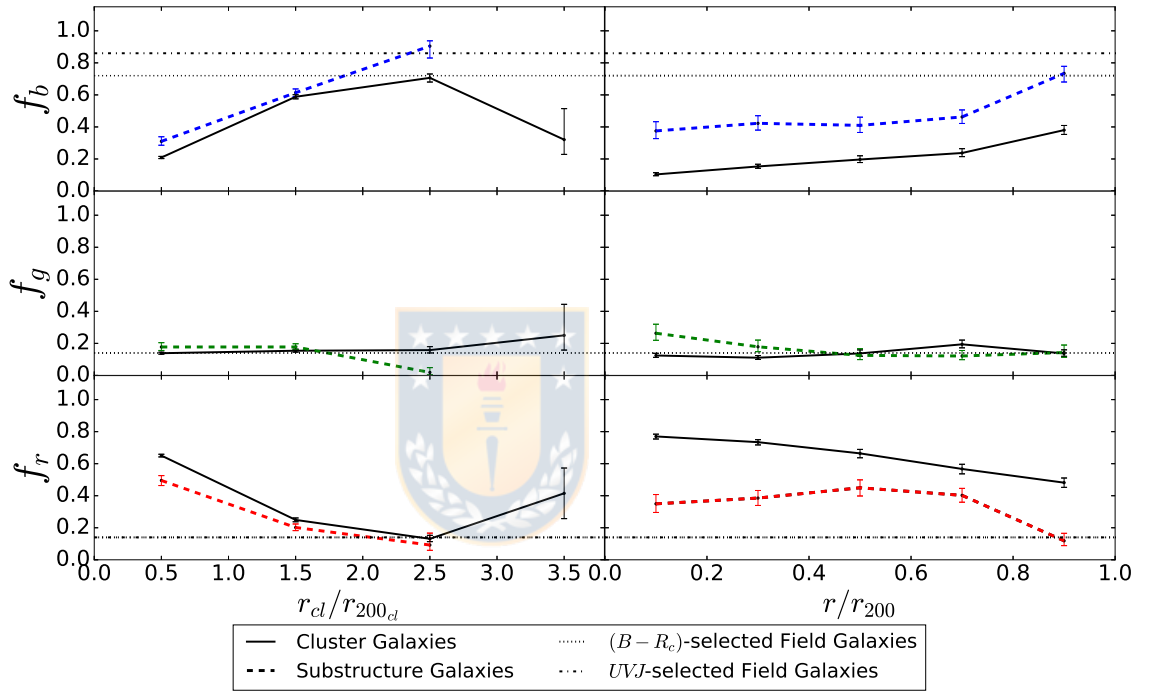


Figure 3.5 Colour fraction as a function of projected distance. Left panel: Fraction of blue (f_b), green (f_g) and red (f_r) galaxies as a function of projected distance from the cluster centre. Right panel: f_b , f_g and f_r as a function of projected distance from cluster or substructure centre. The dotted horizontal black lines represent f_b , f_g and f_r in the field. The dash-dotted horizontal black lines represent the fractions of star-forming (f_{SF}) and passive galaxies (f_P) in the field. Galaxy fractions in the field correspond to a mean value. Galaxy clusters and substructures have lower fractions of blue galaxies than the fraction of star-forming galaxies observed in the field, indicating that cluster and substructures are more efficient in producing red galaxies. Source: Olave-Rojas et al. (2018)

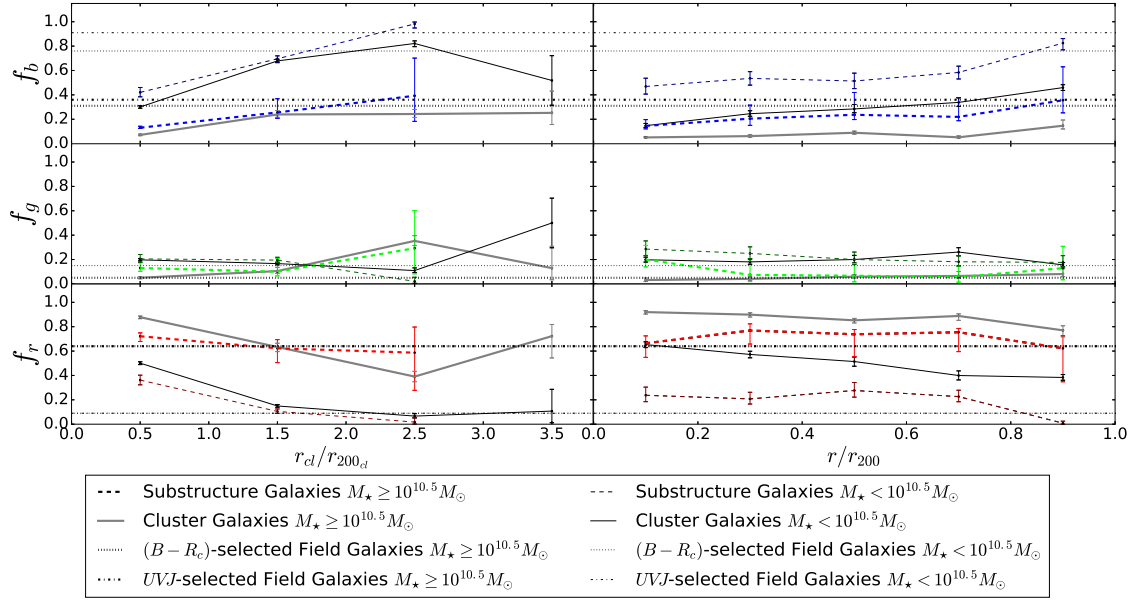


Figure 3.6 Colour fraction as a function of projected distance in bins of stellar mass. Left panel: Fraction of blue (f_b), green (f_g) and red (f_r) galaxies as a function of projected distance from the cluster centre. Right panel: f_b , f_g and f_r as a function of projected distance from cluster or substructure centre. The dotted horizontal black lines represent f_b , f_g and f_r in the field. The dash-dotted horizontal black lines represent the fractions of star-forming (f_{SF}) and passive galaxies (f_p) in the field. Galaxy fractions as a function of projected distance in all environments were estimated by separating galaxies in two bins of stellar mass in massive ($M_\star \geq 10^{10.5} M_\odot$) and less massive galaxies ($M_\star < 10^{10.5} M_\odot$). The fraction of red galaxies is higher for massive galaxies independent of the environment. However, in dense environments the fraction of red galaxies is higher than in the field, indicating that cluster and substructures are more efficient in producing red galaxies. Source: Olave-Rojas et al. (2018)

Spectrophotometric Sample

We determine the number of blue, green and red galaxies, in the spectrophotometric sample, using the same approach as for the spectroscopic sample (see §3.4.3). However, when using photometric redshifts to select cluster members, we are likely to include field interlopers as a result of the uncertainties on z_{phot} , which are larger than those of spectroscopic redshifts. Nevertheless, we can statistically estimate the expected contribution of field interlopers at the cluster redshift and correct our colour fractions by the field contamination.

To estimate the contribution of field galaxies in our estimated colour fractions we use the COSMOS/UltraVISTA catalogue published by Muzzin et al. (2013) to build a sub-

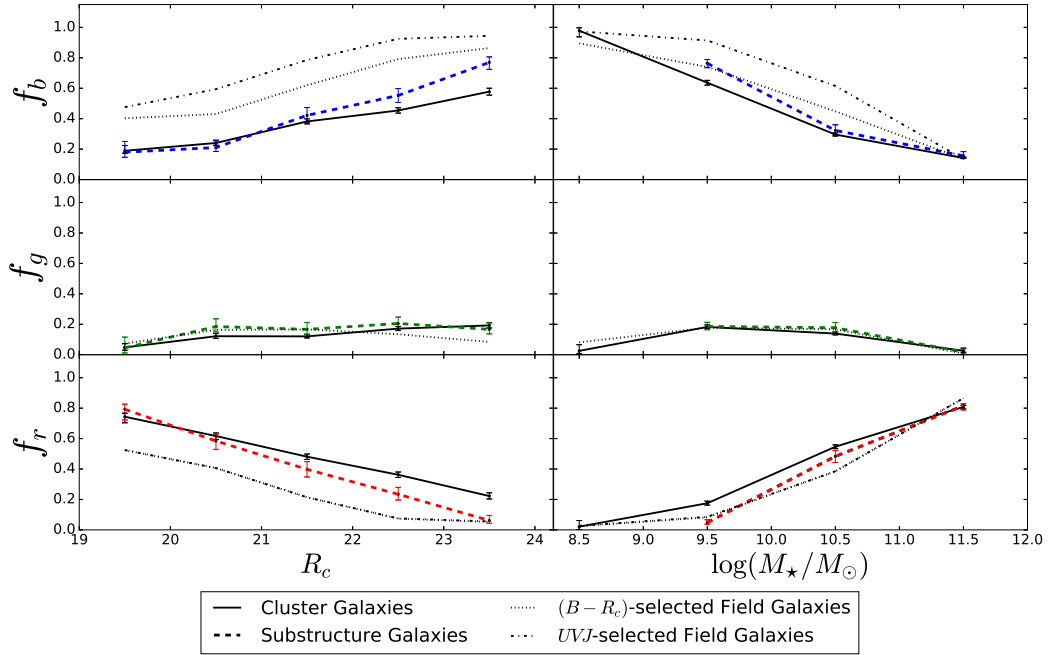


Figure 3.7 Colour fraction as a function of apparent magnitude and stellar mass. Left panel: Fractions of blue (f_b), green (f_g) and red (f_r) galaxies in galaxy clusters and substructures as a function of R_c apparent magnitude. Right panel: f_b , f_g and f_r as a function of $\log(M_\star/M_\odot)$. The dash-dotted black lines represent the fractions of star-forming (f_{SF}) and passive galaxies (f_P) in the field. The fraction of blue galaxies increases with increasing R_c magnitude and decreasing stellar mass in all environments, but the fraction of star-forming galaxies in the field is higher than the fraction of blue galaxies in cluster or substructures. Source: Olave-Rojas et al. (2018)

sample of 3,166 field galaxies at $0.36 < z < 0.46$. The COSMOS/UltraVISTA field sample covers 1.62 deg^2 of the Cosmic Evolution Survey (COSMOS, Scoville et al. 2007) and the sources in the catalogue have been selected from the UltraVISTA K_s survey (McCracken et al., 2012) reaching a depth of $K_{s,tot} = 23.4 \text{ mag}$ (90% completeness). The UltraVISTA survey was carried out with the VISTA InfraRed CAMera (VIRCAM, Dalton et al. 2006) on the Visible and Infrared Survey Telescope for Astronomy (VISTA, Emerson et al. 2006) at the ESO/Paranal Observatory. The COSMOS/UltraVISTA sample is available in the UltraVISTA web repository⁹ and provides a point-spread function (PSF) matched photometry in 30 photometric bands covering the wavelength range of $0.15 - 24 \mu\text{m}$, z_{phot} , stellar masses and rest-frame U , V , and J photometry of 262,615

⁹<http://www.strw.leidenuniv.nl/galaxyevolution/ULTRAVISTA/Ultravista/K-selected.html>

sources, as discussed in Muzzin et al. (2013).

The blue, green and red populations of our sample of 3,166 field galaxies at $0.36 < z < 0.46$ were defined in the same way as it was done with the clusters, using the colour bimodality described in §3.4.3. The colour fractions (f_b, f_g and f_r) of field galaxies were used to infer the contamination in the colour fractions in clusters/substructures due to field background and foreground sources. To correct our colour fractions in the spectrophotometric sample for background contamination we use an approach based on statistical inference. In practice we build a posterior probability distribution in which the colour fractions from clusters/substructures are considered as signal and the colour fractions from field are considered as noise. The full mathematical derivation of this approach is presented in D’Agostini (2004) (see also Cameron 2011). In the same way as Cerulo et al. (2017) we defined our background-corrected colour fractions in galaxy clusters/substructures as the median of the posterior probability distribution. The uncertainty in our background corrected colour fractions was defined as the 68% credible interval of the distribution.

Our blue and red galaxy fractions in cluster, substructures and the field were further corrected for contamination of dusty star-forming galaxies on the red sequence using the *UVJ*-diagram as a diagnostic tool to distinguish young, star-forming and dusty from old and passive galaxies (Wuyts et al. 2007, Patel et al. 2011, Nantais et al. 2016). We used the *UVJ* selection proposed by Williams et al. (2009) to select quiescent galaxies and clean the red sequence in the clusters, substructures and field from dusty star-forming contaminants. In our sample of 3,166 field galaxies at $0.36 < z < 0.46$ from COSMOS/UltraVISTA we found that 40% of the galaxies selected on the field red sequence are dusty-star forming galaxies. To estimate the contamination of dusty star-forming galaxies in the red sequence in the cluster centres ($r < r_{200}$) we matched, using R.A. and Dec., the spectrophotometric member catalogue with the photometric catalogue from HST. We set an aperture of 1” as the maximum separation between the matched galaxies. We found that 5% of the selected galaxies in the red sequence of the clusters in the inner regions ($r < r_{200}$) are dusty star-forming galaxies. Finally, to estimate the contamination in the substructures and in outer regions of the clusters ($r > r_{200}$) we used the groups catalogue from COSMOS published by George et al. (2011) limited to the redshift of the clusters ($0.36 < z < 0.46$). The COSMOS groups in this redshift range are similar, in terms of mass and size, to the selected substructures. We found that 17% of the galaxies selected

on the red sequence of the COSMOS groups are dusty star-forming. Our results will be discussed in §3.5.

Figures 3.8, 3.9 and 3.10 show the f_b , f_g and f_r as a function of distance from the overdensity centre, R_c magnitude and stellar mass for cluster and substructure galaxies. These results will be discussed in §3.5. In the figures we have added the fractions of blue, green and red field galaxies. These fractions were estimated in our sample of 3,166 field galaxies at $0.36 < z < 0.46$ after removing group members according to the catalogue of George et al. (2011).

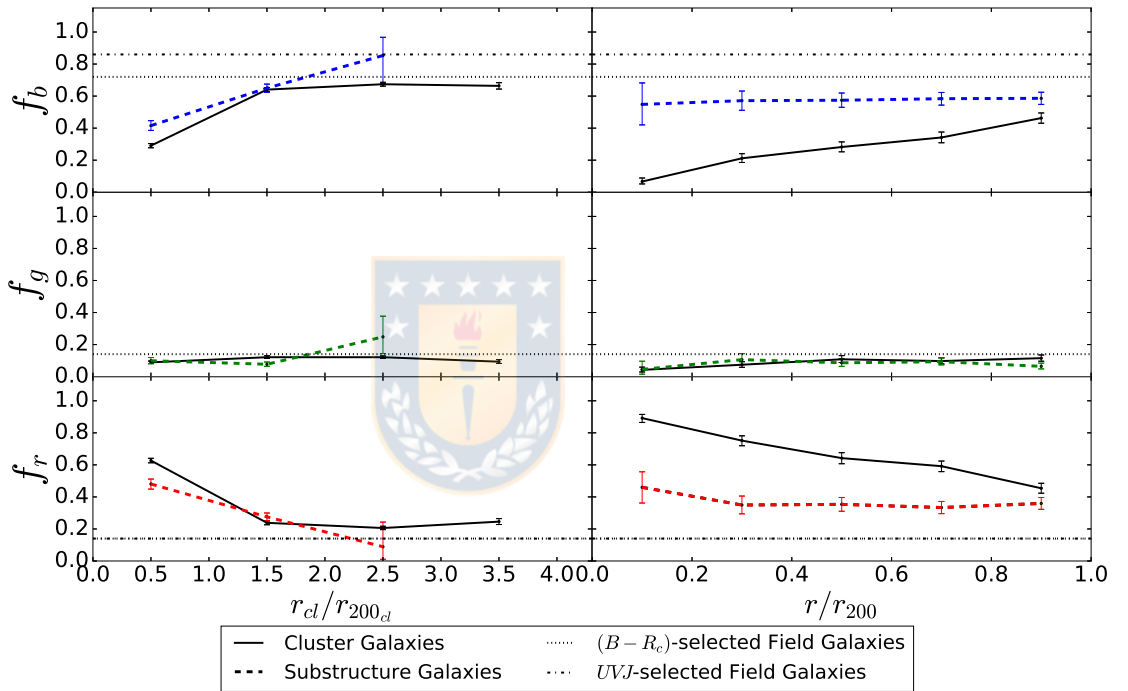


Figure 3.8 Background-corrected colour fractions as a function of projected distance normalised by r_{200} . Left panel: Fractions of blue (f_b), green (f_g) and red (f_r) galaxies as a function of projected distance from the cluster centre. Right panel: f_b , f_g and f_r as a function of projected distance from cluster or substructure centre, accordingly. The dotted horizontal black line represents the f_b , f_g and f_r of field galaxies, while the dash-dotted horizontal black lines represent the fractions of star-forming (f_{SF}) and passive galaxies (f_P) in the field. Galaxy fractions in the field are mean values. In general, galaxies in overdensities (clusters and substructures) have higher f_r than in the field. Source: Olave-Rojas et al. (2018)

Since we found that 40% of the galaxies selected on the field red sequence are dusty-star forming galaxies, we use the UVJ -diagram (Wuyts et al. 2007, Patel et al. 2011,

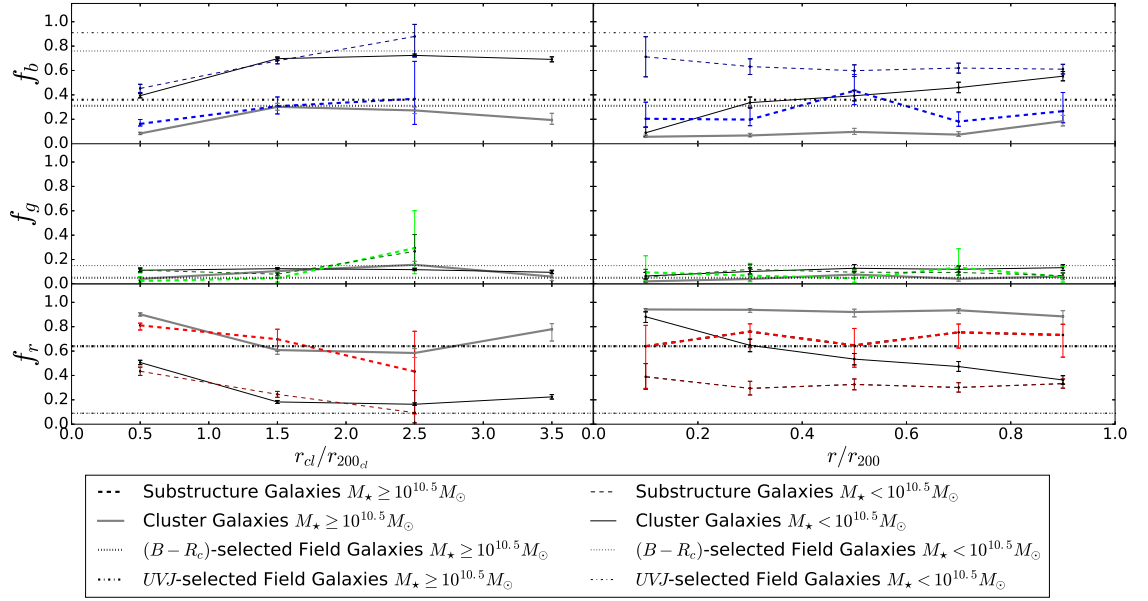


Figure 3.9 Background-corrected colour fractions as a function of projected distance in bins of stellar mass normalised by r_{200} . Left panel: Fractions of blue (f_b), green (f_g) and red (f_r) galaxies as a function of projected distance from the cluster centre. Right panel: f_b , f_g and f_r as a function of projected distance from cluster or substructure centre, accordingly. The dotted horizontal black line represents the f_b , f_g and f_r of field galaxies, while the dash-dotted horizontal black lines represent the fractions of star-forming (f_{SF}) and passive galaxies (f_P) in the field. Galaxy fractions in the field are mean values. Galaxy fractions as a function of projected distance in all environments were estimated by separating galaxies in two bins of stellar mass in massive ($M_\star \geq 10^{10.5} M_\odot$) and less massive galaxies ($M_\star < 10^{10.5} M_\odot$). In general, independent of the stellar mass, galaxies in dense environments such as clusters and substructures tend to be redder than galaxies in the field. Source: Olave-Rojas et al. (2018)

Nantais et al. 2016) to estimate the fraction of star-forming (f_{SF}) and passive (f_P) galaxies in the field. In the clusters/substructures we cannot use the UVJ -diagram to estimate the f_{SF} and f_P because there are not data in the UVJ -bands that cover the outer regions of the clusters ($r > r_{200}$). However, we correct the colour fractions for cluster and substructure members, in both the spectroscopic and spectrophotometric samples, for the contamination from dusty star-forming galaxies derived from the CLASH HST data and the COSMOS groups. The fractions shown in Figures 3.5 – 3.10 are all corrected for contamination from dusty star-forming galaxies.

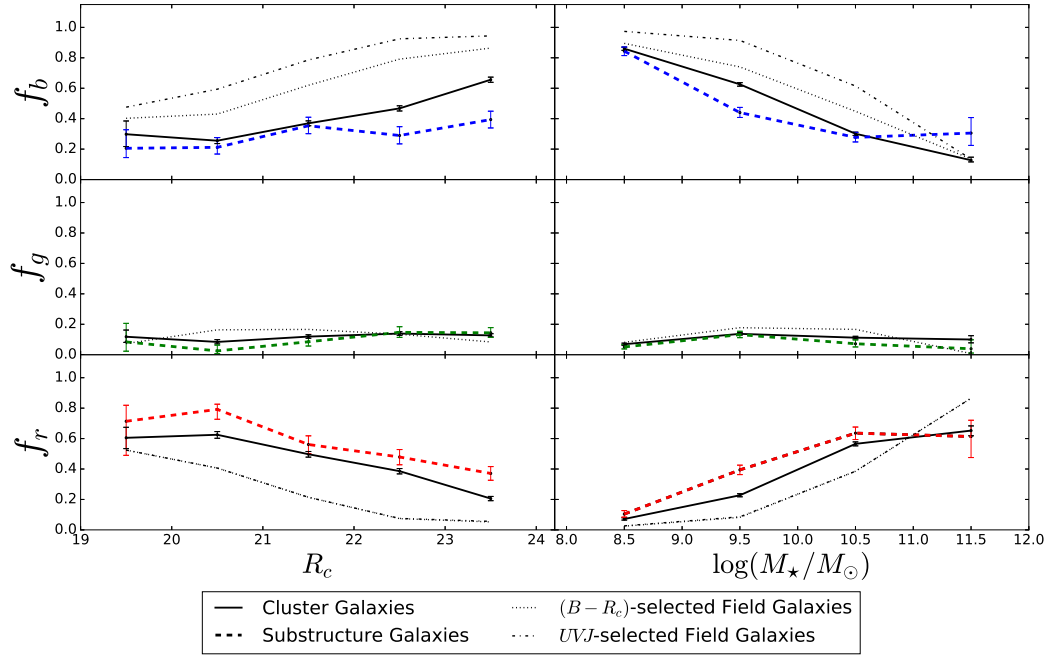


Figure 3.10 Background-corrected colour fractions as a function of apparent magnitude and stellar mass. Left panel: Background-corrected colour fractions for clusters and substructures as a function of R_c apparent magnitude. Right panel: Background-corrected colour fractions for clusters and substructures as a function of $\log(M_\star/M_\odot)$. The dashed black curve represents the f_b, f_g and f_r of field galaxies, while the dash-dotted black lines represent the fractions of star-forming (f_{SF}) and passive galaxies (f_P) in the field. Galaxy fractions in the field were estimated in bins of R_c -band magnitude or stellar mass. The fraction of red or quiescent galaxies increases towards bright magnitudes and massive galaxies in all environments. Source: Olave-Rojas et al. (2018)

3.4.7 Substructure Quenching Efficiency

In our analysis, we assume that the colour change of galaxies in clusters/substructures is associated with the migration of galaxies from the blue cloud to the red sequence in the CMD. This migration is caused by the quenching of star-formation (e.g Peng et al. 2010). To quantify the role of the substructures in the star formation quenching, or pre-processing, we estimated the environmental quenching efficiency (ϵ_q ; Peng et al. 2010, Peng et al. 2012, Nantais et al. 2016), or conversion fraction, because it quantifies the fraction of galaxies that would be blue in the field but are red in a denser environment (e.g cluster or substructures; Peng et al. 2010). The environmental quenching efficiency is defined as follows:

$$\epsilon_q = \frac{(f_{r,dense} - f_{r,field})}{f_{b,field}}, \quad (3.7)$$

where in this equation, ϵ_q is the environmental quenching efficiency, $f_{r,dense}$ is the red fraction in a dense environment (cluster or substructure), and $f_{r,field}$ and $f_{b,field}$ are the red and blue fractions in the field, respectively. In our sample, we estimated ϵ_q in clusters and substructures as a function of projected distance from the cluster centre, normalised by r_{200} . Besides, we estimated the ϵ_q in cluster and substructure as a function of projected distance from cluster or substructure centre normalised by r_{200} of the cluster or substructure, accordingly. ϵ_q is calculated in the same bins used to derive colour fractions. The uncertainty on the environmental quenching efficiency was defined, in each bin of projected distance, as the 68% width of the distribution of ϵ_q after 100,000 Monte-Carlo iterations performed by randomly perturbing the values of the colour fractions within their error bars. In Table 3.4 we summarise our mean environmental quenching efficiency in clusters and substructures, estimated using the spectroscopic and spectrophotometric samples. Our results are presented in Figures 3.11 – 3.13, and will be discussed in §3.5.

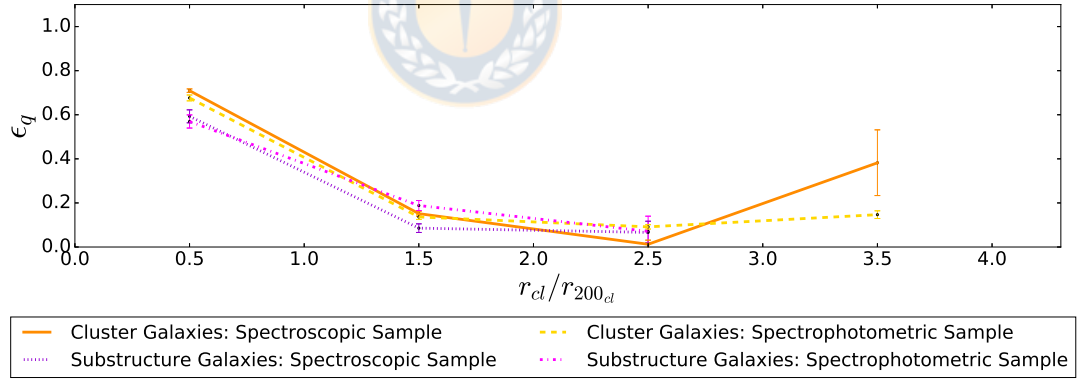


Figure 3.11 Environmental quenching efficiency in clusters and substructures calculated with equation 3.7 (Peng et al., 2010) as a function of projected distance from the cluster centre normalised by $r_{200,cl}$. The solid brown and dashed yellow lines represent the ϵ_q in the clusters for the spectroscopic (see §3.4.1) and spectrophotometric (see §3.4.4) samples, respectively. The dotted indigo and dash-dotted magenta lines represent the ϵ_q in the substructures for the spectroscopic and spectrophotometric samples, respectively. In the outskirts of clusters ($r > r_{200,cl}$) the ϵ_q of substructures becomes comparable to the ϵ_q of clusters. Source: Olave-Rojas et al. (2018)

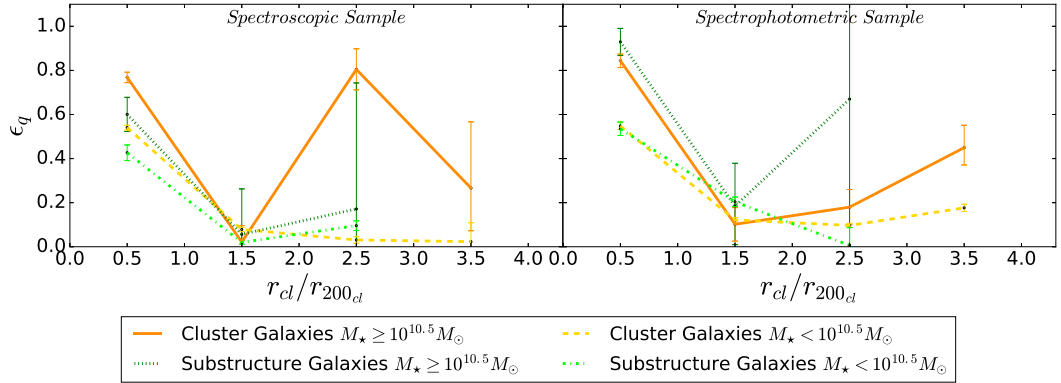


Figure 3.12 Environmental quenching efficiency separated by mass in massive ($M_{\star} \geq 10^{10.5} M_{\odot}$) and less massive galaxies ($M_{\star} < 10^{10.5} M_{\odot}$) in clusters and substructures calculated with equation 3.7 (Peng et al., 2010) as a function of projected distance from the cluster centre normalised by $r_{200_{cl}}$. The solid orange and dashed gold lines represent the ϵ_q in the clusters for massive and less massive galaxies, respectively. The green dotted and dash-dotted lines represent the ϵ_q in substructures. Left panel: spectroscopic sample. Right panel: spectrophotometric sample. The environmental quenching efficiency is higher in massive galaxies. Source: Olave-Rojas et al. (2018)

Table 3.4 Mean environmental quenching efficiency in clusters and substructures.

Environment	Clusters			Substructures		
	All Galaxies	Massive Galaxies	Less Massive Galaxies	All Galaxies	Massive Galaxies	Less Massive Galaxies
$r_{cl}/r_{200_{cl}}$						
Spectroscopic Sample	31 ± 22	47 ± 32	17 ± 5	25 ± 18	28 ± 18	18 ± 11
Spectrophotometric Sample	26 ± 5	39 ± 26	24 ± 12	28 ± 17	59 ± 25	28 ± 18
r/r_{200}						
Spectroscopic Sample	70 ± 7	73 ± 11	55 ± 7	35 ± 11	55 ± 19	21 ± 4
Spectrophotometric Sample	73 ± 5	92 ± 5	64 ± 29	40 ± 5	54 ± 8	38 ± 4

3.5 Discussion

3.5.1 Substructure detections

The first difficulty to overcome in studies of pre-processing is the accurate detection of substructures and infalling groups. This is due mainly to the limitations given by the amount of data available, the dynamical state of the clusters and the methods used in the search and characterisation of the substructures (e.g Cohn 2012, Tempel et al. 2017).

In order to find the substructures in MACS0416 and MACS1206 we used the DS-test Dressler & Shectman (1988) along with clustering algorithms (K-means and DBSCAN; Lloyd 2006, Ester et al. 1996). As shown in §3.4.2 we found more substructures in MACS0416 than in MASC1206. This result could be a consequence of the dynami-

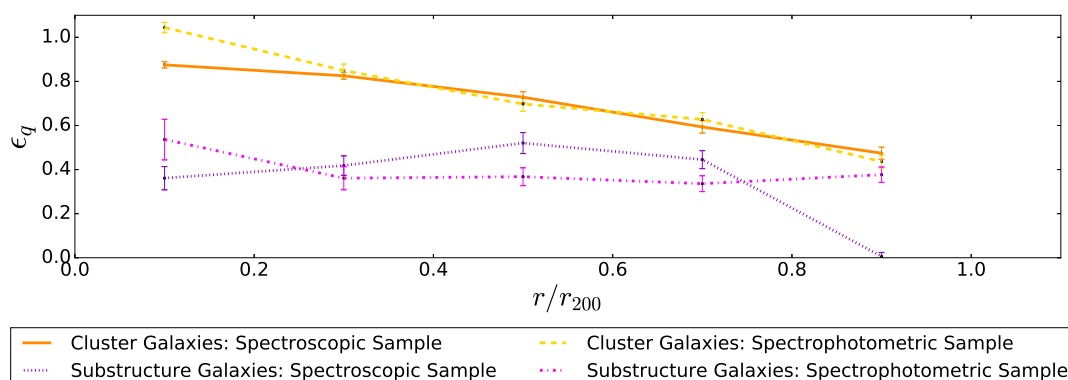


Figure 3.13 Environmental quenching efficiency as a function of distance from the overdensity centre in clusters and substructures calculated with equation 3.7 (Peng et al., 2010) as a function of projected distance from the cluster centre or substructure centre normalised by r_{200} of the cluster or substructure, accordingly. The solid brown and dashed yellow lines represent the ϵ_q in the clusters for the spectroscopic (see §3.4.1) and spectrophotometric (see §3.4.4) samples, respectively. The dotted indigo and dash-dotted magenta lines represent the ϵ_q in the substructures for the spectroscopic and spectrophotometric samples, respectively. In the innermost regions ($r < r_{200}$) of the overdensity (either cluster or substructure) clusters are more efficient than substructures in quenching star formation. Source: Olave-Rojas et al. (2018)

cal state of the clusters. Cohn (2012) shows that the presence of galaxy substructures is correlated with the dynamical state of a cluster. While MACS0416 is a merger between two large structures (Balestra et al., 2016), MACS1206 is a relaxed cluster (Biviano et al., 2013). However, according to Tempel et al. (2017) the ability to detect substructures depends on the data available regardless of the method used. In our study, as shown in §3.2.2, we have more spectroscopic data for MACS0416 than MACS1206 and this could be the reason why we have more spectroscopic members in MACS0416 than in MACS1206 (see 3.4.1), and thus more substructures in MACS0416 than MACS1206. This idea is supported by a simple test that we have done in which we have randomly selected the same number of spectroscopic members in MACS0416 and in MACS1206. In this new sample for MACS0416 we only find 10 substructures. Furthermore, the fall of spectroscopic completeness spectroscopic completeness at $r \geq 2 \times r_{200}$ (shown in §3.3.1) may affect our ability of detecting substructures (Biviano et al. 2013, Balestra et al. 2016).

We note that the $\sim 40\%$ of our identified substructures are in the inner ($r \leq r_{200}$) regions of the clusters, whereas the $\sim 60\%$ are in the outer ($r > r_{200}$) regions (see §3.4.2). Our results are in agreement with observational and theoretical studies (e.g Jaffé et al.

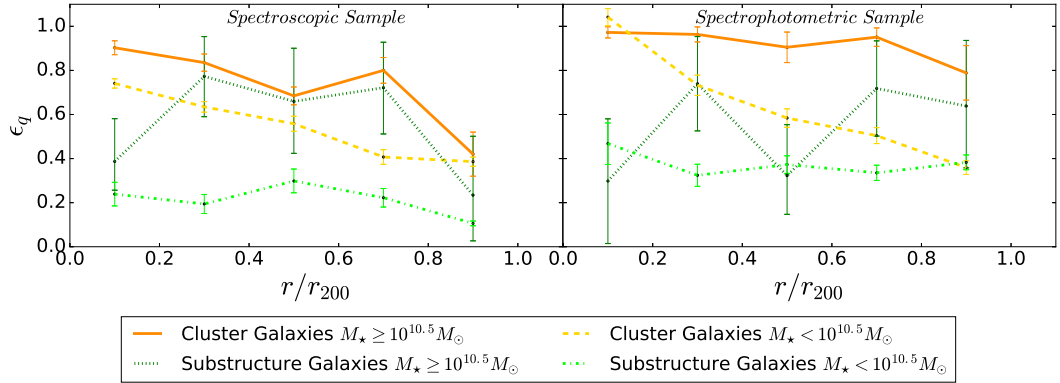


Figure 3.14 Environmental quenching efficiency as a function of distance from the overdensity centre separated by mass in massive ($M_{\star} \geq 10^{10.5} M_{\odot}$) and less massive galaxies ($M_{\star} < 10^{10.5} M_{\odot}$) in clusters and substructures calculated with equation 3.7 (Peng et al., 2010) as a function of projected distance from the cluster centre or substructure centre normalised by r_{200} of the cluster or substructure, accordingly. The solid orange and gold dashed lines represent the ϵ_q in the clusters for massive and less massive galaxies, respectively. The solid orange and dashed gold lines represent the ϵ_q in the substructures for massive and less massive galaxies, respectively. Left panel: spectroscopic sample. Right panel: spectrophotometric sample. The environmental quenching efficiency is higher in massive galaxies. Source: Olave-Rojas et al. (2018)

2016, Vijayaraghavan & Ricker 2013, respectively) in which it is shown that most of the identifiable substructures are located in the outermost regions of galaxy clusters (at $r > r_{200}$). In addition, Vijayaraghavan & Ricker (2013) suggest that when a group falls into a cluster and is at a distance of $\sim 2 \times r_{200}$ from the cluster centre, the group is stretched out along the direction of infall, due to the effect of the cluster gravitational potential on the group. In our case, using visual inspection (see §3.4.2), we found that substructures in the outer regions of the clusters, especially in MACS0416, even at $2 \times r_{200}$, tend to be less elongated than substructures in the inner regions of the clusters. Interestingly, we notice that the inner ($r \leq r_{200}$) elongated substructures found in MACS0416 are elongated along the NE-SW direction, the same in which this cluster is elongated (Balestra et al., 2016). This supports the notion that the inner substructures are more susceptible to the gravitational effects of the overall cluster potential.

3.5.2 Colour fractions in substructures and galaxy clusters

Figure 3.3 shows that galaxies in substructures show the same bimodality in colours observed in the entire clusters. We note the absence of very bright red and blue galaxies in substructures. This could be a consequence of the selection criteria for the spectroscopic targets since the spectroscopic target selection was mostly done in a colour-colour space.

The well established morphology-density relation (Dressler 1980, Postman et al. 2005) can be translated to a morphology-clustercentric radius relation (e.g Whitmore et al. 1993, Goto et al. 2003). That is, early-type galaxies are more frequent in the cluster core while late-type galaxies are more frequent in the outer regions of clusters. Moreover, the morphology of galaxies is related with other physical properties such as their stellar masses, colours and star-formation rates. In this sense, the morphology of galaxies can also be inferred from their colours, for example: early-type galaxies tend to be red, whereas late-type galaxies tend to be blue. In this context, the relation between the morphology of galaxies and the environment can be explained by a colour-environment relation (Blanton et al. 2005, Skibba et al. 2009, Grützbauch et al. 2011b).

In the case of MACS0416 and MACS1206, the spectroscopic colour fractions as a function of projected distance from the cluster centre obtained in §3.4.6 (see left panel of Figure 3.5) show that galaxies in clusters and substructures follow a colour-clustercentric radius relation. Galaxies within $r_{200,cl}$, independent of whether they are part of a cluster or substructure, tend to be redder than galaxies beyond $r_{200,cl}$. This suggests that this result is likely a consequence of the effect of the cluster environment over the properties of galaxies traced by their colours (e.g Miller 1986, Byrd & Valtonen 1990, Boselli et al. 2014). Moreover, studying the colour fraction of galaxies as a function of the distance from the cluster or substructure centre (see right panel of Figure 3.5), we note that the total colour-clustercentric radius relation in substructures follows similar trends observed in the main clusters. According to this, substructures may be considered as down-scaled versions of clusters in which galaxy properties, traced by their colours, have been sculpted by the gravitational potential and physical processes within the substructures (e.g. ram-pressure stripping and galaxy-galaxy interactions), which can stop star-formation and turn galaxies red.

Figure 3.6 shows the spectroscopic colour fractions as a function of projected distance by separating galaxies in all environments according to their stellar masses in massive ($M_{\star} \geq 10^{10.5} M_{\odot}$) and less massive ($M_{\star} < 10^{10.5} M_{\odot}$). We note that fraction of green

galaxies is constant in all environments, independent of the stellar mass of the galaxies and that massive galaxies tend to be red independent of the environment in which they are located. Besides, the fraction of red galaxies (f_r) in clusters and substructures at $r < 1.5 \times r_{200_{cl}}$ is higher than the f_r in the field, independent of the stellar mass. This result is in agreement with the result presented in the left panel of Figure 3.5, in which the cluster environment models galaxy properties traced by their colours at least within $1.5 \times r_{200_{cl}}$. Beyond $1.5 \times r_{200_{cl}}$ f_r in all environments become comparable. The f_r of massive galaxies in substructures is slightly higher than in the clusters. Moreover, right panel of Figure 3.6 shows that the f_r in dense environments tend to be higher than the fraction of red galaxies in the field. This suggest that denser environments are more effective in producing red galaxies independent of the stellar masses of the galaxies. Figure 3.9 shows that the results for the spectroscopic sample are reproduced by the spectrophotometric sample.

To test the colour fractions estimated using the spectroscopic sample and motivated by the low spectroscopic completeness beyond $r > 1.5 \times r_{200}$, we increased the statistics in the sample by adding to the spectroscopic sample z-phot selected galaxies at all radii from the cluster centres (see §3.4.4). For substructures, following George et al. (2011), we added z_{phot} selected galaxies only within r_{200} from the substructure centres (see §3.4.4). Figure 3.8 (left panel) shows that the colour fractions as a function of the projected distance from the cluster centre obtained with the spectrophotometric sample reproduce those of the spectroscopic sample. Figure 3.8 (right panel) shows that the results for the spectroscopic sample are reproduced by the spectrophotometric sample.

In the spectroscopic and background-corrected colour fractions as a function of distance (see Figures 3.5 and 3.8) we see that the fraction of blue galaxies is larger in substructures than in the cluster, at all distances. Substructures host, on average, less dense environments than the entire cluster, thus allowing for a higher star formation activity (e.g. Dressler 1980, van der Wel et al. 2007). Interestingly, as noted in Perez et al. 2011, Jaffé et al. 2016, galaxy-galaxy interactions, especially those involving gas-rich galaxies, can induce bursts of star formation. This may also contribute to the enhanced blue fraction in substructures. The fraction of red galaxies in clusters and substructures is higher for massive galaxies than for less massive galaxies. This suggests that at such stellar masses internal processes play a significant role in quenching star formation.

The uncertainties in the colour fractions, in the spectroscopic sample, as a function of projected distance from the centre of the overdensity (either cluster or substructure) are

of the order of $\sim 10\%$. We note here that our cluster sample does not include substructure members; the results of this Chapter, however, do not change if we consider substructure members in the cluster sample.

With only 3 photometric bands available for MACS0416, it is not possible to obtain reliable stellar masses through SED fitting. For this reason we decided to estimate the stellar mass of galaxies using the empirical approach proposed by Bell et al. (2003) (see §3.4.5). Since the two clusters are almost at the same redshift, we used the R-band apparent magnitude as a proxy for galaxy luminosity. The colour fractions as a function of R-band luminosity and stellar mass are shown in Figures 3.7 and 3.10 for the spectroscopic and “spectrophotometric” samples, respectively. We see that the colour fractions follow the same trends with luminosity or stellar masses regardless of the galaxies being in the cluster or the substructures.

These results support the notion that internal physical mechanisms, related to galaxy stellar mass, act independently from the environment in quenching star formation in galaxies. Interestingly, when considering the spectrophotometric sample, the red fraction is higher in substructures than in the clusters. Although still consistent within the errors, this result seems to be at odd with what we see in the spectroscopic sample, where the red fraction in substructures is slightly lower than in the clusters. We argue that this could be a consequence of the small statistics in the spectroscopic sample as we go towards the cluster outskirts, which results in the loss of substructure members. As a result, the substructure red fraction in the spectroscopic sample may be slightly underestimated. If the effect that we see in the spectrophotometric sample is real, then this suggests that the environment of substructures favours the quenching of star formation and thus pre-processing is significant in the overall quenching of star formation in clusters of galaxies.

3.5.3 Evidence for pre-processing from the colour fractions in substructures

An easy way to detect the existence of pre-processing in galaxy clusters consists in comparing the fractions of quiescent or star-forming galaxies in cluster outskirts and in the field. For example, Wetzell et al. (2013) find that galaxies in groups or satellite groups have lower SFR than in the field. Hou et al. (2014) find that the fraction of quiescent galaxies in the outer ($2 - 3 \times r_{200}$) substructures of galaxy clusters is higher than in the

field. Similarly, Haines et al. (2015) show that the fraction of star-forming galaxies in clusters is lower than in the field out to $3 \times r_{200}$ from the cluster centre. All these results point towards the existence of pre-processing.

In this work we compare the fractions of blue and red galaxies in the clusters with the fractions of star-forming and quiescent galaxies in the COSMOS/UltraVISTA field. As discussed in Section 3.4.4, we selected quiescent and star-forming galaxies in the field with the UVJ diagram. This selection cannot be done in the two clusters analysed in this work as the available photometry does not cover the rest-frame J band at the redshifts of the clusters. We therefore compare the fractions of blue and red galaxies in clusters and substructures with the fractions of quiescent and star-forming galaxies in the field. This comparison can be done as the fractions of blue and red galaxies in clusters and substructures are corrected for contamination of dusty star-forming galaxies as discussed in Section §3.4.6.

Figure 3.5 shows that in the spectroscopic sample the fractions of red galaxies remain higher than the field in the cluster and substructures out to $2 \times r_{200,cl}$ from the cluster centres and $1 \times r_{200}$ from the overdensity centre. At larger distances from the cluster centre ($r > 2 \times r_{200,cl}$) the fraction of quiescent galaxies in the field becomes slightly higher than in substructures. We remind here that the spectroscopic completeness of the sample is a decreasing function of cluster-centric radius (Figure 3.1), implying that results at projected distances greater than $2 \times r_{200}$ may be affected by sample incompleteness even after weighting the observed colour fractions. However, considering the uncertainties on colour fractions, the fraction of red galaxies in substructures is at least comparable to that in the field out to $2.5 \times r_{200,cl}$ from the cluster centre. Figure 3.8 shows, indeed, that when considering also z_{phot} -selected members the fraction of red galaxies in substructures is higher or at least comparable to that in the field out to $2.5 \times r_{200,cl}$ from the cluster centre. In the case of colour fractions as a function of projected distance from the centre of an overdensity, the right panel of Figures 3.5 and 3.8 show that the fraction of red galaxies in substructures is higher than that in the field.

We conclude from this that the trends of the colour fractions with projected distance for cluster and substructure galaxies agree with the existence of pre-processing in galaxy clusters.

Bianconi et al. (2018) studied the star formation in infalling substructures for a sample of clusters at $0.15 < z < 0.3$ selected from the Local Cluster Substructure Survey

(LoCuSS, Smith et al. 2010). They find that the fraction of star-forming galaxies in the substructures is always lower than in the clusters, interpreting this as evidence of pre-processing. Although this result appears in disagreement with our Figures 3.5 and 3.8, we can reconcile our findings with those of Bianconi et al. (2018) by noting that those authors identified substructures using the X-ray luminosity distributions of the clusters. Such a method privileges the selection of the most massive and dense substructures, where the environmental quenching effects are stronger. We also point out that the clusters in Bianconi et al. (2018) are at lower redshifts than ours and thus their substructures are likely to host larger fractions of passive galaxies (see e.g. Li et al. 2009). Finally, these authors restricted themselves only to massive galaxies ($M_{\star} \geq 2 \times 10^{10} M_{\odot}$), which may be more affected by internal quenching processes (see e.g. Muzzin et al. 2012, Gavazzi et al. 2015, also Figures 3.7 and 3.10 in this Chapter). Our results (see Figures 3.6 and 3.9) show that, considering the uncertainties, the fraction of red massive ($M_{\star} \geq 10^{10.5} M_{\odot}$) galaxies in substructures is higher or at least comparable to the fraction of red massive galaxies in the clusters as a function of projected distance from the cluster centre. This result is in agreement with Bianconi et al. (2018). These results are in agreement with some authors (e.g. Grützbauch et al. 2011a) that find that the effects of stellar mass and environments in producing red galaxies are not independent and that massive galaxies are preferentially located in denser environments.

Figure 3.11 shows that the environmental quenching efficiency in substructures is lower than in the main cluster and begins to be comparable to the main cluster at $r > 1 \times r_{200,cl}$. Figure 3.13 shows that the environmental quenching efficiency in clusters is always higher than in the substructures. In particular, we note that while ϵ_q increases towards the cluster centre, it remains approximately constant with the distance from the centre of the substructures. Despite these differences in the spatial distribution of the quenching efficiency, we find that on average ϵ_q has similar values in the main cluster and in the substructures (see Table 3.4). All these results can be explained by the fact that environmental quenching processes are stronger in cluster cores than in substructures. Interestingly, we note that the ϵ_q of massive galaxies ($M_{\star} \geq 10^{10.5} M_{\odot}$) in substructures is higher than ϵ_q of the massive galaxies in the cluster (see right panel of Figure 3.12). Our results could be explained by the fact that in lower-mass environments such as galaxy groups or substructures is more likely to produce red massive galaxies by galaxy mergers than in clusters Mihos (2003). This fact could be indicating that internal and external mechanisms act together

in producing red galaxies in substructures.

We note in Figure 3.14 that the values of ϵ_q for massive and less massive galaxies in the inner regions ($< r_{200}$) of clusters and substructures are consistent between them. However, ϵ_q appears larger for massive galaxies in both the cluster and substructure samples. We need a larger sample to test such a result, which will be addressed in a forthcoming paper.

Kawinwanichakij et al. (2017), using galaxies at $0.5 < z < 2.0$ from the FourStar Galaxy Evolution Survey (ZFOURGE Straatman et al. 2016), found that in the mass range of $8.8 < \log(M/M_\odot) < 10.0$ the environmental quenching efficiency is $\sim 30\%$ at $z < 1$. These authors suggest that, at $z < 1$, environmental quenching plays a key role in suppressing the star-formation in low mass galaxies. In our case, using only the spectroscopic sample, we estimate a mean quenching efficiency of $\epsilon_q = (31 \pm 22)\%$ and $\epsilon_q = (25 \pm 18)\%$ for clusters and substructures, respectively (see Table 3.4). When we use the spectrophotometric sample we obtain a mean quenching efficiency of $\epsilon_q = (26 \pm 16)\%$ for clusters, and a $\epsilon_q = (28 \pm 17)\%$ for substructures (see Table 3.4). Our values are close to those obtained by Kawinwanichakij et al. (2017). Besides, we note that for less massive galaxies ($M_\star < 10^{10.5} M_\odot$) in substructures we found a mean environmental quenching efficiency of the order of $(18 \pm 11)\%$ and $(25 \pm 18)\%$ for the spectroscopic and spectrophotometric samples, respectively. Our mean values are slightly lower than the value found by Kawinwanichakij et al. (2017). However, in the case of massive galaxies ($M_\star \geq 10^{10.5} M_\odot$) we found a mean environmental quenching efficiency in substructures of $\epsilon_q = (59 \pm 25)\%$ for the spectrophotometric sample, this value is higher than the environmental quenching efficiency of massive galaxies in the cluster (see Table 3.4). This suggest that in our studied clusters the environmental quenching plays a role in producing red galaxies in all stellar mass ranges.

3.6 Summary and Conclusions

We have studied the effect of the local environment on the colour of galaxies in two clusters at $z \sim 0.4$ drawn from the CLASH-VLT survey (Rosati et al., 2014). In these clusters, we have identified several substructures using a combination of statistical methods (DS-test) and clustering algorithms (DBSCAN). Most of the identified substructures are located in the cluster outskirts ($r \geq r_{200}$), in agreement with literature results.

We have investigated the spectroscopic and background-corrected colour fraction as a

function of projected distance from the cluster centre for galaxies in cluster and substructures, and as a function of projected distance from the centre of the overdensity (either cluster or substructure) for clusters and substructures, accordingly. We found that the colour-clustercentric radius relation is well established both in clusters and substructures. In addition we found that the colour-clustercentric radius relation in the clusters can be reproduced by the colour-clustercentric radius relation in substructures. This suggests that substructures may be considered as down-scaled versions of clusters, in which the internal physical properties of the substructures sculpt galaxy properties such as colours, SFR and morphologies.

We find that the fraction of blue galaxies in both clusters and substructures is lower than the fraction of star-forming galaxies in the field. The fractions of red and blue galaxies in substructures are intermediate between that of the main cluster and the fractions of quiescent and star-forming galaxies in the field. This result supports the notion of the existence of pre-processing in galaxy clusters.

The environmental quenching efficiency in the centres of substructures is lower than in the centres of clusters and becomes comparable to that of the clusters when the distance from the centre of the overdensity increases. We also find that the environmental quenching efficiency of external substructures ($r \geq r_{200}$ from the cluster centres) is comparable to that of the main cluster. The average environmental quenching efficiencies of cluster and substructures are similar.

We find that massive galaxies ($M_{\star} \geq 10^{10.5} M_{\odot}$) tend to be redder than less massive galaxies ($M_{\star} < 10^{10.5} M_{\odot}$) in all environments. However the environmental quenching efficiency of massive galaxies in substructures is higher than the environmental quenching efficiency of galaxies in clusters. This fact suggests that stellar mass and environment play a combined role in producing red galaxies in substructures.

The analysis of MACS0416 and MACS1206 shows that the study of substructures in clusters is fundamental to understand the evolution of galaxies in dense environments. Clusters assembled a significant part of their mass through the accretion of smaller groups, and the properties of galaxies in clusters bear the imprint of this assembly history as we show in this Chapter. The analysis developed in this work will be extended to the entire CLASH-VLT sample; this work is already ongoing and will allow us to study galaxy pre-processing with high statistical significance in a large sample of clusters.

4

Revealing the effects of galaxy interaction in the main galaxies of the southern group Arp 314

The content of this chapter has been sent for publication in Monthly Notices of the Royal Astronomical Society to be published as: “Revealing the effects of galaxy interaction in the main galaxies of the southern group Arp 314” by Torres-Flores S., Amram P., Olave-Rojas D., Muñoz-Elgueta N., Mendes de Oliveira C., de Mello D. F., Urrutia-Viscarra F.

Abstract

We present new Gemini imaging and spectroscopic data of the poorly studied system Arp 314, which consists of a triplet of interacting galaxies. This new imagery exhibiting tidal tails, stellar bridges and shells between the galaxies members and confirms the past interactions. Using this data set, we have analyzed the physical properties of 22 star-forming regions located in the main disk of these galaxies, as well as in the intergalactic medium. All these regions have emission lines typical of young ages and a couple of them display very high $H\alpha$ luminosities ($L_{H\alpha} \sim 10^{40}$ erg s⁻¹). Using the star-forming regions located in Arp 314-1, we derive its gas phase oxygen abundance distribution, which suggests a flatter behavior than the distribution shown by non-interacting systems. This is in agreement with results obtained for other interacting systems and simulations. The presence of gas flows, as indicated by its complex kinematics, could explain this finding. The nuclear region of this galaxy can be classified as a *transition object*. Most of the

star formation in Arp 314-2 is located in a central starburst, where double $H\alpha$ profiles can be identified, as shown by archival Fabry-Perot data. Additionally, we found that the irregular galaxy Arp 314-3 has a low oxygen abundance. Considering its luminosity, this object has a primordial origin, and it was not formed during the interaction event that this system has experienced.

4.1 Introduction

Small groups of interacting galaxies are prime environments at $z\sim 0$ to study galaxy evolution, mainly due to their low velocity dispersions ($\sigma\sim 200\text{ km s}^{-1}$) and low galaxy-galaxy separation (typically of the same order of the galaxy diameter), which facilitates interaction and merging of the galaxy members. Given the strong gravitational encounters that may take place in these small interacting groups (triplets, compact groups and multiplets in general), one can expect substantial galaxy transformation to happen. For example, compact group galaxies are found to often display morphological and kinematic perturbations, depending on the evolutionary stage of the group (e.g. Mendes de Oliveira & Hickson, 1994; Verdes-Montenegro et al., 2001; Amram et al., 2003). Galaxy interactions in small groups are thought to trigger star formation and/or nuclear activity, gas flows, metal mixing and formation of new objects (e.g. Ellison et al. 2008, Ellison et al. 2010, Scudder et al. 2012). In an attempt to find a large sample of groups with star-forming galaxies, Hernández-Fernández & Mendes de Oliveira (2015) have conducted a systematic search of new star-forming compact group of galaxies. A small fraction of them were found within clusters. Indeed, galaxy groups can also play an important role in the pre-processing of galaxies, i.e., galaxies should quench their star-formation in groups prior to the infall into the cluster environment (e.g. Zabludoff & Mulchaey, 1998; Fujita, 2004).

Detailed studies of individual galaxies in small galaxy groups can deliver important information regarding the influence of the environment on their physical properties (star formation, nuclear activity, metallicity, etc). A natural way to study their properties is to analyze spectroscopic data for different regions located across the interacting systems. This analysis can be performed by using multi object capabilities, given the commonly large spatially extent of interacting galaxies, which often have long tails. Kinematic data are extremely useful to search for gas inflows and outflows (e.g. Arribas et al., 2014;

Rupke et al., 2005), which can be associated with nuclear activity and metal mixing. In this sense, the study of the physical and kinematic properties of interacting galaxies is another powerful tool to understand these systems and to determine how important the environment is for galaxy evolution. These points motivated us to use optical spectroscopic and kinematic data to perform a complete study of the galaxy members of the strongly interacting group Arp 314, which is dominated by three late-type galaxies located at small projected distances from one another.

The system Arp 314, at a distance of 51.1 Mpc (Mould et al., 2000, $H_0=73.0 \text{ km sec}^{-1} \text{ Mpc}^{-1}$) was classified the first time by Arp (1966) and it consists of two late-type spiral galaxies (Arp 314-1 and Arp 314-2) and one irregular galaxy (Arp 314-3). The median galaxy separation of this triplet is $\sim 23 \text{ kpc}$ (considering a scale of $14.85 \text{ kpc arcmin}^{-1}$, NED database). *Sloan Digital Sky Survey* (SDSS) images of this system show an extended tidal tail which starts from member Arp 314-2. The neutral gas distribution and content of this system was studied by Nordgren et al. (1997), who found a large H I cloud that covers all members. Torres-Flores et al. (2014a) studied the kinematics of the three main galaxies of Arp 314, by using H α Fabry-Perot data cubes. These authors found perturbed velocity fields for members Arp 314-1 and Arp 314-2, which translated into perturbed rotation curves. Although the dwarf galaxy Arp 314-3 is also perturbed, it displays a clear velocity gradient. Arp 314 is, therefore, an ideal target to investigate environmental effects in galaxies.

This Chapter is organized as follows. In Sections 4.2 and 4.3 we present the data and data analysis. In Section 4.4 we present the results. In Section 4.5 we discuss our results and in Section 4.6 we summarize our results.

4.2 Data

4.2.1 Imaging and spectroscopy

We have obtained u' , g' and r' -band imaging and multi slit spectroscopic data of Arp 314 by using the Gemini MultiObject Spectrograph (GMOS, Hook et al. 2004) at the Gemini South Observatory, under the programme GS-2013B-Q-27 (PI: S. T-F).

We observed five, four and three exposures of 300 seconds each in the filters u' , g' and r' , respectively. This allowed the derivation of a false colour image of the main galaxies

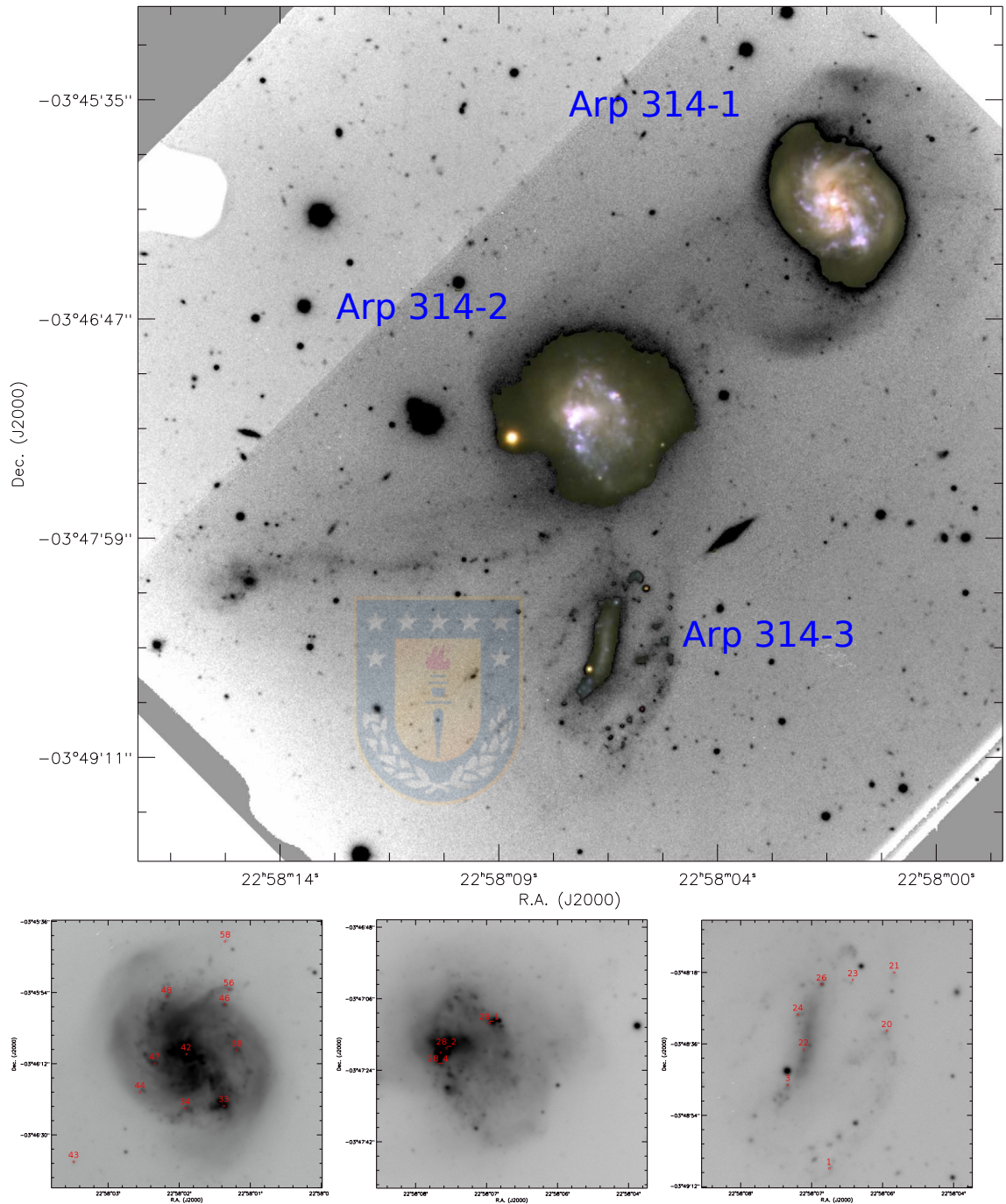


Figure 4.1 r' -band image of Arp 314. Top panel: r' -band high contrast image of Arp 314. Tidal structures and shells can be identified on this image. Overplotted, u' , g' and r' -band Gemini/GMOS false colour images of Arp 314-1 and Arp 314-2 are shown, in order to highlighting the star-forming regions. Bottom panels (left to right): Arp 314-1, Arp 314-2 and Arp 314-3 r' -band images. Regions with spectroscopic data are labeled (see Table 4.1 for coordinates). Source: Torres-Flores et al. (2019)

Table 4.1 Positions, radial velocities and internal extinctions for sources in Arp 314

ID	R.A. (J2000)	Dec. (J2000)	E(B-V) mag	Velocity km s ⁻¹
(1)	(2)	(3)	(4)	(5)
1	22:58:06.898	-3:49:07.46	0.00	3926±95
3	22:58:07.594	-3:48:46.31	0.15	3835±186
20	22:58:05.926	-3:48:32.65	0.00	3649±185
21	22:58:05.798	-3:48:17.89	0.31	3686±42
22	22:58:07.325	-3:48:37.35	0.06	3845±29
23	22:58:06.499	-3:48:19.81	0.63	3788
24	22:58:07.423	-3:48:28.55	0.08	3785±219
26	22:58:07.030	-3:48:20.90	0.18	3798
33	22:58:01.630	-3:46:22.69	0.22	3699
34	22:58:02.280	-3:46:23.29	0.63	3767
38	22:58:01.411	-3:46:08.63	0.32	3645±25
42	22:58:02.261	-3:46:09.57	...	3685±69
43	22:58:04.162	-3:46:36.80	0.00	3664±124
44	22:58:03.043	-3:46:19.21	0.04	3579±192
46	22:58:01.618	-3:45:57.13	0.05	3787±72
47	22:58:02.794	-3:46:11.97	0.19	3606±71
48	22:58:02.597	-3:45:55.13	0.12	3518±73
56	22:58:01.546	-3:45:53.28	0.09	3735±321
58	22:58:01.608	-3:45:41.10	0.09	3721±58
28_1	22:58:07.147	-3:47:12.27	0.14	3525±46
28_2	22:58:07.874	-3:47:18.62	0.22	3541
28_4	22:58:07.968	-3:47:19.67	0.12	3561

of this system, as shown in the top panel of Figure 4.1. On this image it is possible to observe the faint stellar structures visible in the intergalactic medium of this system, which mainly corresponds to tidal tails and shells.

In order to design the GMOS spectroscopic mask, we used the false colour image shown in Figure 4.1 to select the bluest star-forming regions located across the field, mainly in the disk and tidal structures of our targets. We note that this selection criteria has been defined based on our goal of detecting young objects in general and emission line sources in particular. We observe four exposures of 1370 seconds each, using the grating R400. Observations were centered at 605 nm, 595 nm, 605 nm and 600 nm, with a slit width of 1.0 arcsec (given that most of our sources are point-like objects). The different central wavelengths were used to remove the gaps in the CCDs. The heights of the slits were changed depending on the source size, and also maximizing the number of objects in the mask design. The position angle of the observations was 135° for Arp 314. In Table 4.1 we list the coordinates of the slits located in the system Arp 314.

The use of the grating R400 allowed us to observe the main nebular emission lines

necessary to determine the oxygen abundances of these sources (e.g. Marino et al., 2013). The spectral coverage included H β , [OIII] 4959Å, [OIII] 5007Å, [NII] 6548 Å, H α , [NII] 6584Å emission lines for all observed sources. Depending on the position of the mask, for some regions it was also possible to observe H γ in the spectrum. CuAr arc lamps were observed after each science observation. Data reduction was performed using the GEMINI reduction package, in IRAF. Having in hand a suitable set of bias and flat fields, each frame was then corrected using the IRAF tasks GBIAS, GFLAT and GSREDUCE. Wavelength calibrations were done using the GSWAVELENGTH task. Continuum and sky emission lines were removed with the GSSKYSUB task. Finally, flux calibration was done by using the observations of the standard star LTT3218.

4.2.2 Fabry-Perot data

Gas flows have often been invoked as a mechanism to produce flattening of the metallicity gradients as a result of mixing of the metal distribution of interacting galaxies (e.g. Rupke et al. 2010a). In Section 4.4.7 we use H α Fabry-Perot data of Arp 314 to search for gas flows in this system. The goal is to then combine these results with those from the observed oxygen abundance analysis (derived in section 4.4.6) to investigate if there is a correspondence between gas flow and flat metallicity gradient for this specific system. Fabry-Perot data of Arp 314 covering the three members of Arp 314 with a spectral resolution of R=12600 was published in Torres-Flores et al. (2014a).

4.2.3 Complementary data

In order to complement the analysis presented in this Chapter, we have searched for medium infrared data of the main galaxies of Arp 314. We searched for data in the *Wide-Field Infrared Survey Explorer*, WISE (Wright et al. 2010) archive and in Table 4.2 we list the different magnitudes for each galaxy. The values listed in Table 4.2 correspond to the *wxgmag* value listed in the all-sky release source catalogue and these fluxes have been measured in elliptical apertures considering previous 2MASS detections. In the case of the *wxgmag* values, the *x* corresponds to the different filters available in WISE (W1, W2, W3 and W4). We note that we do not find WISE magnitudes for Arp 314-3. In addition, we have searched for ultraviolet (UV) GALEX data for Arp 314. The UV/GALEX data can trace star formation up to 200 Myrs, in comparison with the optical nebular emission as-

Table 4.2 *WISE* information for galaxies in Arp 314

ID	3.4 μ m mag	4.6 μ m mag	12 μ m mag	22 μ m mag
(1)	(2)	(3)	(4)	(5)
Arp 314-1	10.27 \pm 0.01	10.07 \pm 0.01	5.09 \pm 0.01	3.37 \pm 0.01
Arp 314-2	10.75 \pm 0.01	10.58 \pm 0.01	6.96 \pm 0.01	4.23 \pm 0.03
Arp 314-3	–	–	–	–

sociated with $H\alpha$, which traces current star formation. Arp 314 has been observed by this satellite and the general properties of its galaxies have been published by Muñoz-Mateos et al. (2007) and Gil de Paz et al. (2007).

4.3 Analysis

In this section we describe the analysis that we have performed on the Gemini/GMOS spectroscopic and ESO/T3.60m Fabry-Perot data of Arp 314.

4.3.1 Extinctions and flux measurements

Each spectrum of star-forming region has been corrected by Galactic and internal extinctions. We have used the Galactic extinction law suggested by Fitzpatrick (1999), assuming a colour excess of $E(B-V)=0.06$ (NED database). The internal extinction has been derived by comparing the observed and intrinsic Balmer line ratios between $H\alpha$ and $H\beta$. The observed fluxes of the $H\alpha$ and $H\beta$ emission lines were estimated with the routine `PAN`, in `IDL`, which allows us to fit a single Gaussian on each observed emission line profile. For the intrinsic Balmer decrement we assume a value of $H\alpha/H\beta=2.86$, for a electronic temperature of $T=10,000$ K and a electron density of $N_e=100$ cm $^{-3}$ (Osterbrock, 1989). This analysis allows us to obtain a gaseous colour excess $E(B-V)$ following Domínguez et al. (2013), which was converted into the colour excess of the stellar continuum ($E_\star(B-V)=0.44\times E(B-V)$, Calzetti et al. 2000). This colour excess ($E_\star(B-V)$) was used to correct each spectrum by internal extinction, by using Calzetti et al. (2000)'s extinction law, which was adopted taking into account the star-forming nature of our sources. As an example of the spectroscopic information, in the top and bottom panels of Figure 4.2 we show the GMOS optical spectra of two regions belonging to Arp 314-2 and Arp 314-3. On these panels we have labeled the most important emission lines that were identified in these spectra. Moreover, most of the faint emission lines were not identified

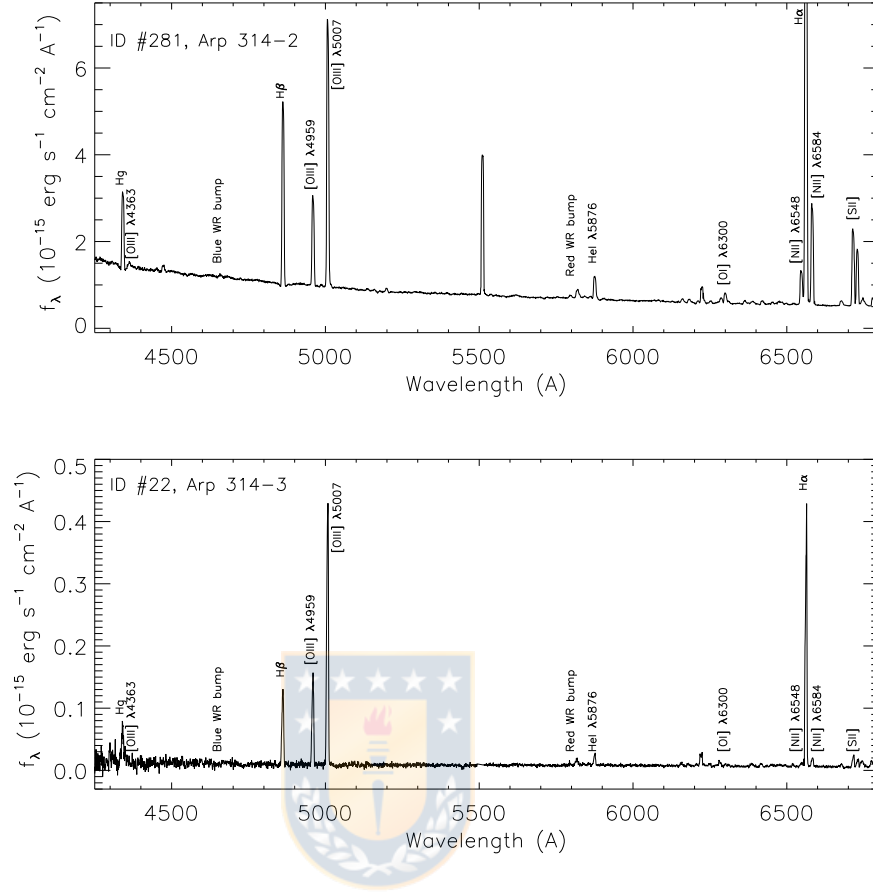


Figure 4.2 Spectra of two star-forming regions in Arp 314. *Top panel:* Spectrum of region #28_1, which corresponds to the brightest H α source in Arp 314-2. We do not show the entire flux axis, in order to display faint emission features. *Bottom panel:* Spectrum of the most intense star-forming region detected in Arp 314-3. The position of the main emission lines are labeled. Source: Torres-Flores et al. (2019)

in all the spectra available for Arp 314, as can be seen in the bottom panel of this Figure. For these reasons, our analysis will be based on the strongest emission lines (i. e. H β , [O III] 4959Å, [O III] 5007Å, [N II] 6548 Å, H α and [N II] 6584Å).

In the case of the slits located in the center of Arp 314-1, the strong stellar continuum emission, which displays absorption features, can affect the measurement of the emission line fluxes. In order to remove the contribution of the stellar continuum we have used the Penalized Pixel-Fitting (pPXF) method (Cappellari & Emsellem 2004) enabling us to estimate the stellar continuum emission. In order to do this, we have used the MILES stellar library (Sánchez-Blázquez et al. 2006), assuming a Salpeter IMF, ten ages ranging

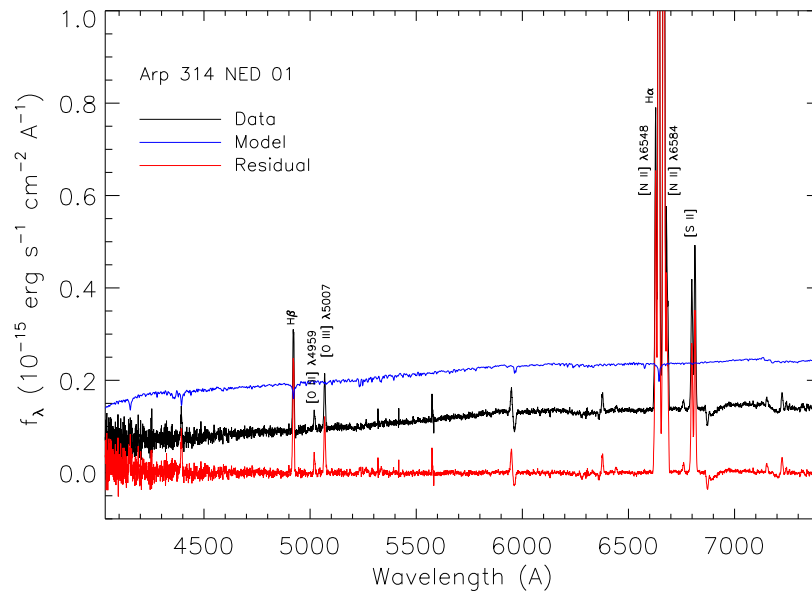


Figure 4.3 Observed spectrum of Arp 314-1 (black line). The stellar continuum derived from the pPXF analysis (blue line) is displaced by +0.1 in the y-axis to make it visible. The continuum-free spectrum is also displayed (red line) and the main emission lines are labeled. Source: Torres-Flores et al. (2019)

from 0.063 to 17.78 Gyr and six metallicities ranging from -1.71 to 0.22. Once the model was derived, we subtracted it from the observed data, in order to obtain a continuum free spectrum, which was used to measure the line fluxes. The results of this procedure are shown in Figure 4.3.

Emission line fluxes were measured on the extinction corrected spectra by using the routine `SPLIT` from `IRAF`. This routine allow us to fit a single Gaussian on each of the main nebular emission lines observed in the GMOS data, and also provides uncertainties for the fluxes measurements, which are computed by Monte-Carlo simulation. At the end, we measure the fluxes for the $H\beta$, $[O\text{III}]\lambda 4959\text{\AA}$, $[O\text{III}]\lambda 5007\text{\AA}$, $[N\text{II}]\lambda 6548\text{\AA}$, $H\alpha$ and $[N\text{II}]\lambda 6584\text{\AA}$ emission lines. These lines are typically used to derive oxygen abundances by using strong emission-line method, like the N2 (Storchi-Bergmann et al. 1994, Denicoló et al. 2002, Pettini & Pagel 2004) or the O3N2 (Stasińska, 2006) method. We did not detect the faint $[O\text{III}]\lambda 4363\text{\AA}$ emission line, which is usually used to determine oxygen abundances through the direct method, thus we use strong emission-line methods to derive gas-phase oxygen abundances as described below.

In order to confirm that the observed star-forming regions belong to the interacting systems, we have measured their radial velocities by using the task `EMSAO`, in `IRAF`. This routine correlates the observed spectra with a template which contains information for several emission lines. In the case of six regions (ID #23, #26, #33, #34, #28_2, and #28_4) the task `EMSAO` was not able to determine their radial velocities automatically. In these specific cases the radial velocity was estimated by using the observed wavelength of the $H\alpha$ emission line. The task `EMSAO` does not provide uncertainties in those cases.

4.3.2 Star formation rates and stellar masses

Studies have found that interacting galaxies may provide an enhancement in their star formation rates (e.g. Scudder et al., 2012). The effect of tidal encounters and mergers can trigger star formation bursts, as found in individual systems like the Antennae galaxies (e.g. Bastian et al., 2009). In order to quantify the effect of the interaction in the galaxies belonging to Arp 314, we have estimated the star formation rates (SFR) for individual regions and for the galaxies as a whole. Using the $H\alpha$ flux measured for each individual star-forming object, we have determined its SFR by using the standard recipe given in Kennicutt (1998) ($\text{SFR} = 7.9 \times 10^{-42} L(H\alpha) \text{ erg s}^{-1}$), under the assumption of a continuous star formation process.

SFRs for Arp 314-2 and Arp 314-3 have been computed using three different methods. Firstly, from their $H\alpha$ fluxes (Fabry-Perot) by using the recipe proposed by Kennicutt (1998). It is important to note that the $H\alpha$ fluxes published by Torres-Flores et al. (2014a) were not corrected by internal extinction, given that these measurements come from the $H\alpha$ (Fabry-Perot) emission line and no bluer emission lines, like $H\beta$, were available. Secondly, using the *WISE* data and the calibrations derived for Wen et al. (2014) and Cluver et al. (2014). *WISE* magnitudes were converted into spectral luminosities νL_ν considering the corresponding distances. Details about conversion between *WISE* luminosities (e.g. in-band and spectral luminosities) can be found in Jarrett et al. (2013) and Cluver et al. (2014). Thirdly, SFRs were also estimated by using their *GALEX* far ultraviolet (FUV) magnitudes published by Gil de Paz et al. (2007) and Muñoz-Mateos et al. (2007). Magnitudes were corrected by internal extinctions (A_{FUV}) and converted in SFRs by using the A_{FUV} values and calibrations given in Muñoz-Mateos et al. (2007), and considering the distance to each galaxy.

In addition, a number of authors have found that a combination of $H\alpha$ and mid-infrared

luminosities (MIR) can provide a good estimation of the total star formation in a galaxy (e. g. Calzetti et al. 2007, Smith et al. 2007). In this sense, the infrared data provide information of obscured star formation and the optical $H\alpha$ emission gives direct information of the current star formation. Wen et al. (2014) provide new calibrations to estimate the total star formation rates, by using $H\alpha$ and MIR *WISE* emission. Then, we have used equation 17 in Wen et al. (2014) to compute the total SFR for Arp 314-2, where the $H\alpha$ emission comes from the Fabry-Perot data (Torres-Flores et al., 2014a). This estimation is nevertheless not valid for Arp 314-1, given its AGN nature (as shown in section 4.4.4), and is not feasible for Arp 314-3, because no *WISE* magnitudes are available.

Stellar masses for galaxies can be estimated by using their near infrared luminosities, given that these wavelengths are less affected by extinction and they trace the bulk of the stellar emission. The main uncertainty in this case is the assumption of a mass-to-light ratio. Several authors have derived calibrations to estimate this parameter (e.g. Bell & de Jong, 2001; Bell et al., 2003). Given the current available data, we have used the *WISE* W1 fluxes ($3.4\mu\text{m}$) to estimate the stellar masses of our targets. In order to derive the masses, we have used the calibration proposed by Cluver et al. (2014) (equation 1), which involves the use of the colour (W1-W2) and the W1 luminosity.

4.3.3 Gas-phase oxygen abundances

The determination of chemical abundances through the direct method will depend on the detection of auroral emission lines (e.g. $[\text{OIII}] 4363\lambda$), which typically have low intensities. In addition, these lines are typically found in low metallicity environments. For all sources observed in Arp 314, except for ID#28_1, it was not possible to measure the $[\text{OIII}] 4363\lambda$ line (we detect a weak contribution of the $[\text{OIII}] 4363\lambda$ emission line in the region ID#28_1, see top panel of Figure 4.2). For this reason, oxygen abundances were estimated by strong line methods. In the literature there exists several empirical methods to determine chemical abundances. For instance, the N2 calibrator (Storchi-Bergmann et al. 1994, Denicoló et al. 2002) involves the use of the $H\alpha$ and the $[\text{NII}] 6584\lambda$ emission lines, and therefore it does not depend strongly in the reddening correction. However, no oxygen lines are used in the determination of chemical abundances. On the other hand, the O3N2 method (see Pettini & Pagel 2004) involves the $[\text{OIII}] 5007\lambda$ emission line, besides the $H\beta$, $H\alpha$ and $[\text{N}] 6584\lambda$ lines. Marino et al. (2013) recommended this method in the high-metallicity regime. Those authors have also included new direct abundance

measurements in the calibration that makes the estimation more relevant and suggest the use of this calibrator for regions that display an O3N2 value ranging from -1.1 to 1.7. Given that the spectra of our targets cover the whole optical regime, from blue to red, we have used the O3N2 method and thus the prescription given by Marino et al. (2013) to determine oxygen abundances. It is worth noting that the empirical calibration methods display large uncertainties (~ 0.2 dex), which are associated with the proper scatter of the calibrator. Also, the use of different methods can give us different estimates for the oxygen abundances. However, when a single calibrator is used for a given sample, we can have a reliable determination of the metallicity distribution (see Scarano et al. 2011, Bresolin et al. 2012). This is important for this kind of studies, where metallicity distributions are studied. In this context, our final measurements include the uncertainties of 0.2 dex derived from the scatter of the calibrators, however, the actual uncertainties arises from the flux estimates.

4.4 Results

4.4.1 Inspecting the optical morphology of galaxies in Arp 314

Using the Gemini optical imaging data we have inspected the morphology of each galaxy belonging to Arp 314 (see Figure 4.1). We describe hereafter the main morphological features of the interacting system. Galaxy Arp 314-1 displays a spiral-arm structure with several bright blue knots clearly associated with star-forming regions. The nucleus is dominated by a strong point-like emission. The outskirts of the galaxy display a diffuse stellar emission in the shape of a shell-like structure. Given their proximity, these shells should be formed by an interaction of Arp 314-1 with Arp 314-2 as seen in simulations of interacting galaxies. For instance, Hernquist & Quinn (1989) suggested that shell structures can be formed during the interaction of a low-mass disk galaxy with a more massive disk galaxy. Galaxy Arp 314-2 displays an extremely perturbed morphology (see Figure 4.1), with no spiral pattern being detected. Shell-like structures also emerge in this case. Three bright knots can be observed in its centre, with a diffuse stellar emission to the Northwest of these regions. Several star-forming regions can be observed across the main body of this object. Between Arp 314-1 and Arp 314-2 we observe a diffuse and faint stellar emission which seems to connect both galaxies. A chain of compact sources is also

observed in this region. On the Southeast side of Arp 314-2, there is an extended optical tidal tail containing a number of compact knots. Finally, Arp 314-3 displays an irregular shape. Its morphology reveals the presence of a stellar bar surrounded by more than a dozen star-forming regions. The morphology of this galaxy resembles that of the Large Magellanic Cloud. Elmegreen et al. (1993) catalogued Arp 314 as a “Multiple galaxy system with dwarf galaxy-like debris” (Table 2 in that paper).

4.4.2 Internal extinctions, radial velocities and line fluxes

In the fourth column of Table 4.1 we list colour excesses estimated as described in Section 4.3, with the exception of the central spectrum of Arp314-1, given its possible AGN nature (see Section 4.4.4). The values of colour excess span from $E(B-V)_* \sim 0$ to $E(B-V)_* \sim 0.63$ (the latter value corresponds to ~ 2.0 mag in the V-band, considering $R_V=3.1$). These values are consistent with the estimates derived for star-forming regions located in other interacting systems. In the last column of Table 4.1 we list the radial velocities derived for each region, confirming their membership to their parent galaxies.

In Table 4.3 we list the flux of the $H\beta$, $[OIII] 4959\text{\AA}$, $[OIII] 5007\text{\AA}$, $[NII] 6548\text{\AA}$, $H\alpha$, $[NII] 6584\text{\AA}$ emission lines for the different star-forming regions observed in Arp 314, where the most intense sources are associated with the nucleus of Arp 314-1 and with a strong star-forming object located in Arp 314-2. The physical parameters presented in the following sections have been derived from the fluxes listed in Table 4.3.

4.4.3 $H\alpha$ luminosities: From typical HII regions to giant HII region candidates

Considering the distance to Arp 314, we have derived the dust-corrected $H\alpha$ luminosities for the star-forming complexes (Table 4.3, column 9). Inspecting these values, we found objects with $H\alpha$ luminosities larger than some known Giant HII regions. In the case of Arp 314-2, the central regions #28_1 and #28_4 display $H\alpha$ luminosities larger than $\log(L_{H\alpha}) > 40$ erg s^{-1} . In addition, region #33 also displays high $H\alpha$ luminosity, with a $\log(L_{H\alpha})$ almost equal to 40 erg s^{-1} . We have located these sources on the dispersion velocity map of Arp 314 published by Torres-Flores et al. (2014a) and we found that these objects display a large velocity dispersion of $\sigma \sim 35-40$ km s^{-1} . Similar values have been measured for several giant HII regions (GHII R) located in other nearby galaxies

Table 4.3 Line fluxes for the star-forming regions located in the tidal tail and main body of Arp 314

ID	H β	[OIII] λ 4959	[OIII] λ 5007 10^{-15} erg cm $^{-2}$ s $^{-1}$ \AA^{-1}	[NII] λ 6548	H α	[NII] λ 6584	12+log(O/H)	L $_{H\alpha}$ erg s $^{-1}$	SFR 10^{-3} M $_{\odot}$ yr $^{-1}$
(1)	(2)	(3)	(4)	(5)	(6)	(7)	(8)	(9)	(10)
1	0.11 \pm 0.07	0.17 \pm 0.01	0.33 \pm 0.01	0.01 \pm 0.01	0.23 \pm 0.01	0.01 \pm 0.01	8.12 \pm 0.22	37.85	0.60
3	0.32 \pm 0.02	0.39 \pm 0.02	0.86 \pm 0.01	0.02 \pm 0.01	0.64 \pm 0.01	0.01 \pm 0.01	<8.1	38.30	1.60
20	0.24 \pm 0.01	0.19 \pm 0.01	0.40 \pm 0.01	0.02 \pm 0.01	0.25 \pm 0.01	0.01 \pm 0.01	8.11 \pm 0.21	37.90	0.60
21	0.20 \pm 0.03	0.02 \pm 0.01	0.45 \pm 0.03	0.00 \pm 0.00	0.58 \pm 0.03	0.02 \pm 0.01	8.13 \pm 0.20	38.26	1.40
22	0.88 \pm 0.01	1.04 \pm 0.01	2.92 \pm 0.01	0.03 \pm 0.01	2.36 \pm 0.01	0.11 \pm 0.01	8.14 \pm 0.18	38.87	5.80
23	0.45 \pm 0.06	0.32 \pm 0.04	2.62 \pm 0.08	0.03 \pm 0.05	2.12 \pm 0.07	0.02 \pm 0.02	<8.1	38.82	5.20
24	0.26 \pm 0.01	0.09 \pm 0.01	0.17 \pm 0.01	0.00 \pm 0.00	0.61 \pm 0.01	0.06 \pm 0.01	8.35 \pm 0.18	38.28	1.50
26	2.23 \pm 0.02	3.75 \pm 0.01	10.65 \pm 0.02	0.09 \pm 0.03	6.95 \pm 0.02	0.24 \pm 0.02	<8.1	39.34	17.10
33	6.67 \pm 0.07	1.41 \pm 0.06	4.17 \pm 0.06	2.24 \pm 0.06	24.21 \pm 0.06	6.83 \pm 0.06	8.46 \pm 0.18	39.88	59.80
34	0.64 \pm 0.21	0.11 \pm 0.04	1.07 \pm 0.12	0.54 \pm 0.09	5.08 \pm 0.07	1.30 \pm 0.08	8.36 \pm 0.18	39.20	12.50
38	0.71 \pm 0.07	0.19 \pm 0.03	0.78 \pm 0.03	0.30 \pm 0.05	3.08 \pm 0.04	1.03 \pm 0.05	8.42 \pm 0.18	38.98	7.60
42	22.83 \pm 0.24	2.95 \pm 0.27	10.63 \pm 0.24	28.72 \pm 0.22	132.06 \pm 0.23	93.73 \pm 0.39	-	40.62	-
43	0.22 \pm 0.01	0.25 \pm 0.01	0.57 \pm 0.01	0.01 \pm 0.00	0.35 \pm 0.01	0.04 \pm 0.01	8.24 \pm 0.18	38.04	0.90
44	0.53 \pm 0.01	0.18 \pm 0.01	0.47 \pm 0.01	0.22 \pm 0.01	1.38 \pm 0.01	0.40 \pm 0.01	8.43 \pm 0.18	38.63	3.40
46	0.76 \pm 0.01	0.18 \pm 0.01	0.39 \pm 0.01	0.26 \pm 0.01	2.22 \pm 0.01	0.75 \pm 0.01	8.49 \pm 0.18	38.84	5.50
47	1.86 \pm 0.02	0.88 \pm 0.03	2.21 \pm 0.03	0.50 \pm 0.03	5.98 \pm 0.03	1.44 \pm 0.03	8.38 \pm 0.18	39.27	14.80
48	0.22 \pm 0.02	0.13 \pm 0.01	0.51 \pm 0.01	0.10 \pm 0.01	1.16 \pm 0.01	0.28 \pm 0.01	8.32 \pm 0.18	38.56	2.90
56	0.53 \pm 0.01	0.15 \pm 0.01	0.39 \pm 0.01	0.17 \pm 0.02	1.42 \pm 0.02	0.44 \pm 0.01	8.45 \pm 0.18	38.65	3.50
58	0.14 \pm 0.01	0.03 \pm 0.01	0.30 \pm 0.01	0.03 \pm 0.01	0.45 \pm 0.01	0.12 \pm 0.01	8.34 \pm 0.18	38.15	1.10
28_1	33.91 \pm 0.04	17.13 \pm 0.05	48.07 \pm 0.05	6.30 \pm 0.04	112.52 \pm 0.04	18.95 \pm 0.04	8.34 \pm 0.18	40.55	277.70
28_2	3.46 \pm 0.03	1.85 \pm 0.03	5.29 \pm 0.03	0.86 \pm 0.04	8.92 \pm 0.03	2.37 \pm 0.03	8.37 \pm 0.18	39.44	22.00
28_4	10.67 \pm 0.03	6.02 \pm 0.03	17.42 \pm 0.03	2.29 \pm 0.04	33.42 \pm 0.03	4.80 \pm 0.03	8.31 \pm 0.18	40.02	82.50

(e.g. Firpo et al., 2010), suggesting that these star-forming regions detected in Arp 314 are GHnR candidates. These kind of strong H α emitting sources have been found in several other interacting systems. For example, Miralles-Caballero et al. (2012) studied the properties of several extranuclear H α complexes located in a sample of low-redshift ultra luminous infrared galaxies. These authors found that their sample present similar properties to extragalactic HII regions and tidal dwarf galaxies that are found in mergers and compact groups of galaxies. This may also be the case for the strong H α sources located in Arp 314. Future studies on these regions are necessary in order to understand the effect of the stellar and supernova feedback on their environment. Higher resolution imaging achieved using space facilities or ground based adaptive optics is also needed to eventually resolve multiple HII regions possibly embedded in non-resolved clumps.

4.4.4 Ionization mechanism and AGN activity

We have analyzed the ionization mechanisms (massive stars versus shocks, e.g. Konstantopoulos et al. 2014a for HCG 92) of the star-forming regions listed in Table 4.3. In addition, using the available data, we investigated the ionization mechanism of the nuclear region of the main galaxies of this group and the presence of an active galactic nuclei. In order to determine the ionization mechanism for the sources, we plot their [NII]/H α versus [OIII]/H β emission line ratios (Figure 4.4), following the classic diagnostic diagram

proposed by Baldwin et al. (1981), which is commonly known as BPT diagram. In the top panel of Figure 4.4 the solid and dashed lines represent the limits between star-forming regions and AGN galaxies, which were suggested by Kauffmann et al. (2003) and Kewley et al. (2001), respectively.

Inspecting the top panel of Figure 4.4 we found that most of the sources observed in Arp 314 are located in the star-forming locus, confirming their nature, i.e., these sources are being ionized by massive stars. However, there is one source that lies off the star-forming domain: the nucleus of Arp 314-1 (region #42). Considering the limits given by Kauffmann et al. (2003) and Kewley et al. (2001), and the criteria suggested by Kewley et al. (2006), Arp 314-1 is a *composite galaxy* in the BPT diagram. The spectra of composite galaxies should be the result of a combination of star formation and AGN activity. However, recent studies have found that “composite objects” could be the result of star formation plus shocks (Rich et al., 2015), or even star formation plus ionization produced by low-mass evolved stars (Belfiore et al., 2016).

In order to elucidate the nature of the nuclear region of Arp 314-1, we have compared their $H\alpha$ equivalent width versus their $[NII]/H\alpha$ ratio (as proposed by Cid Fernandes et al., 2011). This diagram is shown in the bottom panel of Figure 4.4. SF, sAGN, wAGN and RG means star-forming, strong AGN weak AGN and “retired galaxies”. Arp 314-1 lies in the strong AGN location, however, the BPT diagram classifies it as a transition object. Considering both diagrams, we suggest that there is a real AGN contribution in the central region of Arp 314-1. In addition, we can not exclude that star formation may play an important role in the nuclear region of this galaxy as well.

4.4.5 Star formation rates

Individual star-forming regions

In the last column of Table 4.3 we list the $SFR(H\alpha)$ for each individual source observed in Arp 314, under the assumption of a continuous star formation process. In general, individual regions display modest level of ongoing star formation. A few exceptions can be found in Arp 314-2. For instance, region #28_1, displays a relatively high $SFR \sim 0.28 M_{\odot} \text{ yr}^{-1}$. This region corresponds to a burst of star formation located outside the nuclear region of this galaxy. On the other hand, regions #1, #3, and #43 display the lower values for the SFRs ($\sim 10^{-3} M_{\odot} \text{ yr}^{-1}$). The case of region #43 is peculiar. This source is located

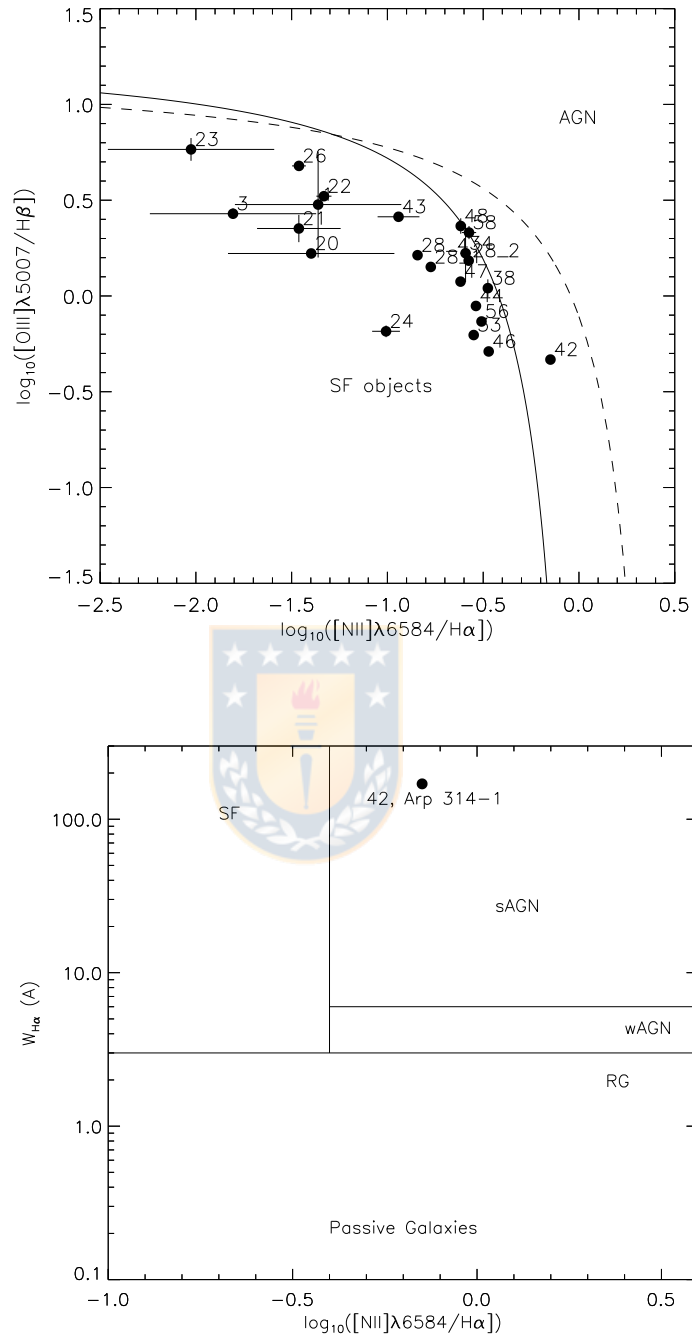


Figure 4.4 Emission line diagnostic diagram for the regions observed in Arp 314. *Top panel:* BPT diagnostic diagram proposed by Baldwin et al. (1981). The solid line represents the limit between photoionized star-forming objects and AGN galaxies, which was suggested by Kauffmann et al. (2003) and the dashed black line indicate the same limit defined by Kewley et al. (2001). *Bottom panel:* WHAN diagnostic diagram proposed by Cid Fernandes et al. (2011), on which we have included the data point for the central region of Arp 314-1. Source: Torres-Flores et al. (2019)

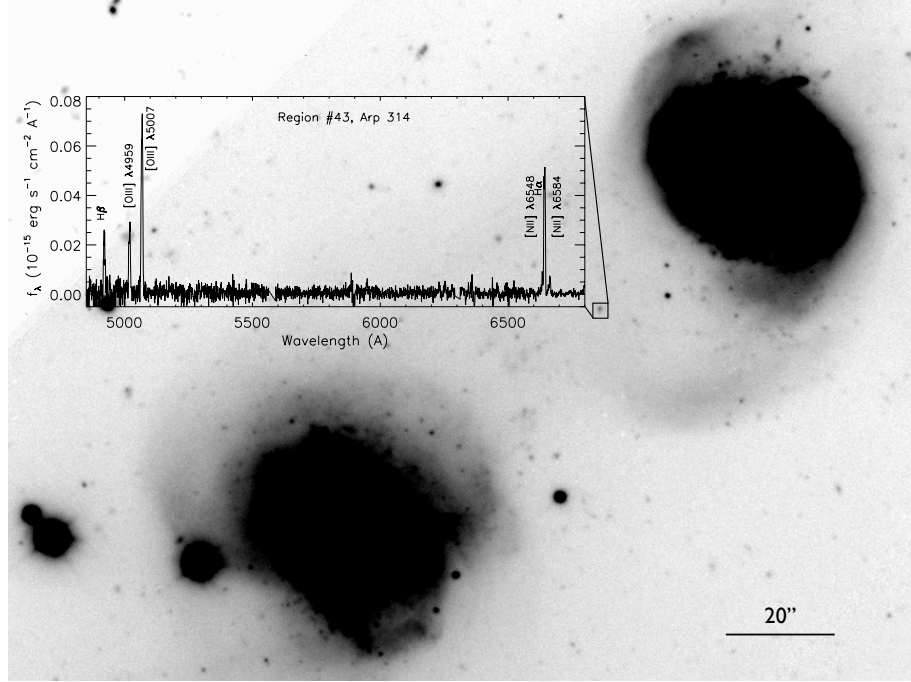


Figure 4.5 Gemini/GMOS r' -band image of Arp 314-1 and Arp 314-2. On this image we show the location and spectrum of the region ID #43, which is located in the bridge that connects the main galaxies of this system. Source: Torres-Flores et al. (2019)

in the bridge that connects Arp 314-1 with Arp 314-2, as can be seen in Figure 4.5, suggesting that this source was formed from gaseous material that was ejected during the interaction process.

Global estimates: UV, $H\alpha$ and MIR data

In Table 4.4 we list the SFRs estimated from the UV, $H\alpha$, MIR and $H\alpha$ corrected by MIR emission for the main galaxies of Arp 314. Indeed, in the case of Arp 314-1, no computation was performed given its possible AGN nature.

The galaxy Arp 314-2 displays $SFR_{FUV}=1.1 M_{\odot} \text{ yr}^{-1}$, $SFR(H\alpha)=1.3 M_{\odot} \text{ yr}^{-1}$, $SFR_{22\mu m}=1.9 M_{\odot} \text{ yr}^{-1}$ and $SFR_{H\alpha_{obs}+22\mu m}=2.1, M_{\odot} \text{ yr}^{-1}$.

In the case of Arp 314-3, we just compute the SFR using the $H\alpha$ emission, obtaining a value of $SFR(H\alpha)=0.2 M_{\odot} \text{ yr}^{-1}$ (no FUV magnitude was found in the *GALEX* archive for this galaxy).

Stellar masses are tabulated Table 4.4 (column 6), including the galaxy Arp 314-1, given that the stellar mass is mainly derived from the stellar emission, W1, which should

Table 4.4 Star formation rates, stellar masses and specific star formation rates

ID	SFR _{FUV} M _⊙ yr ⁻¹	SFR _{Hα} M _⊙ yr ⁻¹	SFR _{22μm} M _⊙ yr ⁻¹	SFR _{Hα+22μm} M _⊙ yr ⁻¹	log(M _★)	log(SFR _{Hα+22μm} /M _★)
(1)	(2)	(3)	(4)	(5)	(6)	(7)
Arp 314-1	–	–	–	–	9.94	–
Arp 314-2	1.1	1.3	1.9/1.8	2.1	9.81	-9.48
Arp 314-3	–	0.2	–	–	–	–

not strongly be affected by AGN activity.

Considering the M_{\star} values, and the SFRs, we estimate the specific SFR (sSFR) for Arp 314-2, value that is listed in the last column of Table 4.4. Its sSFR shows that Arp 314-2 ($\log(\text{SFR}_{H\alpha+22\mu\text{m}}/M_{\star})=-9.48 \text{ yr}^{-1}$) lies in the star-forming sequence in the mass versus sSFR diagram shown by Schiminovich et al. (2007). Considering its mass, this galaxy is actively forming stars. We could not compute the sSFR for Arp 314-1 and Arp 314-3.

4.4.6 Gas-phase oxygen abundances

Diluted metallicities in Arp 314

In the case of the star-forming complexes observed in Arp 314-1 and Arp 314-2 we measured oxygen abundances $12+\log(\text{O}/\text{H})$ which range from 8.24 to 8.49. All these oxygen abundances are sub-solar (considering a solar oxygen abundance of $12+\log(\text{O}/\text{H})_{\odot}=8.72$, Allende Prieto et al. 2001). Considering the B-band absolute magnitude of Arp 314-1 and Arp 314-2, which corresponds to $M_B=-20.62$ and $M_B=-20.28$ respectively (HyperLeda database), we found that both galaxies lie off the B-band metallicity-luminosity relation studied by Kewley et al. (2006). However, we note that the B-band luminosity of these galaxies should be affected by the star formation episodes that are taking place in these galaxies. In order to check it, we have used the stellar mass of these galaxies to determine their location in the mass-metallicity relation studied by Tremonti et al. (2004). Using the masses listed in Table 4.4 (column 6), we found that Arp 314-1 and 314-2 display slightly lower oxygen abundances for their respective stellar masses. A similar scenario has been found in different interacting systems. In fact, Kewley et al. (2006) suggest that gas inflows dilute the central metallicities of interacting galaxies. More recently, Olave-Rojas et al. (2015) suggest that this mechanism is producing the observed metallicity gradient in NGC 6845A, galaxy that belongs to the group NGC 6845.

In the case of Arp 314-3, three of their star-forming regions display O3N2 values that are higher than the limits given by Marino et al. (2013) for using this method. This implies that these regions belonging to Arp 314-3 have oxygen abundances lower than $12+\log(\text{O}/\text{H})_{\odot}=8.10$. In addition, we did not find *WISE* information for this galaxy, therefore, its mass was not computed. In view of these facts, we can not locate this object in the mass-metallicity relation. However, some speculations can be done regarding its origin. Arp 314-3 displays a LMC-like morphology, it could be a pristine irregular dwarf or a Tidal Dwarf Galaxy (TDG). If Arp 314-3 was formed from pre-enriched material belonging to Arp314-1 or/and -2, it should show an oxygen abundance similar to these two galaxies. The oxygen abundance of Arp 314-3 measured with the O3N2 index indicates a metallicity of $12+\log(\text{O}/\text{H})=8.14$, which is lower than the one of Arp 314-1 and Arp 314-2, respectively $12+\log(\text{O}/\text{H})=8.39$ and $12+\log(\text{O}/\text{H})=8.34$. This suggests that Arp 314-3 is a primordial dwarf irregular and not a TDG formed from the interaction of the two main galaxies of the group. This scenario is also supported by the metallicity-luminosity relation studied by Weilbacher et al. (2003), who included in their analysis a sample of TDG candidates. Indeed, considering its B-band absolute magnitude, $M_B=-14.89$ (HyperLeda database), Arp 314-3 does not lie in the locus of the TDGs.

Flat metal distribution in interacting systems

Using the measured oxygen abundances we have derived the oxygen abundance distribution for the galaxy Arp 314-1, which is shown in Figure 4.6. Distances have been de-projected by using the kinematical inclination and position angle published in Torres-Flores et al. (2014a), and using the procedure developed by Scarano et al. (2008). On this figure, the solid line represents a linear fit on the data, where we have excluded the nuclear region (region #42), given the contribution of an AGN in the spectra. On the same plot, we have included the oxygen abundances of regions belonging to Arp 314-2 (empty circles). In this latter case, distances correspond to linear projected distances estimated from the centre of Arp 314-1 to each source. Regions belonging to Arp 314-2 were not included in the fit shown. From the linear fit we derive a zero point of $\alpha=8.48\pm 0.04$ and a slope of $\beta=-0.02\pm 0.01$ dex kpc^{-1} , which is shallower than the slope displayed by non-interacting galaxies (e. g. Zaritsky et al. 1994). Inspecting Figure 4.6 we note that most of the star-forming regions for which we measure oxygen abundances are located at radius $R<5$ kpc. These star-forming objects do not display a clear oxygen abundance

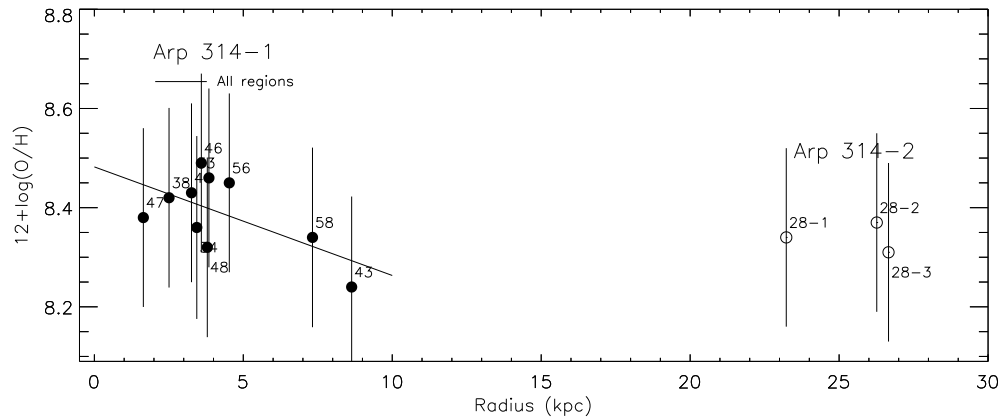


Figure 4.6 Oxygen abundance gradient for Arp 314-1, where different regions are shown by filled black circles. A linear fit on the data is indicated by a black line. Regions belonging to Arp 314-2 are included on the plot (empty circles), in order to show the differences in the oxygen abundances. Source: Torres-Flores et al. (2019)

gradient. Indeed, the reported gradient arises when we include regions #58 and # 43 in the fit. These objects are located in the outskirts of Arp 314-1, therefore, are expected to have lower oxygen abundances.

It is important to note that galaxy Arp 314-3 displays a low oxygen abundance, consistent with its luminosity. Nordgren et al. (1997) published the H I distribution of Arp 314 showing a large cloud of H I covering the three main galaxies. If gas flows/gas mixing are responsible for the flattening of metallicity gradients in interacting systems, it is puzzling that metals have not mixed yet.

4.4.7 Kinematics: Searching for gas motions

The kinematics of the members of Arp 314 has been already analyzed by Torres-Flores et al. (2014a), however, no detailed analyses of the non-circular motions and of the multiple H α emission components were done. We will use this information, combined with the Gemini spectroscopic analysis, to understand the observed metal distribution of Arp 314. In Figure 4.7 we show the r' -band optical images (top panels), the velocity fields (second to fourth panels) and the residual velocity fields (fifth panel) for Arp 314-1, Arp 314-2 and Arp 314-3 (left, middle and right row, respectively). Here the fourth rows represent the observed and modelled velocity field, where the model was derived from the rotation curve derivation (see Torres-Flores et al. 2014a, Epinat et al. 2008). The H α emission

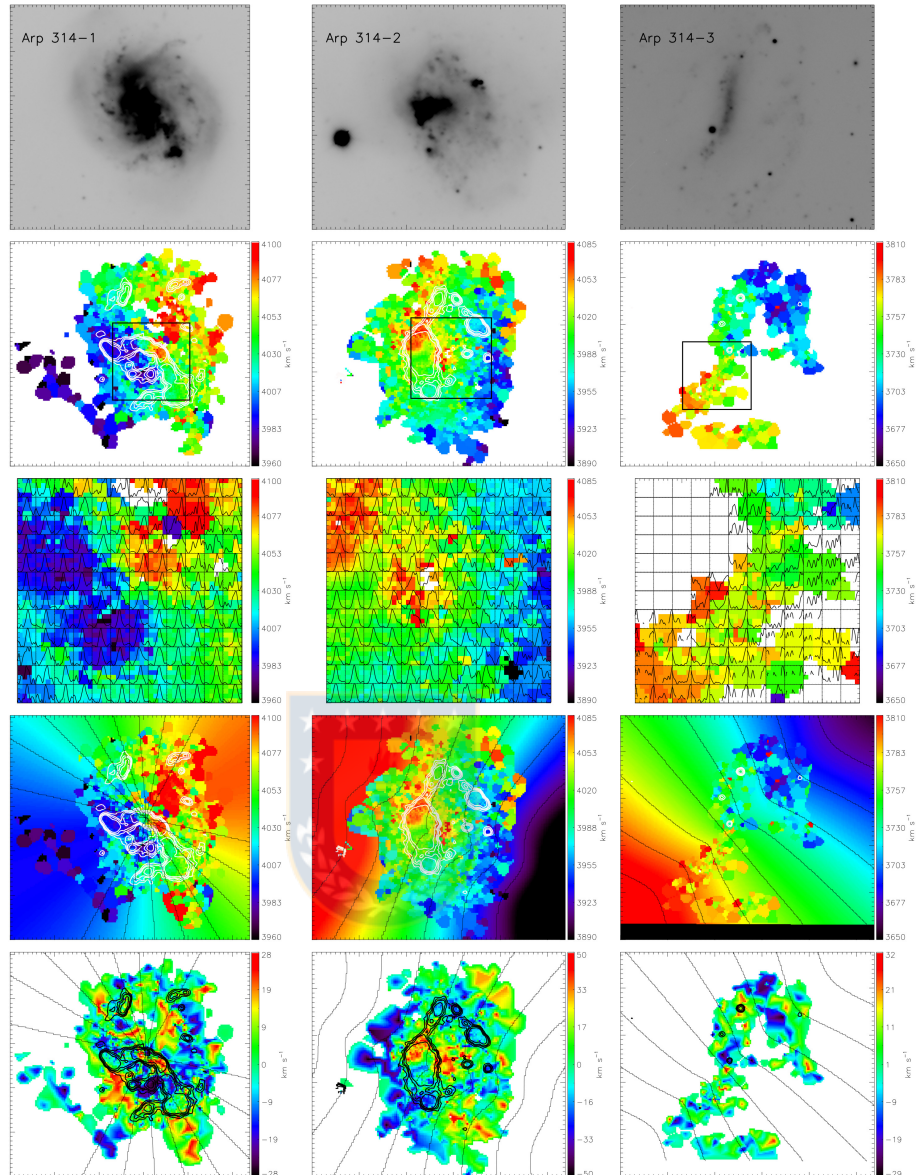


Figure 4.7 Images and velocity fields for Arp 314. Arp 314-1 (left row), Arp 314-2 (middle row) and Arp 314-3 (right row). The first line displays Gemini r-band images. The second line shows the observed color-coded velocity fields on which some bright H α contours have been over-plotted in white. The third line is a zoom of the square drawn in the second line onto which the H α profiles observed in the central regions have been over-plotted (using a bin 4 pix \times 4 pix). For clarity, the intensity of the H α profiles have been normalised to unity. The fourth line shows the observed color velocity fields onto which the 2D model built from the rotation curves published by Torres-Flores et al. 2014a have been over-plotted. The model is visualised using black iso-velocities and color ones when no data are available. The fifth line displays the residual velocity fields, i.e. the difference between the data and the model plotted in the fourth line; for clarity the iso-velocities and the H α isocontours have been replotted. Source: Torres-Flores et al. (2019)

contours and $H\alpha$ profiles have been superimposed (respectively, in the second and third lines). The velocity fields and the residual velocity fields clearly indicate that the three galaxies are far from being pure rotating disks.

In the case of the Sbc galaxy Arp 314-1, Torres-Flores et al. (2014a) reported a relatively regular velocity field. However, they found a misalignment between the morphological and kinematic position angle (33° and 115° , respectively), which is a typical signature of galaxy interaction. Despite the fact that the galaxy is globally rotating, when we compare the model and the observed velocity fields (Figure 4.7 left column, fourth row), we observe strong local velocity jumps (for instance in the outskirts of the disk, where the data show larger velocity amplitude than the model). These strong kinematical perturbations are clearly visible on the residual velocity field (Figure 4.7 left column, last row) that shows non-circular motions randomly distributed in the disk, ranging between -25 to $+25$ km s^{-1} . These kinds of features can contain rich information related with the interaction history of the galaxies, specially in closely face-on systems (e.g Gómez et al. 2019, submitted). Inspecting the $H\alpha$ profiles of Arp 314-1, we mostly found a strong emission line very often accompanied by a second component, which is fainter in intensity. The fainter emission line is either resolved or embedded in an asymmetric profile dominated by the brighter emission line. This may suggest that Arp 314-1 has experienced a recent gas accretion, as has been reported in other interacting systems (e.g. Font et al. 2011). In addition, the slope of the metallicity gradient observed in Arp 314-1 ($\beta = -0.02 \pm 0.01$ dex kpc^{-1}) is consistent with the slope measured in the metal distribution of galaxy pairs (Kewley et al. 2010). Kewley et al. (2010) suggest that the flattening in the metal distribution of galaxy pairs should be connected with large gas inflows. Given the modest intensity of the second component versus the main one, the gas flow we observe inspecting the $H\alpha$ profiles of Arp 314-1 is probably not carrying out large quantities of material. If gas inflows were the main mechanism in producing a flattening in the metal distribution of Arp 314-1, these inflows should have already occurred and we would then expect that presently the process has already finished or it is at its final phase.

The scenario is even more complicated for the SBc galaxy Arp 314-2. The external region of this galaxy displays a complex velocity field which does not actually show a well-behaved rotating disk (see Fig. 4.7, central column). The dip in the blue-shifted and the bump in the redshifted inner rotation curve (Torres-Flores et al., 2014a), likely due to the strong bar, provide a peculiar pattern for the central isovelocities over-plotted on top

of the observed velocity field which does not follow a symmetric rotating disk pattern. Indeed, if we observe a continuity between the data and the model on the blueshifted side of the galaxy, this is not the case on the redshifted side. This can be seen on the very asymmetric residual velocity field showing a blueshift side almost flat, but a redshifted side with velocities which jump from -50 to $+50$ km s^{-1} within a couple of kpc. In fact, these velocities display a ring-like structure. The $\text{H}\alpha$ profiles of the central region of this galaxy display asymmetric profiles. This suggests that more than one kinematic component is present in this region, resulting in broad $\text{H}\alpha$ emission line profiles. Towards the northern region of the nucleus of Arp 314-2 we even detect double $\text{H}\alpha$ profiles (as can be seen in Fig. 4.7). Given the complex kinematic of this system, it is difficult to determine if these double-component profiles arise from a gas inflow. In any case, this galaxy displays a $\text{SFR}(\text{H}\alpha) \sim 1.1 M_{\odot} \text{ yr}^{-1}$, which suggests that no external gas accretion is dramatically increasing its SFR. However, the central region of this galaxy, where the $\text{H}\alpha$ emission peaks (inner $5'' \times 5''$ centred in R.A.: 22:58:07.94, Dec: -3:47:19.10), displays velocity dispersions of ~ 40 km s^{-1} . Those values are larger than the typical values for the velocity dispersion displayed by non-interacting systems (~ 25 km s^{-1} , Epinat et al., 2010, for the GHASP survey). Given that there is a spatial correlation between the maximum of the $\text{H}\alpha$ emission and the maximum velocity dispersion in the central region of Arp 314-2, we can not exclude that the stellar feedback produced by star formation is increasing the interstellar medium velocity dispersion.

Finally, the kinematic of the irregular SBd dwarf galaxy Arp 314-3 displays, despite its bar, a fairly symmetric rotation disk pattern (Torres-Flores et al., 2014a) of low maximum rotation velocity ~ 40 km s^{-1} at the optical radius and growing up to ~ 60 km s^{-1} at two optical radii. These authors suggest that this object could be an irregular star-forming galaxy or an object formed from tidal debris. The low observed oxygen abundances confirm the first scenario: Arp 314-3 is a primordial irregular galaxy, as discussed in session 4.4.6.

4.5 Discussion

4.5.1 Discovering the unexplored interacting system Arp 314

Despite its spectacular morphology, the interacting system Arp 314 has not been studied in detail in the past. Garcia (1995) classified it as a compact group. Nordgren et al. (1997) studied the H α content in this system. H α tails, produced by tidal interaction, are dynamically fragile and have furthermore a limited live time (Hibbard et al., 2000), thus a classification based on the H α distribution, morphology, content and kinematics in groups of galaxies indicate the stage of group evolution. Following Verdes-Montenegro et al. (2001), Arp 314 is at beginning of stage 2.0, the H α is still rather concentrated on the individual galaxies but characteristic tidal tails are in process of formation. Based on their H α kinematic information, Nordgren et al. (1997) suggest that Arp 314-1 is in a direct encounter with Arp 314-2, while Arp 314-2 is in a retrograde encounter with Arp 314-1. These authors also suggest that Arp 314-3 seems to be in a direct encounter with the main galaxies of this system. In addition, they found that the H α emission in Arp 314 encompass the three members in a large common gaseous cloud. Some gaseous tidal structures were also reported for these authors, which are typical signatures of galaxy-galaxy interactions.

The gaseous features described by Nordgren et al. (1997) are consistent with the optical appearance of Arp 314. Using Gemini optical imaging we report the existence of a faint stellar bridge that connects Arp 314-1 with Arp 314-2 (see Figure 4.1). On this bridge we have found a young star-forming region (ID #43), suggesting that on this object was formed *in situ*, on gaseous material which belongs to the main galaxies of this system. Indeed, region #43 displays an oxygen abundances that is similar to the value displayed by the main galaxies of the system, which prove that this system was formed from pre-enriched material, as also found in other interacting systems (Mendes de Oliveira et al. 2004, Trancho et al. 2012, Konstantopoulos et al. 2014b). The fate of this kind of systems is uncertain. They could be dissolved by their internal feedback (e.g. Fall et al. 2005) or they could survive as independent entities, as future globular clusters.

The morphology of the members of Arp 314 is complex. Despite the fact that Arp 314-1 displays a spiral pattern, the presence of shells around this galaxy supports the idea of a gravitational encounter. The scenario is even more dramatic for Arp 314-2 that displays a very perturbed morphology, where no spiral arms can be identified. Its central region is dominated by a star-forming burst, and several small-scale star-forming regions are lo-

cated around the centre, in a ring-like structure. The observed specific SFR (sSFR) of Arp 314-2 locates the object in the star-forming sequence of the M_*/sSFR plane (Schiminovich et al., 2007). To the east of this galaxy is observed an optical tidal tail, which contains a bright spot on its tip. Finally, the optical imaging of Arp 314-3 displays the typical morphology of an irregular galaxy, where a stellar bar can be identified. Elmegreen et al. (1993) speculate that this object was formed from tidal debris. However, this scenario could be discarded, given that this object displays a quite low oxygen abundance, lower than the values estimated for Arp 314-1 and Arp 314-2.

In addition to the morphological features associated with gravitation encounters, a wealth of kinematic peculiarities have been measured in interacting systems showing the close link between interactions and the presence of non-circular motions, distorted velocity field, changing position angle along the major axis, gas kinematics axis misalignment with respect to the stellar component axis and/or the stellar kinematic axis, kinematically decoupled core. These features have been largely observed for a sample of compact group galaxies studied with Fabry-Perot data (e.g. Amram et al., 2003; Amram et al.; Muñoz-Elgueta et al., 2018), and the system Arp 314 is not the exception. Galaxies Arp 314-1 and Arp 314-2 display perturbed velocity fields and asymmetric $\text{H}\alpha$ profiles, which in some cases can be clearly resolved into double components. In addition, non-circular motions are detected in the members of Arp 314, suggesting the existence of gas flows in these galaxies. These gas flows can play an important role in the evolution of interacting galaxies, given that they can transport gaseous material across the galaxies, favouring the metal mixing and fuelling the nuclear region of galaxies.

Indeed, the merging of gas-rich galaxies can be associated with nuclear inflows which will most probably create a strong central burst of star formation, which seems to be the case of Arp 314-2. On the other hand, gas flows can trigger the nuclear activity in interacting galaxies. In this context, Ellison et al. (2011) studied a sample of pairs galaxies, finding that the AGN fraction increase once the separation of the galaxy pair decrease (for pairs located at separations lower than $40 h_{70}^{-1}$ kpc). In the case of Arp 314, we found that Arp 314-1 is located in the “composite region” of the BPT diagnostic diagram. This fact may suggest that this object display nuclear star formation activity, plus a possible AGN contribution. However, recent studies based on 3D spectroscopy have found that evolved low-mass stars or even shocks can contribute to the ionization of the nuclear region (Rich et al., 2015; Belfiore et al., 2016). Future Gemini/GMOS 3D

spectroscopy of the nuclear region of Arp 314-1 can help us to discern the nature of this object.

4.5.2 Gas flows and the flattening of the gas-phase oxygen distribution

Several authors have found that interacting galaxies display flatter metallicity gradients than isolated systems, suggesting that gas flows during interacting events play an important role in the chemical evolution of these systems (e.g. Kewley et al., 2006, 2010; Rupke et al., 2010b). These gas flows should produce a metal dilution in the central region of interacting galaxies and they may be responsible in triggering star formation burst. These observational results have been confirmed by simulations (e.g. Rupke et al., 2010a). However, the suggested and expected gas flows are difficult to observe, given the complexity of interacting systems and also due to the lack of large field of view high-resolution spectroscopic data. In this sense, a combination of data that allow us to determine metallicity gradients (in large areas) plus a detailed kinematic analysis is essential to understand metallicity gradients in interacting systems. This has motivated us to study the metallicity evolution in a sample of galaxies located in small nearby galaxy groups. For most of these groups we have high resolution Fabry-Perot $H\alpha$ spectroscopic data, which is useful to determine the kinematics of these systems.

As part of this project, Torres-Flores et al. (2014b) have studied the metal distribution in the tidal tails of NGC 92, which is the main galaxy of the compact group called Robert's quartet, and found that NGC 92 displays a flat metallicity distribution along its tidal tail. However, the kinematic analysis data did not reveal the existence of a gas flow along it. As another part of this project, Torres-Flores et al. (2015) and Alfaro-Cuello et al. (2015) have studied the metal distribution in the merging compact group HCG 31. In this case, the use of integral field unit (IFU) spectroscopy plus $H\alpha$ Fabry-Perot data allow them to detect a gas flow between the nucleus of HCG 31A and HCG 31C. This gas flow should explain the smooth transition observed in the oxygen abundance between HCG 31A and HCG 31C. Finally, Olave-Rojas et al. (2015) have studied the chemical distribution in the tails of NGC 6845A, which is the main galaxy of the compact group NGC 6845, and also found a flat metallicity distribution; however no Fabry-Perot data was available for this target.

For the present study, by using the oxygen abundances of ten regions belonging to Arp 314-1 we have determined its metal distribution. We derived a slope which is consistent with the values found in sample of galaxy pairs studied by Kewley et al. (2010), which indicates a flatter metallicity distribution when compared with isolated systems. The result found for Arp 314-1 is consistent with the metallicity gradients measured in other galaxies belonging to small galaxy groups, suggesting that the group environment facilitate the mixture of gases and the chemical evolution of galaxies. However, our Fabry-Perot kinematic data does not reveal the existence of recent large gas flows in Arp 314-1, as could be expected from its metallicity distribution. If a gas-poor accretion occurred, as suggested by the rather flat metallicity distribution, this event must have occurred long enough for the traces of gaseous kinematic disturbances to have disappeared. Since the gas flow, the system had enough time to dampen this fresh gas supply and regain a dynamic equilibrium. The gas accretion has to be much older than the typical age of HII region, i.e. 10^7 yr. Large kinematic perturbations can be interpreted as signs of recent gas flows, as can be the case of Arp 314-2, or even other interacting systems analysed with Fabry-Perot data, where multiple profiles can be easily identified (e.g. Arp 299, Rampazzo et al. 2005; HCG 31, Amram et al. 2007). In the case of Arp 314-1, the kinematic data show asymmetric $H\alpha$ profiles, where a weak secondary component can be identified. This secondary component could suggest a small-scale gas accretion event, which may be playing a role in the chemical distribution of this system, but it should be accompanied by other process in order to strongly affect the metal distribution in Arp 314-1 (or previous gas flows have been responsible in flattening the metal distribution). We note that an extra mechanism can act to affect the metal distribution of galaxies. Martin et al. (2002) found evidence that galactic outflows are chemically enriched. Therefore, central outflows in Arp 314-1 could be carrying enriched material, which can be contributing in the flattening of the metal distribution. This scenario will be tested with future 3D spectroscopy of Arp 314-1. In the case of Arp 314-2, it is not possible to determine a metallicity gradient, given the few number of observed star-forming regions. However, the kinematics richness of this object converts it as an ideal target for 3D spectroscopic studies, which can be used to understand its metal distribution. Thus, the mixture of 3D high-resolution kinematic data and optical 3D spectroscopic capabilities (with large field of views) can be extremely useful to determine the importance of gas flows in the chemical evolution of interacting galaxies.

4.6 Summary and conclusions

In this Chapter we present new Gemini/GMOS images and spectroscopic observations of the poorly studied interacting system Arp 314. The main results are:

- Deep optical imaging reveals the presence of tidal tails, stellar bridges and shells around the main galaxies of this system. These features are typical signatures of galaxy-galaxy interactions.
- The spectrum of the nuclear region of Arp 314-1 displays emission line ratios that classified this source as a “composite object”, where the ionization arises from star formation plus AGN activity or shocks or the contribution of evolved low mass stars.
- The sSFR of Arp 314-2 locates this object in the star-forming sequence of the M_{\star} versus sSFR plane. Most of the star formation of this galaxy is located in a central burst, where double $H\alpha$ profiles can be identified. In addition, this galaxy displays a complex kinematics.
- The use of Gemini multislit data allowed us to follow the metallicity behavior of the main galaxy of this system, Arp 314-1, finding a flatter/complex metal distribution than the displayed by non-interacting systems. The observed metal distribution can be explained by the presence of gas flows, which were identified in this galaxy through the inspection of the kinematic data. However, it is unclear the real contribution of the observed gas flows in the flattening of the metal distribution.
- We discarded that Arp 314-3 had a tidal origin, mainly due to its low oxygen abundance, and suggested that Arp 314-3 is a primordial dwarf galaxy.

All the physical phenomena that are taking place in Arp 314 makes this system an ideal target to study galaxy transformation, and future integral field unit observations will reveal in more detail this important path in the evolution of galaxies.

5

Conclusions and Future Plans

The present chapter summarises the main results of the Thesis, outlining the main scientific conclusions and the implications that they have in the general context of galaxy evolution and giving an overview of the further developments that are planned for the present studies in the future.

5.1 General Conclusions

The present Thesis was dedicated to the study of the environmental drivers of galaxy evolution, focussing on the phenomenon of galaxy pre-processing which was addressed from a global and a local perspectives.

The first part of the Thesis addressed the problem of the relationships between cluster assembly and star-formation quenching in galaxies. We focussed on the importance that the accretion of quenched galaxies in clusters, especially when these galaxies are members of groups, has in the build-up of the red sequence. We identified substructures in the two $z = 0.4$ clusters MACS0416 and MACS1206, which are in two very different dynamical states, and studied the colours of galaxies in the clusters and in their substructures. We compared the fractions of red and blue galaxies, which are proxies for the fractions of quiescent and star-forming galaxies, in clusters, substructures and the field. We found that out to $3 \times r_{200}$ from the cluster centre the fraction of red galaxies in the clusters and in their substructures are always higher than in the field and, conversely, that the fractions of blue galaxies in the clusters and in their substructures are always lower than the fraction of star-forming galaxies in the field. We also found that substructures behave like

down-scaled clusters since the fractions of blue and red galaxies in them follow the same trends with distance from the centre and stellar mass that galaxies in clusters follow. As we discussed in Chapter 1, substructures are the remnants of the accretion of groups from the surrounding field and thus we conclude that pre-processing plays a significant role in the star-formation quenching of galaxies in clusters and in the resulting build-up of the red sequence.

In the second part of the Thesis we investigated the interaction processes that take place in groups, studying one particular system which is the Arp 314 group. We found that gravitational and tidal interactions in groups can change the morphology of galaxies and alter their star formation and the chemical composition of their stellar populations. The interaction that is happening in Arp 314 is promoting star formation in the group members. This result suggests that when groups of galaxies are accreted on to a cluster, their members may be undergoing or may have undergone a transformation in their morphology and star formation activity, supporting the notion that pre-processing represents an important piece in the evolution of cluster galaxies. It is interesting to note that the ongoing interaction in Arp 314 is enhancing star formation in the group members and that in Chapter 3 we showed that the fraction of blue galaxies in substructures is slightly higher than in the main clusters. If interactions that enhance star formation are happening in groups, then these may be, at least partly, responsible for the higher fraction of blue galaxies that we detect in substructures.

5.2 Future Plans

The results obtained in this Thesis lay the foundations for a systematic study of the environmental processes that regulate the evolution of galaxies and, in particular, of their relationships with the assembly of clusters. We plan to develop the study presented in the Thesis along the following directions:

- extension of the methodology developed in Chapter 3 to the CLASH-VLT and/or other large cluster samples to study the effects of pre-processing as a function of cosmic time;
- study of the luminosity/stellar mass distributions of galaxies in clusters and substructures to investigate the different pathways to star formation quenching and

stellar mass assembly in clusters and accreted groups;

- extension of the study presented in Chapter 4 to a large sample of interacting galaxies in groups to derive a complete view of the physical mechanisms that pre-process galaxies;
- application of the global and local approaches developed in Chapters 3 and 4, respectively, to samples of clusters that have sufficient spatial coverage to include the outskirts and high-resolution IFU spectroscopy of galaxies in infalling groups and substructures.

All these studies will allow us to draw a comprehensive picture of pre-processing and to understand the actual importance that this phenomenon has in the evolution of galaxies.



Bibliography

- Abazajian, K. N., Adelman-McCarthy, J. K., Agüeros, M. A., Allam, S. S., Allende Prieto, C., An, D., Anderson, K. S. J., Anderson, S. F., Annis, J., Bahcall, N. A., & et al., *ApJS*, 182:543-558, June 2009.
- Aguerri, J. A. L., Sánchez-Janssen, R., & Muñoz-Tuñón, C., *A&A*, 471:17–29, August 2007.
- Alberts, S., Pope, A., Brodwin, M., Atlee, D. W., Lin, Y.-T., Dey, A., Eisenhardt, P. R. M., Gettings, D. P., Gonzalez, A. H., Jannuzi, B. T., Mancone, C. L., Moustakas, J., Snyder, G. F., Stanford, S. A., Stern, D., Weiner, B. J., & Zeimann, G. R., *MNRAS*, 437:437–457, January 2014.
- Alfaro-Cuello, M., Torres-Flores, S., Carrasco, E. R., Mendes de Oliveira, C., de Mello, D. F., & Amram, P., *MNRAS*, 453:1355–1370, October 2015.
- Allende Prieto, C., Lambert, D. L., & Asplund, M., *ApJ*, 556:L63–L66, July 2001.
- Amram, P., Plana, H., Mendes de Oliveira, C., Balkowski, C., & Boulesteix, J.
- Amram, P., Plana, H., Mendes de Oliveira, C., Balkowski, C., & Boulesteix, J., *A&A*, 402: 865–877, May 2003.
- Amram, P., Mendes de Oliveira, C., Plana, H., Balkowski, C., & Hernandez, O., *A&A*, 471:753–764, September 2007.
- Annunziatella, M., Biviano, A., Mercurio, A., & et al., *A&A*, 571:A80, November 2014.
- Arp, H., *ApJS*, 14:1, November 1966.
- Arribas, S., Colina, L., Bellocchi, E., Maiolino, R., & Villar-Martín, M., *A&A*, 568:A14, August 2014.
- Baade, D., Meisenheimer, K., Iwert, O., & et al., *The Messenger*, 95:15–16, March 1999.
- Baba, H., Yasuda, N., Ichikawa, S.-I., Yagi, M., Iwamoto, N., Takata, T., Horaguchi, T., Taga, M., Watanabe, M., Okumura, S.-I., Ozawa, T., Yamamoto, N., & Hamabe, M., *Report of the National Astronomical Observatory of Japan*, 6:23–36, September 2002.

- Bacon, R., Accardo, M., Adjali, L., Anwand, H., Bauer, S.-M., Blaizot, J., Boudon, D., Brinchmann, J., Brotons, L., Caillier, P., Capoani, L., Carollo, M., Comin, M., Contini, T., Cumani, C., Daguis, E., Deiries, S., Delabre, B., Dreizler, S., Dubois, J.-P., Dupieux, M., Dupuy, C., Emsellem, E., Fleischmann, A., François, M., Gallou, G., Gharsa, T., Girard, N., Glindemann, A., Guiderdoni, B., Hahn, T., Hansali, G., Hofmann, D., Jarno, A., Kelz, A., Kiekebusch, M., Knudstrup, J., Koehler, C., Kollatschny, W., Kosmalski, J., Laurent, F., Le Floch, M., Lilly, S., Lizon à L'Allemand, J.-L., Loupias, M., Manescau, A., Monstein, C., Nicklas, H., Niemeyer, J., Olaya, J.-C., Palsa, R., Parès, L., Pasquini, L., Pécontal-Rousset, A., Pello, R., Petit, C., Piqueras, L., Popow, E., Reiss, R., Remillieux, A., Renault, E., Rhode, P., Richard, J., Roth, J., Rupprecht, G., Schaye, J., Slezak, E., Soucail, G., Steinmetz, M., Streicher, O., Stuik, R., Valentin, H., Vernet, J., Weilbacher, P., Wisotzki, L., Yerle, N., & Zins, G., *The Messenger*, 147: 4–6, March 2012.
- Bahé, Y. M. & McCarthy, I. G., *MNRAS*, 447:969–992, February 2015.
- Bahé, Y. M., McCarthy, I. G., Balogh, M. L., & Font, A. S., *MNRAS*, 430:3017–3031, April 2013.
- Baldry, I. K., Balogh, M. L., Bower, R. G., Glazebrook, K., Nichol, R. C., Bamford, S. P., & Budavari, T., *MNRAS*, 373:469–483, December 2006.
- Baldwin, J. A., Phillips, M. M., & Terlevich, R., *PASP*, 93:5–19, February 1981.
- Balestra, I., Mercurio, A., Sartoris, B., & et al., *ApJS*, 224:33, June 2016.
- Barnes, J. E. & Hernquist, L., *ApJ*, 471:115, November 1996.
- Barreira, A., Li, B., Jennings, E., Merten, J., King, L., Baugh, C. M., & Pascoli, S., *MNRAS*, 454:4085–4102, December 2015.
- Bastian, N., Tranco, G., Konstantopoulos, I. S., & Miller, B. W., *ApJ*, 701:607–619, August 2009.
- Beers, T. C., Flynn, K., & Gebhardt, K., *AJ*, 100:32–46, July 1990.
- Bekki, K., *ApJ*, 502:L133–L137, August 1998.

- Belfiore, F., Maiolino, R., Maraston, C., Emsellem, E., Bershad, M. A., Masters, K. L., Yan, R., Bizyaev, D., Boquien, M., Brownstein, J. R., Bundy, K., Drory, N., Heckman, T. M., Law, D. R., Roman-Lopes, A., Pan, K., Stanghellini, L., Thomas, D., Weijmans, A.-M., & Westfall, K. B., *MNRAS*, 461:3111–3134, September 2016.
- Bell, E. F. & de Jong, R. S., *ApJ*, 550:212–229, March 2001.
- Bell, E. F., McIntosh, D. H., Katz, N., & Weinberg, M. D., *ApJS*, 149:289–312, December 2003.
- Bender, R., Appenzeller, I., Böhm, A., & et al. *The FORS Deep Field: Photometric Data and Photometric Redshifts*. In Cristiani, S., Renzini, A., & Williams, R. E., editors, *Deep Fields*, page 96, 2001. doi: 10.1007/10854354_18.
- Bertin, E. *Automatic Astrometric and Photometric Calibration with SCAMP*. In Gabriel, C., Arviset, C., Ponz, D., & Enrique, S., editors, *Astronomical Data Analysis Software and Systems XV*, volume 351 of *Astronomical Society of the Pacific Conference Series*, page 112, July 2006.
- Bertin, E. *SWarp: Resampling and Co-adding FITS Images Together*. Astrophysics Source Code Library, October 2010.
- Bertin, E. *Automated Morphometry with SExtractor and PSFEx*. In Evans, I. N., Accomazzi, A., Mink, D. J., & Rots, A. H., editors, *Astronomical Data Analysis Software and Systems XX*, volume 442 of *Astronomical Society of the Pacific Conference Series*, page 435, July 2011.
- Bertin, E. & Arnouts, S., *A&AS*, 117:393–404, June 1996.
- Bianconi, M., Smith, G. P., Haines, C. P., McGee, S. L., Finoguenov, A., & Egami, E., *MNRAS*, 473:L79–L83, January 2018.
- Biviano, A., Rosati, P., Balestra, I., & et al., *A&A*, 558:A1, October 2013.
- Blanton, M. R., Eisenstein, D., Hogg, D. W., Schlegel, D. J., & Brinkmann, J., *ApJ*, 629:143–157, August 2005.
- Boselli, A., Voyer, E., Boissier, S., Cucciati, O., Consolandi, G., Cortese, L., Fumagalli, M., Gavazzi, G., Heinis, S., Roehly, Y., & Toloba, E., *A&A*, 570:A69, October 2014.

- Boselli, A., Roehly, Y., Fossati, M., Buat, V., Boissier, S., Boquien, M., Burgarella, D., Ciesla, L., Gavazzi, G., & Serra, P., *A&A*, 596:A11, November 2016.
- Boulesteix, J., Georgelin, Y., Marcelin, M., & Monnet, G. *First results from CIGALE scanning Perot-Fabry interferometer*. In Boksenberg, A. & Crawford, D. L., editors, *Instrumentation in astronomy V*, volume 445 of *Proc. SPIE*, pages 37–41, January 1984. doi: 10.1117/12.966123.
- Bravo-Alfaro, H., Caretta, C. A., Lobo, C., Durret, F., & Scott, T., *A&A*, 495:379–387, February 2009.
- Brescia, M., Cavuoti, S., D’Abrusco, R., Longo, G., & Mercurio, A., *ApJ*, 772:140, August 2013.
- Bresolin, F., *ApJ*, 656:186–197, February 2007.
- Bresolin, F., Kennicutt, R. C., & Ryan-Weber, E., *ApJ*, 750:122, May 2012.
- Brimioulle, F., Seitz, S., Lerchster, M., Bender, R., & Snigula, J., *MNRAS*, 432:1046–1102, June 2013.
- Bruzual, G. & Charlot, S., *MNRAS*, 344:1000–1028, October 2003.
- Byrd, G. & Valtonen, M., *ApJ*, 350:89–94, February 1990.
- Calzetti, D., Armus, L., Bohlin, R. C., Kinney, A. L., Koornneef, J., & Storchi-Bergmann, T., *ApJ*, 533:682–695, April 2000.
- Calzetti, D., Kennicutt, R. C., Engelbracht, C. W., Leitherer, C., Draine, B. T., Kewley, L., Moustakas, J., Sosey, M., & et al., *ApJ*, 666:870–895, September 2007.
- Cameron, E., *pasa*, 28:128–139, June 2011.
- Caminha, G. B., Grillo, C., Rosati, P., Balestra, I., Mercurio, A., Vanzella, E., Biviano, A., Caputi, K. I., Delgado-Correal, C., Karman, W., Lombardi, M., Meneghetti, M., Sartoris, B., & Tozzi, P., *A&A*, 600:A90, April 2017.
- Cappellari, M. & Emsellem, E., *PASP*, 116:138–147, February 2004.

- Cerulo, P., Couch, W. J., Lidman, C., Delaye, L., Demarco, R., Huertas-Company, M., Mei, S., & Sánchez-Janssen, R., *MNRAS*, 439:2790–2812, April 2014.
- Cerulo, P., Couch, W. J., Lidman, C., Demarco, R., Huertas-Company, M., Mei, S., Sánchez-Janssen, R., Barrientos, L. F., & Muñoz, R. P., *MNRAS*, 457:2209–2235, April 2016.
- Cerulo, P., Couch, W. J., Lidman, C., Demarco, R., Huertas-Company, M., Mei, S., Sánchez-Janssen, R., Barrientos, L. F., & Muñoz, R. P., *ArXiv e-prints*, July 2017.
- Chiang, Y.-K., Overzier, R., & Gebhardt, K., *ApJ*, 779:127, December 2013.
- Chien, L.-H., Barnes, J. E., Kewley, L. J., & Chambers, K. C., *ApJ*, 660:L105–L108, May 2007.
- Cid Fernandes, R., Stasińska, G., Mateus, A., & Vale Asari, N., *MNRAS*, 413:1687–1699, May 2011.
- Clampin, M., Ford, H., Bely, P., Burrows, C., Hartig, G., Postman, M., Sparks, W., White, R. L., Illingworth, G., Broadhurst, T., Golimowski, D. A., Feldman, P., Tsvetanov, Z., Cheng, E., Kimble, R., Neff, S., Leviton, D., Miley, G., Bartko, F., & Woodruff, R. *The Advanced Camera for Surveys*. In Benvenuti, P., Macchetto, F. D., & Schreier, E. J., editors, *Science with the Hubble Space Telescope - II*, page 597, 1996.
- Cluver, M. E., Jarrett, T. H., Hopkins, A. M., Driver, S. P., Liske, J., Gunawardhana, M. L. P., Taylor, E. N., Robotham, A. S. G., Alpaslan, M., Baldry, I., Brown, M. J. I., Peacock, J. A., Popescu, C. C., Tuffs, R. J., Bauer, A. E., Bland-Hawthorn, J., Colless, M., Holwerda, B. W., Lara-López, M. A., Leschinski, K., López-Sánchez, A. R., Norberg, P., Owers, M. S., Wang, L., & Wilkins, S. M., *ApJ*, 782:90, February 2014.
- Cohn, J. D., *MNRAS*, 419:1017–1027, January 2012.
- Cortese, L., *A&A*, 543:A132, July 2012.
- Cortese, L. & Hughes, T. M., *MNRAS*, 400:1225–1240, December 2009.
- Cortese, L., Gavazzi, G., Boselli, A., Franzetti, P., Kennicutt, R. C., O’Neil, K., & Sakai, S., *A&A*, 453:847–861, July 2006.

- Couch, W. J., Barger, A. J., Smail, I., Ellis, R. S., & Sharples, R. M., *ApJ*, 497:188–211, April 1998.
- Cybulski, R., Yun, M. S., Fazio, G. G., & Gutermuth, R. A., *MNRAS*, 439:3564–3586, April 2014.
- D'Agostini, G., *ArXiv Physics e-prints*, December 2004.
- Dahari, O., *ApJS*, 57:643–664, April 1985.
- Daigle, O., Carignan, C., Hernandez, O., Chemin, L., & Amram, P., *MNRAS*, 368:1016–1024, May 2006.
- Dalton, G. B., Caldwell, M., Ward, A. K., Whalley, M. S., Woodhouse, G., Edeson, R. L., Clark, P., Beard, S. M., Gallie, A. M., Todd, S. P., Strachan, J. M. D., Bezawada, N. N., Sutherland, W. J., & Emerson, J. P. *The VISTA infrared camera*. In *Society of Photo-Optical Instrumentation Engineers (SPIE) Conference Series*, volume 6269 of *Proc. SPIE*, page 62690X, June 2006. doi: 10.1117/12.670018.
- Dang, X., Peng, H., Wang, X., & Zhang, H. *Theil-Sen Estimators in a Multiple Linear Regression Model*. 2006.
- De Lucia, G., Poggianti, B. M., Aragón-Salamanca, A., White, S. D. M., Zaritsky, D., Clowe, D., Halliday, C., Jablonka, P., von der Linden, A., Milvang-Jensen, B., Pelló, R., Rudnick, G., Saglia, R. P., & Simard, L., *MNRAS*, 374:809–822, January 2007.
- De Lucia, G., Weinmann, S., Poggianti, B. M., Aragón-Salamanca, A., & Zaritsky, D., *MNRAS*, 423:1277–1292, June 2012.
- de Mello, D. F., Smith, L. J., Sabbi, E., Gallagher, J. S., Mountain, M., & Harbeck, D. R., *AJ*, 135:548–554, February 2008.
- Demarco, R., Rosati, P., Lidman, C., & et al., *ApJ*, 663:164–182, July 2007.
- Demarco, R., Gobat, R., Rosati, P., Lidman, C., Rettura, A., Nonino, M., van der Wel, A., Jee, M. J., Blakeslee, J. P., Ford, H. C., & Postman, M., *ApJ*, 725:1252–1276, December 2010.

- Dempster, A. P., Laird, N. M., & Rubin, D. B., *JOURNAL OF THE ROYAL STATISTICAL SOCIETY, SERIES B*, 39(1):1–38, 1977.
- Denicoló, G., Terlevich, R., & Terlevich, E., *MNRAS*, 330:69–74, February 2002.
- Diaferio, A., *MNRAS*, 309:610–622, November 1999.
- Domínguez, A., Siana, B., Henry, A. L., Scarlata, C., Bedregal, A. G., Malkan, M., Atek, H., Ross, N. R., Colbert, J. W., Teplitz, H. I., Rafelski, M., McCarthy, P., Bunker, A., Hathi, N. P., Dressler, A., Martin, C. L., & Masters, D., *ApJ*, 763:145, February 2013.
- Dressler, A., *ApJ*, 236:351–365, March 1980.
- Dressler, A. & Shectman, S. A., *AJ*, 95:985–995, April 1988.
- Dressler, A., Oemler, Jr., A., Couch, W. J., Smail, I., Ellis, R. S., Barger, A., Butcher, H., Poggianti, B. M., & Sharples, R. M., *ApJ*, 490:577–591, December 1997.
- Dressler, A., Smail, I., Poggianti, B. M., Butcher, H., Couch, W. J., Ellis, R. S., & Oemler, Jr., A., *ApJS*, 122:51–80, May 1999.
- Dressler, A., Oemler, Jr., A., Poggianti, B. M., Gladders, M. D., Abramson, L., & Vulcani, B., *ApJ*, 770:62, June 2013.
- Duc, P.-A. & Bournaud, F., *ApJ*, 673:787–797, February 2008.
- Ebeling, H., *MNRAS*, 340:1269–1278, April 2003.
- Ebeling, H., Edge, A. C., & Henry, J. P., *ApJ*, 553:668–676, June 2001.
- Ebeling, H., Ma, C. J., Kneib, J.-P., Jullo, E., Courtney, N. J. D., Barrett, E., Edge, A. C., & Le Borgne, J.-F., *MNRAS*, 395:1213–1224, May 2009.
- Eichner, T., Seitz, S., Suyu, S. H., Halkola, A., Umetsu, K., Zitrin, A., Coe, D., Monna, A., Rosati, P., Grillo, C., Balestra, I., Postman, M., Koekemoer, A., Zheng, W., Høst, O., Lemze, D., Broadhurst, T., Moustakas, L., Bradley, L., Molino, A., Nonino, M., Mercurio, A., Scodreggio, M., Bartelmann, M., Benitez, N., Bouwens, R., Donahue, M., Infante, L., Jouvel, S., Kelson, D., Lahav, O., Medezinski, E., Melchior, P., Merten, J., & Riess, A., *ApJ*, 774:124, September 2013.

- Einasto, J., *Trudy Astrofizicheskogo Instituta Alma-Ata*, 5:87–100, 1965.
- Eke, V. R., Cole, S., & Frenk, C. S., *MNRAS*, 282, September 1996.
- Ellison, S. L., Patton, D. R., Simard, L., & McConnachie, A. W., *AJ*, 135:1877–1899, May 2008.
- Ellison, S. L., Patton, D. R., Simard, L., McConnachie, A. W., Baldry, I. K., & Mendel, J. T., *MNRAS*, 407:1514–1528, September 2010.
- Ellison, S. L., Patton, D. R., Mendel, J. T., & Scudder, J. M., *MNRAS*, 418:2043–2053, December 2011.
- Elmegreen, B. G., Kaufman, M., & Thomasson, M., *ApJ*, 412:90–98, July 1993.
- Emerson, J., McPherson, A., & Sutherland, W., *The Messenger*, 126:41–42, December 2006.
- Epinat, B., Amram, P., Marcelin, M., Balkowski, C., Daigle, O., Hernandez, O., Chemin, L., Carignan, C., Gach, J.-L., & Balard, P., *MNRAS*, 388:500–550, August 2008.
- Epinat, B., Amram, P., Balkowski, C., & Marcelin, M., *MNRAS*, 401:2113–2147, February 2010.
- Ester, M., Kriegel, H.-P., Sander, J., & Xu, X. *A Density-based Algorithm for Discovering Clusters a Density-based Algorithm for Discovering Clusters in Large Spatial Databases with Noise*. In *Proceedings of the Second International Conference on Knowledge Discovery and Data Mining*, KDD'96, pages 226–231. AAAI Press, 1996.
- Fakhouri, O., Ma, C.-P., & Boylan-Kolchin, M., *MNRAS*, 406:2267–2278, August 2010.
- Fall, S. M., Chandar, R., & Whitmore, B. C., *ApJ*, 631:L133–L136, October 2005.
- Finn, R. A., Zaritsky, D., McCarthy, Jr., D. W., Poggianti, B., Rudnick, G., Halliday, C., Milvang-Jensen, B., Pelló, R., & Simard, L., *ApJ*, 630:206–227, September 2005.
- Firpo, V., Bosch, G., Hägele, G. F., & Morrell, N., *MNRAS*, 406:1094–1107, August 2010.

- Fitchett, M. J. *Substructure in clusters of galaxies*. In Dickey, J. M., editor, *The Minnesota lectures on Clusters of Galaxies and Large-Scale Structure*, volume 5 of *Astronomical Society of the Pacific Conference Series*, pages 143–174, 1988.
- Fitzpatrick, E. L., *PASP*, 111:63–75, January 1999.
- Font, J., Beckman, J. E., Rosado, M., Epinat, B., Fathi, K., Hernandez, O., Carignan, C., Gutiérrez, L., Relaño, M., Blasco-Herrera, J., & Fuentes-Carrera, I., *ApJ*, 740:L1, October 2011.
- Fujita, Y., *PASJ*, 56:29–43, February 2004.
- Garcia, A. M., *A&A*, 297:56–60, May 1995.
- Garilli, B., Fumana, M., Franzetti, P., Paioro, L., Scodeggio, M., Le Fèvre, O., Paltani, S., & Scaramella, R., *PASP*, 122:827, July 2010.
- Gavazzi, G., Consolandi, G., Dotti, M., Fanali, R., Fossati, M., Fumagalli, M., Viscardi, E., Savorgnan, G., Boselli, A., Gutiérrez, L., Hernández Toledo, H., Giovanelli, R., & Haynes, M. P., *A&A*, 580:A116, August 2015.
- George, M. R., Leauthaud, A., Bundy, K., & et al., *ApJ*, 742:125, December 2011.
- Gil de Paz, A., Boissier, S., Madore, B. F., Seibert, M., Joe, Y. H., Boselli, A., Wyder, T. K., Thilker, D., Bianchi, L., Rey, S.-C., Rich, R. M., Barlow, T. A., Conrow, T., Forster, K., Friedman, P. G., Martin, D. C., Morrissey, P., Neff, S. G., Schiminovich, D., Small, T., Donas, J., Heckman, T. M., Lee, Y.-W., Milliard, B., Szalay, A. S., & Yi, S., *ApJS*, 173:185–255, December 2007.
- Girardi, M., Escalera, E., Fadda, D., Giuricin, G., Mardirossian, F., & Mezzetti, M., *ArXiv Astrophysics e-prints*, December 1996.
- Girardi, M., Demarco, R., Rosati, P., & Borgani, S., *A&A*, 442:29–41, October 2005.
- Girardi, M., Mercurio, A., Balestra, I., & et al., *A&A*, 579:A4, July 2015.
- Gobat, R., Rosati, P., Strazzullo, V., Rettura, A., Demarco, R., & Nonino, M., *A&A*, 488: 853–860, September 2008.

- Goto, T., Yamauchi, C., Fujita, Y., Okamura, S., Sekiguchi, M., Smail, I., Bernardi, M., & Gomez, P. L., *MNRAS*, 346:601–614, December 2003.
- Gruen, D., Brimiouille, F., Seitz, S., Lee, C.-H., Young, J., Koppenhoefer, J., Eichner, T., Riffeser, A., Vikram, V., Weidinger, T., & Zenteno, A., *MNRAS*, 432:1455–1467, June 2013.
- Gruen, D., Seitz, S., Brimiouille, F., Kosyra, R., Koppenhoefer, J., Lee, C.-H., Bender, R., Riffeser, A., Eichner, T., Weidinger, T., & Bierschenk, M., *MNRAS*, 442:1507–1544, August 2014.
- Grützbauch, R., Chuter, R. W., Conselice, C. J., Bauer, A. E., Bluck, A. F. L., Buitrago, F., & Mortlock, A., *MNRAS*, 412:2361–2375, April 2011a.
- Grützbauch, R., Conselice, C. J., Varela, J., Bundy, K., Cooper, M. C., Skibba, R., & Willmer, C. N. A., *MNRAS*, 411:929–946, February 2011b.
- Gunn, J. E. & Gott, III, J. R., *ApJ*, 176:1, August 1972.
- Haines, C. P., Gargiulo, A., & Merluzzi, P., *MNRAS*, 385:1201–1210, April 2008.
- Haines, C. P., Pereira, M. J., Smith, G. P., Egami, E., Babul, A., Finoguenov, A., Ziparo, F., McGee, S. L., Rawle, T. D., Okabe, N., & Moran, S. M., *ApJ*, 806:101, June 2015.
- Harrison, E. R., *ApJ*, 191:L51, July 1974.
- Hernández-Fernández, J. D. & Mendes de Oliveira, C., *MNRAS*, 453:1965–1980, October 2015.
- Hernquist, L. & Quinn, P. J., *ApJ*, 342:1–16, July 1989.
- Hibbard, J. E., Vacca, W. D., & Yun, M. S., *AJ*, 119:1130–1144, March 2000.
- Holden, B. P., Illingworth, G. D., Franx, M., Blakeslee, J. P., Postman, M., Kelson, D. D., van der Wel, A., Demarco, R., Magee, D. K., Tran, K.-V., Zirm, A., Ford, H., Rosati, P., & Homeier, N., *ApJ*, 670:190–205, November 2007.
- Hook, I. M., Jørgensen, I., Allington-Smith, J. R., Davies, R. L., Metcalfe, N., Murowinski, R. G., & Crampton, D., *PASP*, 116:425–440, May 2004.

- Hou, A., Parker, L. C., & Harris, W. E., *MNRAS*, 442:406–418, July 2014.
- Jaffé, Y. L., Aragón-Salamanca, A., Kuntschner, H., Bamford, S., Hoyos, C., De Lucia, G., Halliday, C., Milvang-Jensen, B., Poggianti, B., Rudnick, G., Saglia, R. P., Sanchez-Blazquez, P., & Zaritsky, D., *MNRAS*, 417:1996–2019, November 2011.
- Jaffé, Y. L., Poggianti, B. M., Verheijen, M. A. W., Deshev, B. Z., & van Gorkom, J. H., *MNRAS*, 431:2111–2125, May 2013.
- Jaffé, Y. L., Verheijen, M. A. W., Haines, C. P., Yoon, H., Cybulski, R., Montero-Castaño, M., Smith, R., Chung, A., Deshev, B. Z., Fernández, X., van Gorkom, J., Poggianti, B. M., Yun, M. S., Finoguenov, A., Smith, G. P., & Okabe, N., *MNRAS*, April 2016.
- Jarrett, T. H., Masci, F., Tsai, C. W., Petty, S., Cluver, M. E., Assef, R. J., Benford, D., Blain, A., Bridge, C., Donoso, E., Eisenhardt, P., Koribalski, B., Lake, S., Neill, J. D., Seibert, M., Sheth, K., Stanford, S., & Wright, E., *AJ*, 145:6, January 2013.
- Jauzac, M., Jullo, E., Eckert, D., Ebeling, H., Richard, J., Limousin, M., Atek, H., Kneib, J.-P., Clément, B., Egami, E., Harvey, D., Knowles, K., Massey, R., Natarajan, P., Neichel, B., & Rexroth, M., *MNRAS*, 446:4132–4147, February 2015.
- Just, D. W., Zaritsky, D., Rudnick, G., Cool, R., Moustakas, J., Clowe, D., De Lucia, G., Aragón-Salamanca, A., Desai, V., Finn, R., Halliday, C., Jablonka, P., Poggianti, B., Bian, F.-Y., & Liebst, K., *ArXiv e-prints*, June 2015.
- Kauffmann, G., Heckman, T. M., Tremonti, C., Brinchmann, J., Charlot, S., White, S. D. M., Ridgway, S. E., Brinkmann, J., Fukugita, M., Hall, P. B., Ivezić, Ž., Richards, G. T., & Schneider, D. P., *MNRAS*, 346:1055–1077, December 2003.
- Kauffmann, G., White, S. D. M., Heckman, T. M., Ménard, B., Brinchmann, J., Charlot, S., Tremonti, C., & Brinkmann, J., *MNRAS*, 353:713–731, September 2004.
- Kawinwanichakij, L., Papovich, C., Quadri, R. F., Glazebrook, K., Kacprzak, G. G., Allen, R. J., Bell, E. F., Croton, D. J., Dekel, A., Ferguson, H. C., Forrest, B., Groggin, N. A., Guo, Y., Kocevski, D. D., Koekemoer, A. M., Labbé, I., Lucas, R. A., Nanayakkara, T., Spitler, L. R., Straatman, C. M. S., Tran, K.-V. H., Tomczak, A., & van Dokkum, P., *ApJ*, 847:134, October 2017.

- Keel, W. C., Kennicutt, Jr., R. C., Hummel, E., & van der Hulst, J. M., *AJ*, 90:708–730, May 1985.
- Kennicutt, Jr., R. C., *ARA&A*, 36:189–232, 1998.
- Kewley, L. J., Dopita, M. A., Sutherland, R. S., Heisler, C. A., & Trevena, J., *ApJ*, 556:121–140, July 2001.
- Kewley, L. J., Geller, M. J., & Barton, E. J., *AJ*, 131:2004–2017, April 2006.
- Kewley, L. J., Rupke, D., Zahid, H. J., Geller, M. J., & Barton, E. J., *ApJ*, 721:L48–L52, September 2010.
- Kimble, R. A., MacKenty, J. W., O’Connell, R. W., & Townsend, J. A. *Wide Field Camera 3: a powerful new imager for the Hubble Space Telescope*. In *Space Telescopes and Instrumentation 2008: Optical, Infrared, and Millimeter*, volume 7010 of *Proc. SPIE*, page 70101E, July 2008. doi: 10.1117/12.789581.
- Koekemoer, A. M., Avila, R. J., Hammer, D., Mack, J., Ogaz, S., Anderson, J., Barker, E. A., Hilbert, B., Gonzaga, S., Grogin, N. A., Fruchter, A. S., Lotz, J., Lucas, R. A., Mountain, M., & Sokol, J. *The HST Frontier Fields: Science Data Pipeline, Products, and First Data Release*. In *American Astronomical Society Meeting Abstracts #223*, volume 223 of *American Astronomical Society Meeting Abstracts*, page 254.02, January 2014.
- Konstantopoulos, I. S., Appleton, P. N., Guillard, P., Trancho, G., Cluver, M. E., Bastian, N., Charlton, J. C., Fedotov, K., Gallagher, S. C., Smith, L. J., & Struck, C. J., *ApJ*, 784:1, March 2014a.
- Konstantopoulos, I. S., Appleton, P. N., Guillard, P., Trancho, G., Cluver, M. E., Bastian, N., Charlton, J. C., Fedotov, K., Gallagher, S. C., Smith, L. J., & Struck, C. J., *ApJ*, 784:1, March 2014b.
- Kravtsov, A. V. & Borgani, S., *ARA&A*, 50:353–409, September 2012.
- Larson, R. B., Tinsley, B. M., & Caldwell, C. N., *ApJ*, 237:692–707, May 1980.
- Le Fèvre, O., Saisse, M., Mancini, D., & et al. *Commissioning and performances of the VLT-VIMOS instrument*. In Iye, M. & Moorwood, A. F. M., editors, *Instrument*

- Design and Performance for Optical/Infrared Ground-based Telescopes*, volume 4841 of *Proc. SPIE*, pages 1670–1681, March 2003. doi: 10.1117/12.460959.
- Lemaux, B. C., Gal, R. R., Lubin, L. M., Kocevski, D. D., Fassnacht, C. D., McGrath, E. J., Squires, G. K., Surace, J. A., & Lacy, M., *ApJ*, 745:106, February 2012.
- Lewis, I., Balogh, M., De Propriis, R., Couch, W., Bower, R., Offer, A., Bland-Hawthorn, J., Baldry, I. K., Baugh, C., Bridges, T., Cannon, R., Cole, S., Colless, M., Collins, C., Cross, N., Dalton, G., Driver, S. P., Efstathiou, G., Ellis, R. S., Frenk, C. S., Glazebrook, K., Hawkins, E., Jackson, C., Lahav, O., Lumsden, S., Maddox, S., Madgwick, D., Norberg, P., Peacock, J. A., Percival, W., Peterson, B. A., Sutherland, W., & Taylor, K., *MNRAS*, 334:673–683, August 2002.
- Li, I. H., Yee, H. K. C., & Ellingson, E., *ApJ*, 698:83–98, June 2009.
- Lloyd, S., *IEEE Trans. Inf. Theor.*, 28(2):129–137, September 2006. ISSN 0018-9448.
- Lotz, J. M., Koekemoer, A., Coe, D., Grogan, N., Capak, P., Mack, J., Anderson, J., Avila, R., Barker, E. A., Borncamp, D., Brammer, G., & et al., *ApJ*, 837:97, March 2017.
- Mancone, C. L. & Gonzalez, A. H., *PASP*, 124:606, June 2012.
- Mann, A. W. & Ebeling, H., *MNRAS*, 420:2120–2138, March 2012.
- Marino, R. A., Rosales-Ortega, F. F., Sánchez, S. F., Gil de Paz, A., Vílchez, J., Miralles-Caballero, D., Kehrig, C., Pérez-Montero, E., Stanishev, V., & et al., *A&A*, 559:A114, November 2013.
- Martin, C. L., Kobulnicky, H. A., & Heckman, T. M., *ApJ*, 574:663–692, August 2002.
- Martin, D. C., Fanson, J., Schiminovich, D., Morrissey, P., Friedman, P. G., Barlow, T. A., Conrow, T., Grange, R., Jelinsky, P. N., Milliard, B., Siegmund, O. H. W., Bianchi, L., Byun, Y.-I., Donas, J., Forster, K., Heckman, T. M., Lee, Y.-W., Madore, B. F., Malina, R. F., Neff, S. G., Rich, R. M., Small, T., Surber, F., Szalay, A. S., Welsh, B., & Wyder, T. K., *ApJ*, 619:L1–L6, January 2005.
- Masters, D. & Capak, P., *PASP*, 123:638, May 2011.

- McConnachie, A. W., Patton, D. R., Ellison, S. L., & Simard, L., *MNRAS*, 395:255–268, May 2009.
- McCracken, H. J., Milvang-Jensen, B., Dunlop, J., & et al., *A&A*, 544:A156, August 2012.
- McGee, S. L., Balogh, M. L., Bower, R. G., Font, A. S., & McCarthy, I. G., *MNRAS*, 400: 937–950, December 2009.
- Medezinski, E., Umetsu, K., Nonino, M., Merten, J., Zitrin, A., Broadhurst, T., Donahue, M., Sayers, J., Waizmann, J.-C., Koekemoer, A., Coe, D., Molino, A., Melchior, P., Mroczkowski, T., Czakon, N., Postman, M., Meneghetti, M., Lemze, D., Ford, H., Grillo, C., Kelson, D., Bradley, L., Moustakas, J., Bartelmann, M., Benítez, N., Biviano, A., Bouwens, R., Golwala, S., Graves, G., Infante, L., Jiménez-Teja, Y., Jouvel, S., Lahav, O., Moustakas, L., Ogaz, S., Rosati, P., Seitz, S., & Zheng, W., *ApJ*, 777:43, November 2013.
- Mei, S., Holden, B. P., Blakeslee, J. P., Ford, H. C., Franx, M., Homeier, N. L., Illingworth, G. D., Jee, M. J., Overzier, R., Postman, M., Rosati, P., Van der Wel, A., & Bartlett, J. G., *ApJ*, 690:42–68, January 2009.
- Mei, S., Stanford, S. A., Holden, B. P., Raichoor, A., Postman, M., Nakata, F., Finoguenov, A., Ford, H. C., Illingworth, G. D., Kodama, T., Rosati, P., Tanaka, M., Huertas-Company, M., Rettura, A., Shankar, F., Carrasco, E. R., Demarco, R., Eisenhardt, P., Jee, M. J., Koyama, Y., & White, R. L., *ApJ*, 754:141, August 2012.
- Mendes de Oliveira, C. & Hickson, P., *ApJ*, 427:684–695, June 1994.
- Mendes de Oliveira, C., Cypriano, E. S., Sodré, Jr., L., & Balkowski, C., *ApJ*, 605:L17–L20, April 2004.
- Mercurio, A., Rosati, P., Annunziatella, M., Balestra, I., Biviano, A., Girardi, M., Grillo, C., Nonino, M., Presotto, V., Sartoris, B., Postman, M., CLASH-VLT Team, & CLASH Team. *Galaxy population as a function of the environment: a study in MACSJ1206 at $z\sim 0.44$* . In *The evolution of galaxy clusters and cluster galaxies in the epoch of large optical/IR surveys, proceedings of a conference held 13-17 January, 2014 at the Sexten Center for Astrophysics.*, id.12, page 12, 2014.

- Mercurio, A., Annunziatella, M., Biviano, A., Nonino, M., Rosati, P., Balestra, I., Brescia, M., Girardi, M., Gobat, R., Grillo, C., Lombardi, M., & Sartoris, B., *The Universe of Digital Sky Surveys*, 42:225, 2016.
- Merten, J., Meneghetti, M., Postman, M., & et al., *ApJ*, 806:4, June 2015.
- Mihos, C., *ArXiv Astrophysics e-prints*, May 2003.
- Miller, R. H., *A&A*, 167:41–52, October 1986.
- Miralles-Caballero, D., Colina, L., & Arribas, S., *A&A*, 538:A61, February 2012.
- Miyazaki, S., Komiyama, Y., Sekiguchi, M., Okamura, S., Doi, M., Furusawa, H., Hamabe, M., Imi, K., Kimura, M., Nakata, F., Okada, N., Ouchi, M., Shimasaku, K., Yagi, M., & Yasuda, N., *PASJ*, 54:833–853, December 2002.
- Moore, B., Katz, N., Lake, G., Dressler, A., & Oemler, A., *Nature*, 379:613–616, February 1996.
- Moore, B., Lake, G., Quinn, T., & Stadel, J., *MNRAS*, 304:465–474, April 1999.
- Mould, J. R., Huchra, J. P., Freedman, W. L., Kennicutt, Jr., R. C., Ferrarese, L., Ford, H. C., Gibson, B. K., Graham, J. A., Hughes, S. M. G., Illingworth, G. D., Kelson, D. D., Macri, L. M., Madore, B. F., Sakai, S., Sebo, K. M., Silbermann, N. A., & Stetson, P. B., *ApJ*, 529:786–794, February 2000.
- Muñoz-Elgueta, N., Torres-Flores, S., Amram, P., Hernandez-Jimenez, J. A., Urrutia-Viscarra, F., Mendes de Oliveira, C., & Gómez-López, J. A., *MNRAS*, 480:3257–3278, November 2018.
- Muñoz-Mateos, J. C., Gil de Paz, A., Boissier, S., Zamorano, J., Jarrett, T., Gallego, J., & Madore, B. F., *ApJ*, 658:1006–1026, April 2007.
- Muratov, A. L. & Gnedin, O. Y., *ApJ*, 718:1266–1288, August 2010.
- Muzzin, A., Wilson, G., Yee, H. K. C., Gilbank, D., Hoekstra, H., Demarco, R., Balogh, M., van Dokkum, P., Franx, M., Ellingson, E., Hicks, A., Nantais, J., Noble, A., Lacy, M., Lidman, C., Rettura, A., Surace, J., & Webb, T., *ApJ*, 746:188, February 2012.

- Muzzin, A., Marchesini, D., Stefanon, M., Franx, M., Milvang-Jensen, B., Dunlop, J. S., Fynbo, J. P. U., Brammer, G., Labbé, I., & van Dokkum, P., *ApJS*, 206:8, May 2013.
- Naab, T. & Burkert, A., *ApJ*, 597:893–906, November 2003.
- Nantais, J. B., van der Burg, R. F. J., Lidman, C., Demarco, R., Noble, A., Wilson, G., Muzzin, A., Foltz, R., DeGroot, A., & Cooper, M. C., *A&A*, 592:A161, August 2016.
- Nantais, J. B., Muzzin, A., van der Burg, R. F. J., Wilson, G., Lidman, C., Foltz, R., DeGroot, A., Noble, A., Cooper, M. C., & Demarco, R., *MNRAS*, 465:L104–L108, February 2017.
- Navarro, J. F., Frenk, C. S., & White, S. D. M., *MNRAS*, 275:56–66, July 1995.
- Navarro, J. F., Frenk, C. S., & White, S. D. M., *ApJ*, 490:493–508, December 1997.
- Nonino, M., Dickinson, M., Rosati, P., Grazian, A., Reddy, N., Cristiani, S., Giavalisco, M., Kuntschner, H., Vanzella, E., Daddi, E., Fosbury, R. A. E., & Cesarsky, C., *ApJS*, 183:244–260, August 2009.
- Nordgren, T. E., Chengalur, J. N., Salpeter, E. E., & Terzian, Y., *AJ*, 114:913–931, September 1997.
- Ogrea, G. A., van Weeren, R. J., Jones, C., Clarke, T. E., Sayers, J., Mroczkowski, T., Nulsen, P. E. J., Forman, W., Murray, S. S., Pandey-Pommier, M., Randall, S., Churazov, E., Bonafede, A., Kraft, R., David, L., Andrade-Santos, F., Merten, J., Zitrin, A., Umetsu, K., Goulding, A., Roediger, E., Bagchi, J., Bulbul, E., Donahue, M., Ebeling, H., Johnston-Hollitt, M., Mason, B., Rosati, P., & Vikhlinin, A., *ApJ*, 812:153, October 2015.
- Oke, J. B., *ApJS*, 27:21, February 1974.
- Olave-Rojas, D., Torres-Flores, S., Carrasco, E. R., Mendes de Oliveira, C., de Mello, D. F., & Scarano, S., *MNRAS*, 453:2808–2823, November 2015.
- Olave-Rojas, D., Cerulo, P., Demarco, R., Jaffé, Y. L., Mercurio, A., Rosati, P., Balestra, I., & Nonino, M., *MNRAS*, 479:2328–2350, September 2018.

- Osterbrock, D. E. *Astrophysics of gaseous nebulae and active galactic nuclei*. University Science Books, 1989, 422 p., 1989.
- Patel, S. G., Kelson, D. D., Holden, B. P., Franx, M., & Illingworth, G. D., *ApJ*, 735:53, July 2011.
- Peng, Y.-j., Lilly, S. J., Kovač, K., & et al., *ApJ*, 721:193–221, September 2010.
- Peng, Y.-j., Lilly, S. J., Renzini, A., & Carollo, M., *ApJ*, 757:4, September 2012.
- Perez, J., Michel-Dansac, L., & Tissera, P. B., *MNRAS*, 417:580–590, October 2011.
- Pettini, M. & Pagel, B. E. J., *MNRAS*, 348:L59–L63, March 2004.
- Pickles, A. J., *PASP*, 110:863–878, July 1998.
- Poggianti, B. M., Smail, I., Dressler, A., Couch, W. J., Barger, A. J., Butcher, H., Ellis, R. S., & Oemler, Jr., A., *ApJ*, 518:576–593, June 1999.
- Poggianti, B. M., von der Linden, A., De Lucia, G., & et al., *ApJ*, 642:188–215, May 2006.
- Postman, M., Franx, M., Cross, N. J. G., & et al., *ApJ*, 623:721–741, April 2005.
- Postman, M., Coe, D., Benítez, N., & et al., *ApJS*, 199:25, April 2012.
- Press, W. H. & Schechter, P., *ApJ*, 187:425–438, February 1974.
- Press, W. H., Teukolsky, S. A., Vetterling, W. T., & Flannery, B. P. *Numerical Recipes 3rd Edition: The Art of Scientific Computing*. Cambridge University Press, New York, NY, USA, 3 edition, 2007. ISBN 0521880688, 9780521880688.
- Rampazzo, R., Plana, H., Amram, P., Bagarotto, S., Boulesteix, J., & Rosado, M., *MNRAS*, 356:1177–1190, January 2005.
- Rich, J. A., Kewley, L. J., & Dopita, M. A., *ApJS*, 221:28, December 2015.
- Rosati, P., Balestra, I., Grillo, C., Mercurio, A., Nonino, M., Biviano, A., Girardi, M., Vanzella, E., & Clash-VLT Team, *The Messenger*, 158:48–53, December 2014.
- Rupke, D. S., Veilleux, S., & Sanders, D. B., *ApJS*, 160:87–114, September 2005.

- Rupke, D. S. N., Kewley, L. J., & Barnes, J. E., *ApJ*, 710:L156–L160, February 2010a.
- Rupke, D. S. N., Kewley, L. J., & Chien, L.-H., *ApJ*, 723:1255–1271, November 2010b.
- Salpeter, E. E., *ApJ*, 121:161, January 1955.
- Sánchez-Blázquez, P., Peletier, R. F., Jiménez-Vicente, J., Cardiel, N., Cenarro, A. J., Falcón-Barroso, J., Gorgas, J., Selam, S., & Vazdekis, A., *MNRAS*, 371:703–718, September 2006.
- Scarano, S., Madsen, F. R. H., Roy, N., & Lépine, J. R. D., *MNRAS*, 386:963–972, May 2008.
- Scarano, Jr., S., Lépine, J. R. D., & Marcon-Uchida, M. M., *MNRAS*, 412:1741–1754, April 2011.
- Schawinski, K., Urry, C. M., Simmons, B. D., Fortson, L., Kaviraj, S., Keel, W. C., Lintott, C. J., Masters, K. L., Nichol, R. C., Sarzi, M., Skibba, R., Treister, E., Willett, K. W., Wong, O. I., & Yi, S. K., *MNRAS*, 440:889–907, May 2014.
- Schiminovich, D., Wyder, T. K., Martin, D. C., Johnson, B. D., Salim, S., Seibert, M., Treyer, M. A., Budavári, T., Hoopes, C., Zamojski, M., Barlow, T. A., Forster, K. G., Friedman, P. G., Morrissey, P., Neff, S. G., Small, T. A., Bianchi, L., Donas, J., Heckman, T. M., Lee, Y.-W., Madore, B. F., Milliard, B., Rich, R. M., Szalay, A. S., Welsh, B. Y., & Yi, S., *ApJS*, 173:315–341, December 2007.
- Schlafly, E. F. & Finkbeiner, D. P., *ApJ*, 737:103, August 2011.
- Schlegel, D. J., Finkbeiner, D. P., & Davis, M., *ApJ*, 500:525, June 1998.
- Schneider, P. *Extragalactic Astronomy and Cosmology*. Berlin: Springer, 2006.
- Scoddeggio, M., Franzetti, P., Garilli, B., & et al., *PASP*, 117:1284–1295, November 2005.
- Scoville, N., Aussel, H., Brusa, M., & et al., *ApJS*, 172:1–8, September 2007.
- Scudder, J. M., Ellison, S. L., Torrey, P., Patton, D. R., & Mendel, J. T., *MNRAS*, 426: 549–565, October 2012.

- Skibba, R. A., Bamford, S. P., Nichol, R. C., Lintott, C. J., Andreescu, D., Edmondson, E. M., Murray, P., Raddick, M. J., Schawinski, K., Slosar, A., Szalay, A. S., Thomas, D., & Vandenberg, J., *MNRAS*, 399:966–982, October 2009.
- Skrutskie, M. F., Cutri, R. M., Stiening, R., & et al., *AJ*, 131:1163–1183, February 2006.
- Smith, B. J., Struck, C., Hancock, M., Appleton, P. N., Charmandaris, V., & Reach, W. T., *AJ*, 133:791–817, March 2007.
- Smith, G. P., Khosroshahi, H. G., Dariush, A., Sanderson, A. J. R., Ponman, T. J., Stott, J. P., Haines, C. P., Egami, E., & Stark, D. P., *MNRAS*, 409:169–183, November 2010.
- Sohn, J., Hwang, H. S., Geller, M. J., Diaferio, A., Rines, K. J., Lee, M. G., & Lee, G.-H., *Journal of Korean Astronomical Society*, 48:381–398, December 2015.
- Spergel, D. N., Verde, L., Peiris, H. V., Komatsu, E., Nolta, M. R., Bennett, C. L., Halpern, M., Hinshaw, G., Jarosik, N., Kogut, A., Limon, M., Meyer, S. S., Page, L., Tucker, G. S., Weiland, J. L., Wollack, E., & Wright, E. L., *ApJS*, 148:175–194, September 2003.
- Stasińska, G., *A&A*, 454:L127–L130, August 2006.
- Storchi-Bergmann, T., Calzetti, D., & Kinney, A. L., *ApJ*, 429:572–581, July 1994.
- Straatman, C. M. S., Spitler, L. R., Quadri, R. F., & et al., *ApJ*, 830:51, October 2016.
- Tempel, E., Tuvikene, T., Kipper, R., & Libeskind, N. I., *A&A*, 602:A100, June 2017.
- Toomre, A. & Toomre, J., *ApJ*, 178:623–666, December 1972.
- Torres-Flores, S., Amram, P., Mendes de Oliveira, C., Plana, H., Balkowski, C., Marcelin, M., & Olave-Rojas, D., *MNRAS*, 442:2188–2201, August 2014a.
- Torres-Flores, S., Scarano, S., Mendes de Oliveira, C., de Mello, D. F., Amram, P., & Plana, H., *MNRAS*, 438:1894–1908, February 2014b.
- Torres-Flores, S., Mendes de Oliveira, C., Amram, P., Alfaro-Cuello, M., Carrasco, E. R., & de Mello, D. F., *ApJ*, 798:L24, January 2015.

- Torres-Flores, S., Amram, P., Olave-Rojas, Muñoz-Elgueta, N., Mendes de Oliveira, C., de Mello, D. F., & Urrutia-Viscarra, F., *Submitted*, 2019.
- Tran, K.-V. H., Papovich, C., Saintonge, A., Brodwin, M., Dunlop, J. S., Farrah, D., Finkelstein, K. D., Finkelstein, S. L., Lotz, J., McLure, R. J., Momcheva, I., & Willmer, C. N. A., *ApJ*, 719:L126–L129, August 2010.
- Trancho, G., Konstantopoulos, I. S., Bastian, N., Fedotov, K., Gallagher, S., Mullan, B., & Charlton, J. C., *ApJ*, 748:102, April 2012.
- Tremonti, C. A., Heckman, T. M., Kauffmann, G., Brinchmann, J., Charlot, S., White, S. D. M., Seibert, M., Peng, E. W., Schlegel, D. J., Uomoto, A., Fukugita, M., & Brinkmann, J., *ApJ*, 613:898–913, October 2004.
- Umetsu, K., Medezinski, E., Nonino, M., & et al., *ApJ*, 755:56, August 2012.
- Umetsu, K., Medezinski, E., Nonino, M., & et al., *ApJ*, 795:163, November 2014.
- Umetsu, K., Zitrin, A., Gruen, D., Merten, J., Donahue, M., & Postman, M., *ApJ*, 821:116, April 2016.
- Valentijn, E. A., McFarland, J. P., Snigula, J., & et al. *Astro-WISE: Chaining to the Universe*. In Shaw, R. A., Hill, F., & Bell, D. J., editors, *Astronomical Data Analysis Software and Systems XVI*, volume 376 of *Astronomical Society of the Pacific Conference Series*, page 491, October 2007.
- Valentinuzzi, T., Poggianti, B. M., Fasano, G., D’Onofrio, M., Moretti, A., Ramella, M., Biviano, A., Fritz, J., Varela, J., Bettoni, D., Vulcani, B., Moles, M., Couch, W. J., Dressler, A., Kjærgaard, P., Omizzolo, A., & Cava, A., *A&A*, 536:A34, December 2011.
- van der Wel, A., Holden, B. P., Franx, M., Illingworth, G. D., Postman, M. P., Kelson, D. D., Labbé, I., Wuyts, S., Blakeslee, J. P., & Ford, H. C., *ApJ*, 670:206–220, November 2007.
- van Dokkum, P. G., *PASP*, 113:1420–1427, November 2001.
- Verdes-Montenegro, L., Yun, M. S., Williams, B. A., Huchtmeier, W. K., Del Olmo, A., & Perea, J., *A&A*, 377:812–826, October 2001.

- Vijayaraghavan, R. & Ricker, P. M., *MNRAS*, 435:2713–2735, November 2013.
- Vorontsov-Velyaminov, B. A. *Atlas and catalog of interacting galaxies. 1959, Sternberg Institute, Moscow State University*. In *Atlas and catalog of interacting galaxies (1959)*, 1959.
- Vulcani, B., Poggianti, B. M., Aragón-Salamanca, A., Fasano, G., Rudnick, G., Valentini, T., Dressler, A., Bettoni, D., Cava, A., D’Onofrio, M., Fritz, J., Moretti, A., Omizzolo, A., & Varela, J., *MNRAS*, 412:246–268, March 2011.
- Weilbacher, P. M., Duc, P.-A., & Fritze-v. Alvensleben, U., *A&A*, 397:545–555, January 2003.
- Weinmann, S. M., Kauffmann, G., von der Linden, A., & De Lucia, G., *MNRAS*, 406: 2249–2266, August 2010.
- Wen, X.-Q., Wu, H., Zhu, Y.-N., Lam, M. I., Wu, C.-J., Wicker, J., Long, R. J., & Zhao, Y.-H., *MNRAS*, 438:97–115, February 2014.
- Werk, J. K., Putman, M. E., Meurer, G. R., & Santiago-Figueroa, N., *ApJ*, 735:71, July 2011.
- Werner, M. W., Roellig, T. L., Low, F. J., Rieke, G. H., Rieke, M., Hoffmann, W. F., Young, E., Houck, J. R., Brandl, B., Fazio, G. G., Hora, J. L., Gehrz, R. D., Helou, G., Soifer, B. T., Stauffer, J., Keene, J., Eisenhardt, P., Gallagher, D., Gautier, T. N., Irace, W., Lawrence, C. R., Simmons, L., Van Cleve, J. E., Jura, M., Wright, E. L., & Cruikshank, D. P., *ApJS*, 154:1–9, September 2004.
- Wetzel, A. R., Tinker, J. L., Conroy, C., & van den Bosch, F. C., *MNRAS*, 432:336–358, June 2013.
- Whitmore, B. C., Gilmore, D. M., & Jones, C., *ApJ*, 407:489–509, April 1993.
- Williams, R. J., Quadri, R. F., Franx, M., van Dokkum, P., & Labbé, I., *ApJ*, 691:1879–1895, February 2009.
- Wolf, C., Gray, M. E., & Meisenheimer, K., *A&A*, 443:435–449, November 2005.

- Wright, E. L., Eisenhardt, P. R. M., Mainzer, A. K., Ressler, M. E., Cutri, R. M., Jarrett, T., Kirkpatrick, J. D., Padgett, D., McMillan, R. S., Skrutskie, M., & et al., *AJ*, 140:1868, December 2010.
- Wuyts, S., Labbé, I., Franx, M., Rudnick, G., van Dokkum, P. G., Fazio, G. G., Förster Schreiber, N. M., Huang, J., Moorwood, A. F. M., Rix, H.-W., Röttgering, H., & van der Werf, P., *ApJ*, 655:51–65, January 2007.
- Yahil, A. & Vidal, N. V., *ApJ*, 214:347–350, June 1977.
- York, D. G., Adelman, J., Anderson, Jr., J. E., & et al., *AJ*, 120:1579–1587, September 2000.
- Zabludoff, A. I. & Mulchaey, J. S., *ApJ*, 496:39–72, March 1998.
- Zaritsky, D., Kennicutt, Jr., R. C., & Huchra, J. P., *ApJ*, 420:87–109, January 1994.



Appendices



A

Data Tables

The content of this Appendix has been published with Chapter 3 in Monthly Notices of the Royal Astronomical Society (2018, vol. 479, page 2328) as “Galaxy pre-processing in substructures around $z \sim 0.4$ galaxy clusters” by Olave-Rojas D., Cerulo P., Demarco R., Jaffé Y. L., Mercurio A., Rosati P., Balestra I., Nonino M.

Here we present the data used to plot the colour fractions and quenching efficiency in the spectroscopic and spectrophotometric samples of galaxies in clusters and substructures. Tables A.1 – A.6 show the spectroscopic colour fractions as a function of projected distance, magnitude and stellar mass for substructures and clusters. Tables A.7 – A.12 show the background-corrected colour fractions as a function of projected distance, magnitude and stellar mass for the spectrophotometric sample of galaxies in substructures and clusters. Finally, Tables A.13 – A.16 show the mean environmental quenching efficiency as a function of distance for spectroscopic and spectrophotometric samples of galaxies in clusters and substructures.

Table A.1 Spectroscopic colour fraction as a function of distance from the cluster centre.

Cluster	$r_{cl}/r_{200,cl}$			
	0.5	1.5	2.5	3.5
f_b	$0.209^{+0.007}_{-0.007}$	$0.588^{+0.013}_{-0.013}$	$0.706^{+0.024}_{-0.026}$	$0.321^{+0.194}_{-0.092}$
f_g	$0.139^{+0.006}_{-0.006}$	$0.154^{+0.010}_{-0.009}$	$0.158^{+0.022}_{-0.018}$	$0.250^{+0.194}_{-0.092}$
f_r	$0.651^{+0.008}_{-0.009}$	$0.249^{+0.012}_{-0.011}$	$0.131^{+0.022}_{-0.018}$	$0.415^{+0.158}_{-0.158}$
Substructures				
f_b	$0.310^{+0.029}_{-0.024}$	$0.614^{+0.023}_{-0.024}$	$0.905^{+0.033}_{-0.074}$	-
f_g	$0.177^{+0.027}_{-0.021}$	$0.178^{+0.020}_{-0.017}$	$0.033^{+0.014}_{-0.019}$	-
f_r	$0.495^{+0.030}_{-0.032}$	$0.202^{+0.022}_{-0.020}$	$0.092^{+0.074}_{-0.033}$	-



Table A.2 Spectroscopic colour fraction as a function of distance from the overdensity centre

Cluster	r/r_{200}				
	0.1	0.3	0.5	0.7	0.9
f_b	$0.104^{+0.011}_{-0.008}$	$0.153^{+0.014}_{-0.011}$	$0.197^{+0.023}_{-0.019}$	$0.237^{+0.027}_{-0.022}$	$0.380^{+0.029}_{-0.027}$
f_g	$0.124^{+0.014}_{-0.012}$	$0.110^{+0.013}_{-0.011}$	$0.137^{+0.022}_{-0.017}$	$0.194^{+0.026}_{-0.022}$	$0.137^{+0.023}_{-0.018}$
f_r	$0.770^{+0.014}_{-0.016}$	$0.734^{+0.016}_{-0.017}$	$0.664^{+0.025}_{-0.028}$	$0.567^{+0.029}_{-0.031}$	$0.482^{+0.029}_{-0.029}$
Substructures					
f_b	$0.375^{+0.051}_{-0.024}$	$0.423^{+0.111}_{-0.055}$	$0.410^{+0.183}_{-0.039}$	$0.462^{+0.159}_{-0.031}$	$0.734^{+0.274}_{-0.103}$
f_g	$0.200^{+0.116}_{-0.061}$	$0.074^{+0.111}_{-0.055}$	$0.067^{+0.101}_{-0.050}$	$0.056^{+0.086}_{-0.042}$	$0.129^{+0.179}_{-0.096}$
f_r	$0.349^{+0.061}_{-0.116}$	$0.385^{+0.055}_{-0.111}$	$0.450^{+0.039}_{-0.183}$	$0.402^{+0.031}_{-0.159}$	$0.119^{+0.103}_{-0.274}$

Table A.3 Spectroscopic colour fraction as a function of distance from the cluster centre for massive and less massive galaxies

	$r_{cl}/r_{200_{cl}}$			
	0.5	1.5	2.5	3.5
Cluster				
	$M_{\star} \geq 10^{10.5} M_{\odot}$			
f_b	$0.071^{+0.007}_{-0.006}$	$0.239^{+0.032}_{-0.023}$	$0.243^{+0.037}_{-0.028}$	$0.252^{+0.179}_{-0.096}$
f_g	$0.050^{+0.009}_{-0.008}$	$0.105^{+0.030}_{-0.020}$	$0.353^{+0.043}_{-0.039}$	$0.129^{+0.179}_{-0.100}$
f_r	$0.878^{+0.009}_{-0.012}$	$0.633^{+0.031}_{-0.038}$	$0.391^{+0.043}_{-0.042}$	$0.723^{+0.096}_{-0.179}$
	$M_{\star} < 10^{10.5} M_{\odot}$			
f_b	$0.301^{+0.011}_{-0.010}$	$0.678^{+0.014}_{-0.014}$	$0.822^{+0.021}_{-0.026}$	$0.518^{+0.203}_{-0.203}$
f_g	$0.197^{+0.100}_{-0.009}$	$0.167^{+0.011}_{-0.010}$	$0.109^{+0.022}_{-0.016}$	$0.500^{+0.129}_{-0.203}$
f_r	$0.501^{+0.012}_{-0.012}$	$0.150^{+0.012}_{-0.011}$	$0.067^{+0.020}_{-0.014}$	$0.107^{+0.179}_{-0.096}$
Substructures				
	$M_{\star} \geq 10^{10.5} M_{\odot}$			
f_b	$0.130^{+0.012}_{-0.006}$	$0.256^{+0.113}_{-0.048}$	$0.393^{+0.024}_{-0.210}$	-
f_g	$0.130^{+0.043}_{-0.027}$	$0.100^{+0.107}_{-0.034}$	$0.293^{+0.309}_{-0.210}$	-
f_r	$0.722^{+0.027}_{-0.043}$	$0.623^{+0.071}_{-0.117}$	$0.587^{+0.210}_{-0.309}$	-
	$M_{\star} < 10^{10.5} M_{\odot}$			
f_b	$0.420^{+0.040}_{-0.036}$	$0.696^{+0.240}_{-0.026}$	$0.982^{+0.016}_{-0.034}$	-
f_g	$0.205^{+0.036}_{-0.029}$	$0.195^{+0.023}_{-0.020}$	$0.021^{+0.034}_{-0.016}$	-
f_r	$0.362^{+0.040}_{-0.039}$	$0.105^{+0.020}_{-0.016}$	$0.017^{+0.034}_{-0.016}$	-

Table A.4 Spectroscopic colour fraction as a function of distance from the overdensity centre for massive and less massive galaxies

Cluster	r/r_{200}				
	0.1	0.3	0.5	0.7	0.9
$M_{\star} \geq 10^{10.5} M_{\odot}$					
f_b	$0.051^{+0.008}_{-0.004}$	$0.062^{+0.012}_{-0.008}$	$0.089^{+0.014}_{-0.012}$	$0.052^{+0.012}_{-0.006}$	$0.147^{+0.047}_{-0.026}$
f_g	$0.032^{+0.017}_{-0.012}$	$0.041^{+0.018}_{-0.014}$	$0.059^{+0.018}_{-0.011}$	$0.065^{+0.036}_{-0.017}$	$0.081^{+0.044}_{-0.022}$
f_r	$0.920^{+0.012}_{-0.017}$	$0.899^{+0.016}_{-0.020}$	$0.852^{+0.016}_{-0.021}$	$0.888^{+0.017}_{-0.036}$	$0.770^{+0.037}_{-0.054}$
$M_{\star} < 10^{10.5} M_{\odot}$					
f_b	$0.147^{+0.018}_{-0.014}$	$0.245^{+0.024}_{-0.021}$	$0.285^{+0.024}_{-0.021}$	$0.338^{+0.036}_{-0.031}$	$0.460^{+0.037}_{-0.033}$
f_g	$0.198^{+0.022}_{-0.019}$	$0.181^{+0.023}_{-0.019}$	$0.200^{+0.034}_{-0.027}$	$0.261^{+0.036}_{-0.030}$	$0.156^{+0.019}_{-0.016}$
f_r	$0.653^{+0.026}_{-0.025}$	$0.572^{+0.026}_{-0.027}$	$0.514^{+0.038}_{-0.039}$	$0.399^{+0.038}_{-0.036}$	$0.383^{+0.024}_{-0.023}$
Substructures					
$M_{\star} \geq 10^{10.5} M_{\odot}$					
f_b	$0.145^{+0.052}_{-0.024}$	$0.205^{+0.111}_{-0.056}$	$0.237^{+0.183}_{-0.039}$	$0.219^{+0.159}_{-0.031}$	$0.356^{+0.274}_{-0.103}$
f_g	$0.200^{+0.116}_{-0.061}$	$0.074^{+0.111}_{-0.055}$	$0.067^{+0.101}_{-0.050}$	$0.056^{+0.086}_{-0.042}$	$0.129^{+0.179}_{-0.096}$
f_r	$0.664^{+0.061}_{-0.116}$	$0.768^{+0.055}_{-0.111}$	$0.738^{+0.039}_{-0.183}$	$0.755^{+0.031}_{-0.159}$	$0.623^{+0.103}_{-0.274}$
$M_{\star} < 10^{10.5} M_{\odot}$					
f_b	$0.469^{+0.068}_{-0.063}$	$0.535^{+0.055}_{-0.056}$	$0.514^{+0.064}_{-0.062}$	$0.584^{+0.052}_{-0.054}$	$0.825^{+0.037}_{-0.055}$
f_g	$0.286^{+0.067}_{-0.052}$	$0.250^{+0.054}_{-0.042}$	$0.200^{+0.061}_{-0.042}$	$0.182^{+0.048}_{-0.034}$	$0.176^{+0.055}_{-0.037}$
f_r	$0.237^{+0.067}_{-0.052}$	$0.208^{+0.054}_{-0.042}$	$0.277^{+0.065}_{-0.055}$	$0.226^{+0.052}_{-0.042}$	$0.008^{+0.016}_{-0.007}$

Table A.5 Spectroscopic colour fraction as a function of R_c

Cluster	R_c				
	19.5	20.5	21.5	22.5	23.5
f_b	$0.189^{+0.034}_{-0.017}$	$0.240^{+0.018}_{-0.015}$	$0.382^{+0.017}_{-0.016}$	$0.454^{+0.018}_{-0.017}$	$0.578^{+0.023}_{-0.023}$
f_g	$0.048^{+0.025}_{-0.019}$	$0.121^{+0.018}_{-0.014}$	$0.121^{+0.013}_{-0.011}$	$0.171^{+0.014}_{-0.013}$	$0.192^{+0.019}_{-0.017}$
f_r	$0.744^{+0.023}_{-0.040}$	$0.617^{+0.020}_{-0.022}$	$0.481^{+0.017}_{-0.018}$	$0.362^{+0.018}_{-0.018}$	$0.222^{+0.021}_{-0.019}$
Substructures					
f_b	$0.1805^{+0.070}_{-0.034}$	$0.210^{+0.045}_{-0.026}$	$0.422^{+0.051}_{-0.045}$	$0.553^{+0.046}_{-0.046}$	$0.770^{+0.036}_{-0.046}$
f_g	$0.045^{+0.051}_{-0.036}$	$0.185^{+0.051}_{-0.036}$	$0.167^{+0.045}_{-0.031}$	$0.205^{+0.042}_{-0.032}$	$0.167^{+0.042}_{-0.030}$
f_r	$0.955^{+0.034}_{-0.070}$	$0.704^{+0.045}_{-0.056}$	$0.479^{+0.051}_{-0.050}$	$0.234^{+0.045}_{-0.038}$	$0.061^{+0.034}_{-0.018}$

Table A.6 Spectroscopic colour fraction as a function of $\log(M_\star/M_\odot)$

Cluster	$\log(M_\star/M_\odot)$			
	8.5	9.5	10.5	11.5
f_b	$0.978^{+0.019}_{-0.041}$	$0.636^{+0.015}_{-0.016}$	$0.296^{+0.011}_{-0.010}$	$0.141^{+0.006}_{-0.003}$
f_g	$0.025^{+0.041}_{-0.019}$	$0.182^{+0.013}_{-0.117}$	$0.139^{+0.010}_{-0.009}$	$0.026^{+0.014}_{-0.010}$
f_r	$0.021^{+0.041}_{-0.019}$	$0.175^{+0.014}_{-0.012}$	$0.546^{+0.012}_{-0.013}$	$0.808^{+0.010}_{-0.014}$
Substructures				
f_b	-	$0.764^{+0.025}_{-0.029}$	$0.323^{+0.027}_{-0.022}$	$0.156^{+0.018}_{-0.011}$
f_g	-	$0.241^{+0.037}_{-0.031}$	$0.177^{+0.034}_{-0.026}$	$0.582^{+0.038}_{-0.040}$
f_r	-	$0.048^{+0.028}_{-0.013}$	$0.483^{+0.028}_{-0.013}$	$0.816^{+0.013}_{-0.028}$

Table A.7 Spectrophotometric colour fraction as a function of distance from the cluster centre.

Cluster	$r_{cl}/r_{200_{cl}}$			
	0.5	1.5	2.5	3.5
f_b	$0.290^{+0.013}_{-0.013}$	$0.640^{+0.013}_{-0.013}$	$0.674^{+0.012}_{-0.012}$	$0.664^{+0.020}_{-0.020}$
f_g	$0.089^{+0.008}_{-0.008}$	$0.121^{+0.009}_{-0.008}$	$0.121^{+0.008}_{-0.008}$	$0.093^{+0.013}_{-0.011}$
f_r	$0.627^{+0.014}_{-0.014}$	$0.238^{+0.012}_{-0.012}$	$0.206^{+0.011}_{-0.010}$	$0.246^{+0.019}_{-0.018}$
Substructures				
f_b	$0.416^{+0.031}_{-0.030}$	$0.650^{+0.025}_{-0.026}$	$0.853^{+0.114}_{-0.179}$	-
f_g	$0.099^{+0.020}_{-0.018}$	$0.077^{+0.014}_{-0.013}$	$0.248^{+0.129}_{-0.104}$	-
f_r	$0.481^{+0.031}_{-0.032}$	$0.276^{+0.024}_{-0.024}$	$0.089^{+0.154}_{-0.078}$	-

Table A.8 Spectrophotometric colour fraction as a function of distance from the overdensity centre

Cluster	r/r_{200}				
	0.1	0.3	0.5	0.7	0.9
f_b	$0.067^{+0.022}_{-0.015}$	$0.212^{+0.029}_{-0.026}$	$0.282^{+0.032}_{-0.030}$	$0.342^{+0.034}_{-0.033}$	$0.463^{+0.032}_{-0.032}$
f_g	$0.042^{+0.017}_{-0.013}$	$0.074^{+0.019}_{-0.016}$	$0.108^{+0.023}_{-0.020}$	$0.097^{+0.020}_{-0.018}$	$0.115^{+0.020}_{-0.019}$
f_r	$0.892^{+0.023}_{-0.027}$	$0.751^{+0.030}_{-0.032}$	$0.642^{+0.034}_{-0.035}$	$0.592^{+0.032}_{-0.034}$	$0.454^{+0.031}_{-0.031}$
Substructures					
f_b	$0.548^{+0.134}_{-0.128}$	$0.571^{+0.060}_{-0.060}$	$0.574^{+0.045}_{-0.044}$	$0.584^{+0.039}_{-0.040}$	$0.586^{+0.038}_{-0.038}$
f_g	$0.045^{+0.051}_{-0.030}$	$0.106^{+0.037}_{-0.030}$	$0.086^{+0.026}_{-0.022}$	$0.093^{+0.024}_{-0.020}$	$0.064^{+0.020}_{-0.016}$
f_r	$0.460^{+0.097}_{-0.098}$	$0.349^{+0.056}_{-0.055}$	$0.354^{+0.043}_{-0.043}$	$0.334^{+0.038}_{-0.038}$	$0.359^{+0.037}_{-0.037}$

Table A.9 Spectrophotometric colour fraction as a function of distance from the cluster centre for massive and less massive galaxies

Cluster	$r_{cl}/r_{200_{cl}}$			
	0.5	1.5	2.5	3.5
$M_{\star} \geq 10^{10.5} M_{\odot}$				
f_b	$0.083^{+0.010}_{-0.009}$	$0.301^{+0.029}_{-0.028}$	$0.272^{+0.028}_{-0.026}$	$0.193^{+0.055}_{-0.035}$
f_g	$0.041^{+0.011}_{-0.010}$	$0.105^{+0.023}_{-0.020}$	$0.157^{+0.028}_{-0.025}$	$0.060^{+0.034}_{-0.033}$
f_r	$0.902^{+0.013}_{-0.015}$	$0.608^{+0.034}_{-0.035}$	$0.584^{+0.036}_{-0.037}$	$0.779^{+0.046}_{-0.097}$
$M_{\star} < 10^{10.5} M_{\odot}$				
f_b	$0.393^{+0.017}_{-0.018}$	$0.697^{+0.014}_{-0.013}$	$0.724^{+0.011}_{-0.012}$	$0.691^{+0.021}_{-0.020}$
f_g	$0.112^{+0.012}_{-0.011}$	$0.125^{+0.009}_{-0.010}$	$0.117^{+0.008}_{-0.008}$	$0.095^{+0.013}_{-0.011}$
f_r	$0.506^{+0.018}_{-0.018}$	$0.183^{+0.012}_{-0.012}$	$0.164^{+0.011}_{-0.009}$	$0.224^{+0.019}_{-0.018}$
Substructures				
$M_{\star} \geq 10^{10.5} M_{\odot}$				
f_b	$0.162^{+0.036}_{-0.017}$	$0.307^{+0.076}_{-0.063}$	$0.368^{+0.307}_{-0.210}$	-
f_g	$0.024^{+0.036}_{-0.017}$	$0.047^{+0.056}_{-0.032}$	$0.294^{+0.307}_{-0.210}$	-
f_r	$0.811^{+0.018}_{-0.038}$	$0.697^{+0.082}_{-0.096}$	$0.432^{+0.330}_{-0.348}$	-
$M_{\star} < 10^{10.5} M_{\odot}$				
f_b	$0.453^{+0.034}_{-0.033}$	$0.680^{+0.022}_{-0.020}$	$0.879^{+0.034}_{-0.034}$	-
f_g	$0.638^{+0.026}_{-0.025}$	$0.080^{+0.015}_{-0.013}$	$0.295^{+0.024}_{-0.024}$	-
f_r	$0.434^{+0.099}_{-0.166}$	$0.245^{+0.138}_{-0.111}$	$0.095^{+0.181}_{-0.084}$	-

Table A.10 Spectrophotometric colour fraction as a function of distance from the overdensity centre for massive and less massive galaxies

Cluster	r/r_{200}				
	0.1	0.3	0.5	0.7	0.9
$M_{\star} \geq 10^{10.5} M_{\odot}$					
f_b	$0.056^{+0.014}_{-0.006}$	$0.067^{+0.017}_{-0.011}$	$0.096^{+0.029}_{-0.021}$	$0.074^{+0.024}_{-0.015}$	$0.184^{+0.047}_{-0.039}$
f_g	$0.021^{+0.019}_{-0.011}$	$0.040^{+0.025}_{-0.017}$	$0.077^{+0.035}_{-0.027}$	$0.042^{+0.029}_{-0.020}$	$0.060^{+0.034}_{-0.025}$
f_r	$0.941^{+0.007}_{-0.016}$	$0.939^{+0.010}_{-0.021}$	$0.921^{+0.023}_{-0.040}$	$0.935^{+0.013}_{-0.025}$	$0.884^{+0.047}_{-0.066}$
$M_{\star} < 10^{10.5} M_{\odot}$					
f_b	$0.089^{+0.046}_{-0.030}$	$0.336^{+0.046}_{-0.044}$	$0.393^{+0.045}_{-0.042}$	$0.460^{+0.044}_{-0.042}$	$0.553^{+0.038}_{-0.038}$
f_g	$0.065^{+0.029}_{-0.024}$	$0.102^{+0.029}_{-0.025}$	$0.128^{+0.030}_{-0.028}$	$0.120^{+0.026}_{-0.023}$	$0.133^{+0.024}_{-0.022}$
f_r	$0.882^{+0.040}_{-0.047}$	$0.647^{+0.051}_{-0.052}$	$0.534^{+0.046}_{-0.047}$	$0.473^{+0.041}_{-0.040}$	$0.363^{+0.035}_{-0.034}$
Substructures					
$M_{\star} \geq 10^{10.5} M_{\odot}$					
f_b	$0.204^{+0.136}_{-0.069}$	$0.197^{+0.100}_{-0.050}$	$0.434^{+0.133}_{-0.114}$	$0.181^{+0.079}_{-0.039}$	$0.266^{+0.153}_{-0.095}$
f_g	$0.095^{+0.136}_{-0.069}$	$0.068^{+0.100}_{-0.050}$	$0.046^{+0.070}_{-0.033}$	$0.134^{+0.155}_{-0.092}$	$0.057^{+0.086}_{-0.042}$
f_r	$0.640^{+0.171}_{-0.346}$	$0.759^{+0.064}_{-0.131}$	$0.647^{+0.139}_{-0.179}$	$0.754^{+0.068}_{-0.129}$	$0.732^{+0.088}_{-0.182}$
$M_{\star} < 10^{10.5} M_{\odot}$					
f_b	$0.712^{+0.165}_{-0.164}$	$0.632^{+0.064}_{-0.065}$	$0.598^{+0.048}_{-0.048}$	$0.620^{+0.040}_{-0.042}$	$0.611^{+0.040}_{-0.039}$
f_g	$0.056^{+0.063}_{-0.038}$	$0.119^{+0.041}_{-0.034}$	$0.096^{+0.028}_{-0.024}$	$0.094^{+0.025}_{-0.021}$	$0.068^{+0.021}_{-0.017}$
f_r	$0.389^{+0.108}_{-0.103}$	$0.294^{+0.058}_{-0.054}$	$0.326^{+0.045}_{-0.044}$	$0.301^{+0.039}_{-0.038}$	$0.333^{+0.038}_{-0.037}$

Table A.11 Spectrophotometric colour fraction as a function of R_c

Cluster	R_c				
	19.5	20.5	21.5	22.5	23.5
f_b	$0.298^{+0.087}_{-0.081}$	$0.255^{+0.021}_{-0.019}$	$0.370^{+0.016}_{-0.016}$	$0.468^{+0.017}_{-0.017}$	$0.656^{+0.017}_{-0.017}$
f_g	$0.118^{+0.044}_{-0.037}$	$0.084^{+0.015}_{-0.013}$	$0.119^{+0.012}_{-0.011}$	$0.139^{+0.012}_{-0.012}$	$0.127^{+0.011}_{-0.010}$
f_r	$0.605^{+0.069}_{-0.071}$	$0.625^{+0.021}_{-0.023}$	$0.497^{+0.018}_{-0.019}$	$0.386^{+0.017}_{-0.018}$	$0.206^{+0.014}_{-0.014}$
Substructures					
f_b	$0.205^{+0.122}_{-0.061}$	$0.212^{+0.064}_{-0.044}$	$0.353^{+0.056}_{-0.052}$	$0.289^{+0.058}_{-0.055}$	$0.394^{+0.055}_{-0.055}$
f_g	$0.084^{+0.122}_{-0.061}$	$0.025^{+0.038}_{-0.018}$	$0.085^{+0.035}_{-0.028}$	$0.147^{+0.037}_{-0.033}$	$0.144^{+0.034}_{-0.030}$
f_r	$0.714^{+0.105}_{-0.224}$	$0.792^{+0.034}_{-0.065}$	$0.561^{+0.057}_{-0.059}$	$0.480^{+0.049}_{-0.051}$	$0.371^{+0.045}_{-0.045}$

Table A.12 Spectrophotometric colour fraction as a function of $\log(M_*/M_\odot)$

	$\log(M_*/M_\odot)$			
	8.5	9.5	10.5	11.5
Cluster				
f_b	$0.860^{+0.010}_{-0.011}$	$0.626^{+0.011}_{-0.012}$	$0.301^{+0.010}_{-0.011}$	$0.127^{+0.020}_{-0.011}$
f_g	$0.069^{+0.007}_{-0.007}$	$0.137^{+0.008}_{-0.008}$	$0.112^{+0.009}_{-0.008}$	$0.100^{+0.025}_{-0.022}$
f_r	$0.071^{+0.008}_{-0.007}$	$0.227^{+0.010}_{-0.010}$	$0.565^{+0.013}_{-0.013}$	$0.652^{+0.031}_{-0.034}$
Substructures				
f_b	$0.844^{+0.027}_{-0.029}$	$0.440^{+0.034}_{-0.032}$	$0.277^{+0.033}_{-0.030}$	$0.305^{+0.102}_{-0.081}$
f_g	$0.051^{+0.016}_{-0.013}$	$0.132^{+0.022}_{-0.020}$	$0.072^{+0.025}_{-0.021}$	$0.039^{+0.059}_{-0.028}$
f_r	$0.104^{+0.023}_{-0.020}$	$0.394^{+0.031}_{-0.031}$	$0.636^{+0.040}_{-0.042}$	$0.613^{+0.107}_{-0.138}$

Table A.13 Mean environmental quenching efficiency as a function of distance from the cluster centre for the spectroscopic sample.

$r_{cl}/r_{200_{cl}}$	0.5	1.5	2.5	3.5
	ϵ_q			
Cluster Galaxies	$0.709^{+0.008}_{-0.008}$	$0.151^{+0.011}_{-0.011}$	$0.012^{+0.019}_{-0.018}$	$0.382^{+0.150}_{-0.148}$
Massive Cluster Galaxies	$0.768^{+0.024}_{-0.024}$	$0.021^{+0.075}_{-0.076}$	$0.805^{+0.094}_{-0.093}$	$0.266^{+0.300}_{-0.194}$
Less Massive Cluster Galaxies	$0.540^{+0.010}_{-0.010}$	$0.078^{+0.010}_{-0.010}$	$0.031^{+0.015}_{-0.015}$	$0.023^{+0.086}_{-0.061}$
Substructure Galaxies	$0.593^{+0.029}_{-0.029}$	$0.086^{+0.019}_{-0.020}$	$0.066^{+0.051}_{-0.048}$	-
Massive Substructure Galaxies	$0.600^{+0.078}_{-0.078}$	$0.056^{+0.206}_{-0.207}$	$0.171^{+0.572}_{-0.514}$	-
Less Massive Substructure Galaxies	$0.426^{+0.035}_{-0.035}$	$0.020^{+0.008}_{-0.008}$	$0.096^{+0.022}_{-0.021}$	-

Table A.14 Mean environmental quenching efficiency as a function of distance from the overdensity centre for the spectroscopic sample.

r/r_{200}	0.1	0.3	0.5	0.7	0.9
	ϵ_q				
Cluster Galaxies	$0.875^{+0.014}_{-0.014}$	$0.825^{+0.015}_{-0.015}$	$0.728^{+0.025}_{-0.025}$	$0.593^{+0.028}_{-0.028}$	$0.474^{+0.028}_{-0.028}$
Massive Cluster Galaxies	$0.903^{+0.032}_{-0.032}$	$0.836^{+0.039}_{-0.039}$	$0.685^{+0.040}_{-0.041}$	$0.800^{+0.058}_{-0.058}$	$0.420^{+0.100}_{-0.100}$
Less Massive Cluster Galaxies	$0.741^{+0.021}_{-0.021}$	$0.635^{+0.024}_{-0.024}$	$0.558^{+0.034}_{-0.034}$	$0.407^{+0.033}_{-0.033}$	$0.386^{+0.021}_{-0.021}$
Substructure Galaxies	$0.361^{+0.053}_{-0.053}$	$0.418^{+0.044}_{-0.044}$	$0.520^{+0.048}_{-0.048}$	$0.445^{+0.041}_{-0.041}$	$0.006^{+0.018}_{-0.018}$
Massive Substructure Galaxies	$0.387^{+0.194}_{-0.131}$	$0.772^{+0.181}_{-0.183}$	$0.659^{+0.241}_{-0.236}$	$0.721^{+0.206}_{-0.210}$	$0.234^{+0.267}_{-0.207}$
Less Massive Substructure Galaxies	$0.239^{+0.054}_{-0.053}$	$0.194^{+0.043}_{-0.043}$	$0.298^{+0.054}_{-0.054}$	$0.222^{+0.042}_{-0.042}$	$0.106^{+0.011}_{-0.011}$

Table A.15 Mean environmental quenching efficiency as a function of distance from the cluster centre for the spectrophotometric sample.

$r_{cl}/r_{200,cl}$	0.5	1.5	2.5	3.5
	ϵ_q			
Cluster Galaxies	$0.676^{+0.013}_{-0.013}$	$0.136^{+0.011}_{-0.011}$	$0.091^{+0.010}_{-0.010}$	$0.147^{+0.017}_{-0.017}$
Massive Cluster Galaxies	$0.844^{+0.031}_{-0.031}$	$0.102^{+0.075}_{-0.076}$	$0.180^{+0.080}_{-0.080}$	$0.450^{+0.101}_{-0.079}$
Less Massive Cluster Galaxies	$0.548^{+0.016}_{-0.016}$	$0.122^{+0.011}_{-0.011}$	$0.097^{+0.009}_{-0.009}$	$0.176^{+0.017}_{-0.017}$
Substructure Galaxies	$0.570^{+0.030}_{-0.030}$	$0.188^{+0.023}_{-0.023}$	$0.071^{+0.069}_{-0.054}$	-
Massive Substructure Galaxies	$0.930^{+0.061}_{-0.062}$	$0.185^{+0.194}_{-0.175}$	$0.670^{+0.745}_{-0.742}$	-
Less Massive Substructure Galaxies	$0.535^{+0.030}_{-0.030}$	$0.204^{+0.022}_{-0.021}$	$0.006^{+0.081}_{-0.059}$	-



Table A.16 Mean environmental quenching efficiency as a function of distance from the overdensity centre for the spectrophotometric sample.

r/r_{200}	0.1	0.3	0.5	0.7	0.9
	ϵ_q				
Cluster Galaxies	$0.999^{+0.023}_{-0.024}$	$0.849^{+0.029}_{-0.029}$	$0.698^{+0.032}_{-0.033}$	$0.628^{+0.031}_{-0.031}$	$0.044^{+0.029}_{-0.029}$
Massive Cluster Galaxies	$0.972^{+0.025}_{-0.025}$	$0.963^{+0.034}_{-0.034}$	$0.905^{+0.069}_{-0.069}$	$0.951^{+0.042}_{-0.042}$	$0.789^{+0.124}_{-0.123}$
Less Massive Cluster Galaxies	$0.999^{+0.039}_{-0.039}$	$0.733^{+0.046}_{-0.046}$	$0.584^{+0.042}_{-0.042}$	$0.504^{+0.037}_{-0.036}$	$0.359^{+0.031}_{-0.031}$
Substructure Galaxies	$0.537^{+0.091}_{-0.093}$	$0.361^{+0.052}_{-0.053}$	$0.368^{+0.040}_{-0.041}$	$0.336^{+0.036}_{-0.036}$	$0.377^{+0.035}_{-0.035}$
Massive Substructure Galaxies	$0.298^{+0.282}_{-0.284}$	$0.740^{+0.214}_{-0.214}$	$0.323^{+0.231}_{-0.176}$	$0.718^{+0.216}_{-0.216}$	$0.638^{+0.300}_{-0.281}$
Less Massive Substructure Galaxies	$0.468^{+0.094}_{-0.094}$	$0.324^{+0.050}_{-0.050}$	$0.373^{+0.040}_{-0.040}$	$0.335^{+0.034}_{-0.035}$	$0.383^{+0.034}_{-0.033}$